UNIVERSITÁ DEGLI STUDI DI PADOVA

Dipartimento di Ingegneria Industriale
Corso di Laurea Magistrale in Ingegneria dell'Energia Elettrica

MCCXXII

Electric vehicle synchronous motors comparison and design

Relatore: Chiar.mo Prof. **Bianchi Nicola**

Laureando: **Bonfante Michele** - 1132611

Anno Accademico 2017-2018

Contents

Abstract

This thesis has been accomplished in EDLAB, University of Padua. It focuses on automotive synchronous motors, in particular IPM currently adopted in electric vehicles and PM assisted REL developed on the following specifications that have been initially given:

- $\hat{V}_{phase-phase} = 345$ [V]
- $\hat{I}_{conductor,max} = 550$ [A]
- $L_{stack,max} = 180$ [mm]
- $D_{ext} = 256$ [mm]

These specifications have been imposed by Jaguar and have been taken as reference for the REL and PMREL design.
The reason behind PMREL's choice is the good performance developed by this type of motor together with the lower motor price due to the less expensive Ferrite PM. The motors have been designed by means of electromagnetic simulations in FEMM 4.2 coupled with data analysis in Matlab and Simulink.
The first chapter briefly introduces synchronous motors and it is therefore necessary to explain different performance behaviours between IPM, PMREL and REL. The second one presents the current automotive IPM and particular focus is placed on their maximum performances. Chapter three deals with three IPM motors whose geometries have been changed first into pure reluctance and later in PM assisted REL to study the performance gap between these motors in a better way. Eventually, chapters four and five offer an in-depth analysis of PMREL and REL designed motors with suitable characteristics for an automotive application.

Sommario

Questo lavoro di tesi é stato svolto per portare a termine un'analisi comparativa di motori sincroni IPM (Interior Permanent Magnet) usati attualmente in ambito automotive con motori REL e PMAREL (Riluttanza e Riluttanza assistiti) progettati secondo le specifiche date inizialmente.
Il capitolo 1 rappresenta una introduzione teorica ai concetti di macchine a magneti permanenti con le definizioni dei luoghi di funzionamento quali MTPA punto base, flux weakening e MTPV. Questo capitolo é necessario in quanto nei successivi capitoli i motori presentati sono studiati seguendo queste particolari traiettorie nel piano dq e sono confrontati secondo tali prestazioni.
Il capitolo 2 rappresenta un'analisi approfondita delle prestazioni che gli attuali IPM possono erogare, con tutte le considerazioni del caso sui vari carichi elettrici applicati, sui volumi e poi piú in particolare sulla densitá di potenza di queste macchine.
Il capitolo 3 prevede di analizzare tre dei motori introdotti nel secondo capitolo previa sostituzione del rotore con delle versioni PMREL e riluttanza. In questo modo si vogliono mettere a confronto le massime prestazioni di tali differenti modelli in modo da capire se una possibile versione PMREL di tali motori possa essere adatta all'uso automobilistico.
Nel capitolo 4 sono presentati passaggi che portano alla selezione di un motore PMREL con caratteristiche adatte all'ambito automotive. Per giungere a tali conclusioni sono presi in considerazione diversi fattori quali le dimensioni e le densitá di potenza e coppia. Infine si deve tener conto del particolare avvolgimento da inserire i questo motore. Tale avvolgimento é del tipo hairpin, ovvero una sorta di piattina che va ad incrementare il K_{fill} nella cava. Per tale motivi sono scelte le geometrie con cave di larghezza minore in modo da avere avvolgimenti piú stretti e dunque piú facilmente piegabili nella parte delle testate. Infine le prestazioni delle macchine PMREL con maggior numero di cave sono confrontate con modelli quali Prius, Leaf e BMW i3.
Nel capitolo 5 sono descritti i passaggi che portano al confronto di motori a riluttanza con IPM attualmente in uso. Per tali motori si é scelto un minor numero di poli in modo da avere un adeguato *saliency ratio*. A causa dell'assenza di magneti nel rotore, questi motori presentano prestazioni minori dei corrispettivi IPM e PMREL, dunque il confronto deve esser portato al livello economico per poter giustificarne l'eventuale considerazione allo scopo.
L'obiettivo finale di questa tesi é dunque arrivare ad un motore con prestazioni adatte all'ambito automotive e che porti vantaggi rispetto i motori IPM attualmente impiegati.

Introduction

Hybrid and electric vehicles (EVs), ranging from micro-hybrid to full electric vehicles, are emerging as the most efficient and environmentally friendly products in the automotive industry. They aim at reducing the fossil fuels consumption, decreasing the overall emissions and improving the vehicle efficiency and performance. These are the reasons why the conventional internal combustion engine (ICE) power trains are upgraded and coupled with electrified powertrains.

Electric traction motors are one of the key technologies which play a major role in the "electric" transition due to their high power density, wide speed range and high efficiency. Nowadays' electric vehicles have been equipped with both the asynchronous and synchronous machines and have therefore their pros and cons.

Induction machines (IM) are the result of a well-known technology, for they are relatively low cost and a reliable solution. Due to the rotor cage or winding, they suffer from Joule Losses in the rotor too. This leads to a "stronger" cooling system and to an overall lower operating efficiency.

The other machine is the Permanent Magnet Synchronous Motor (PMSM) which uses rare-earth magnets to increase the flux density at the air gap. This type of machine can be classified on the basis of the Permanent Magnet's disposition inside the rotor. For example, there is the Surface mounted PM (SPM) in which the magnet is glued on the rotor surface. This solution is characterised by a relatively easy manufacturing of the rotor although the permanent magnet can be subjected to the separation from the rotor at high speeds. In order to avoid this, the rotor needs to be covered with a protective shell that increases the mechanical stability. Another solution is that of maintaining the motor maximum speed below a safety one.

Another type of PM motor is the Interior Permanent Magnet (IPM) in which the magnets are embedded in specific rectangular-shaped holes inside the rotor. The IPM can be further classified in V-shaped IPM, where the magnets are more than one per pole and they are disposed in such a way to form a V-shape. Another type of machine is the spoke or I-shaped IPM, in which the magnets are placed with their longer side radially. All these IPM are not vulnerable to the detachment of the magnets but they require a better rotor manufacturing, in particular for the mechanical strength and the PM flux losses due to the iron link and ribs.

The major benefit of the PM in the rotor is the absence of Joule Losses, which leads to an overall improvement on the efficiency with respect to the Induction Motor. However, the magnet is a delicate and precious material and therefore has to be protected from demagnetization. Moreover, the magnet is a very expensive part of the machine. On this last point, another type of IPM that uses a magnetic material made of Ceramic-Ferrite

composite is introduced. It is less expensive but at the same time produces a lower magnetic flux density at the air-gap. This kind of magnet can be inserted in the Synchronous Reluctance Machines (Sync-REL or REL) to increase their performance especially in the Flux Weakening region.
The previously mentioned IPM motors are characterized by the highest torque density between the Synchronous motor typologies although they suffer from the rare earth magnets price variability, as it can be seen in figure 1.

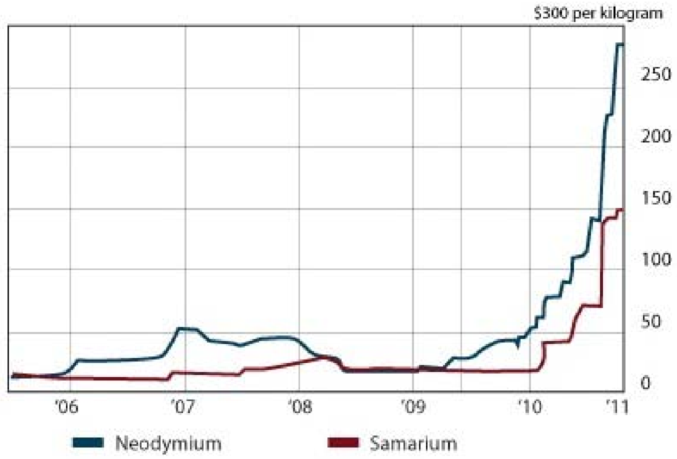

Figure 1: Rare-earth prices over the period of time between 2005-2011. It shows that in a very short period of time rare earth magnets increased their price from 50 to 280 Euro per kilogram.

Thus, in order to avoid these sudden price variations, the synchronous motors can be designed as a Ferrite PM assisted REL, in which the magnets have lower performances but present at the same time a much lower price. This implies that the PMREL motor developed to replace a similar performance IPM, will present: higher volume for compensating the torque loss and a lower price due to cheaper magnets.

Chapter 1

Synchronous Reluctance and Permanent Magnet Motors

This chapter offers an overview on the Permanent Magnet and Reluctance machines which are the subject of this thesis. The basic principles and models of these electric machines are here explained and compared. The different motors presented below are the Surface PM motor (SPM), the Reluctance motor (REL), the PM Assisted Reluctance motor (PMAREL), the Interior PM motor (IPM) with different PM's disposition.

1.1 Preliminary Information

In this section general information on the electrical machines is provided. First of all in this thesis we refer to a motor supplied by a three phase power source. In this system there are three alternating currents (i_a, i_b, i_c) and voltages (u_a, u_b, u_c) of the same frequency but phase shifted of one third of a period. We assume the voltages with respect to neutral terminal, and the currents are phase ones like in figure 1.1.
If we sum the phase-to-neutral voltages one another we obtain the line-to-line voltages (u_{ab}, u_{bc}, u_{ca}).

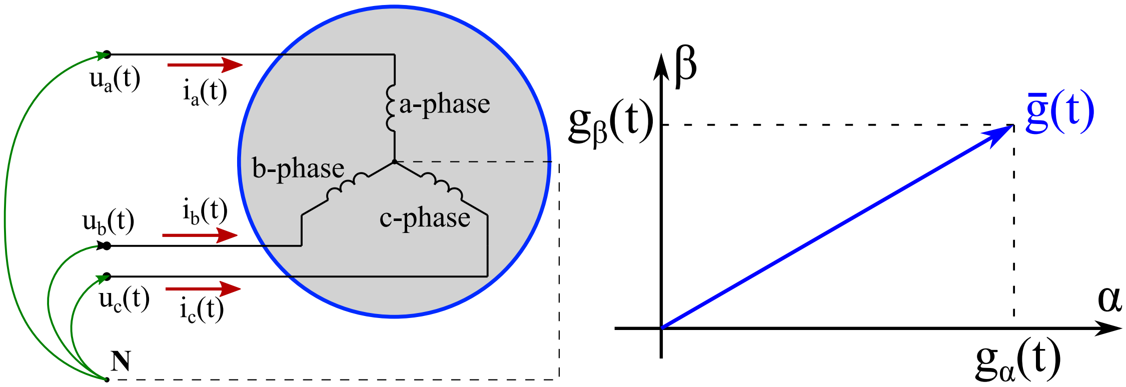

Figure 1.1: Three phase motor and space vector representation.

In vectorial form we can define:

- Line-to-neutral voltages vector: $\vec{u}_{ln} = \left[u_a, u_b, u_c\right]$ [V];
- Line-to-line voltages vector: $\vec{u}_{ll} = \left[u_{ab}, u_{bc}, u_{ca}\right]$ [V];
- Phase currents vector: $\vec{i} = \left[i_a, i_b, i_c\right]$ [A];

If it is considered a balanced three phase system where the *zero sequence* is equal to zero, ie:

$$g_o(t) = \frac{g_a(t) + g_b(t) + g_c(t)}{3} = 0 \tag{1.1}$$

It can be here introduced the complex function that links the generic quantity $\left[g_a, g_b, g_c\right]$ to a vector in the complex plane $\alpha\beta$:

$$\vec{g}(t) = \frac{2}{3}\left[g_a(t) + g_b(t)e^{j\frac{2\pi}{3}} + g_c(t)e^{j\frac{4\pi}{3}}\right] \tag{1.2}$$

Equation 1.2 defines a mathematical association between the three phase quantity and a single vector $\vec{g}(t)$ also called *Spatial Vector*. In the plane $\alpha\beta$ this vector has two components $\vec{g}(t) = g_\alpha(t) + jg_\beta(t)$, where the real part can be obtained by:

$$Re[\vec{g}(t)] = g_\alpha(t) = \frac{2}{3}\left[g_a(t) - \frac{g_b(t)}{2} - \frac{g_c(t)}{2}\right] \tag{1.3}$$

And the imaginary part comes from:

$$im[\vec{g}(t)] = g_\beta(t) = \frac{2}{3}\left[\frac{\sqrt{3}}{2}g_b(t) - \frac{\sqrt{3}}{2}g_c(t)\right] \tag{1.4}$$

With the equations 1.2 it has been defined the transformation between a generic three phase system and an equivalent bi-phase ($\alpha\beta$) system, and the two other equations 1.3 and 1.4 give two orthogonal components of the vector in $\alpha\beta$ plane. Still in the case of balanced system it can be defined the inverse transformation that returns us the three phase components from the spatial vector. If we observe the equation 1.3 it can be seen that the real part is equal to the component $g_a(t)$ of the three phase system. This is the reason why the α-axis is also called a-axis as it can be seen in figure 1.2.

If we think of applying the rotation of $e^{-2\pi/3}$ to the spatial vector $\vec{g}(t)$ and then we evaluate the real part of this rotated vector we obtain the component $g_b(t)$, in short:

$$Re[\vec{g}_b(t)] = Re[\vec{g}(t)e^{-j\frac{2\pi}{3}}] = -\frac{g_\alpha(t)}{2} + \frac{\sqrt{3}g_\beta(t)}{2} = g_b(t) \tag{1.5}$$

In this way it is obtained the $g_b(t)$ from the projection on the real axis of the spatial vector $\vec{g}_b(t)$ which is the original one rotated of 120 degrees in clockwise direction. It can be done the same for $g_c(t)$ but in this case the spatial vector has to be rotated of 240 degrees. Graphically it is visible that it is the same if we leave the spatial vector in its initial position but now we rotate the axis on which we do the projection of 120 and 240 degrees in anticlockwise direction as in the figure 1.3.

If we introduce the zero sequence component we can again do the same passages previously seen but differently from before we have to take into account the value of zero sequence component in such a way to obtain all the information taken from the spatial vector. In other words now we have a system with three degrees of freedom and we need

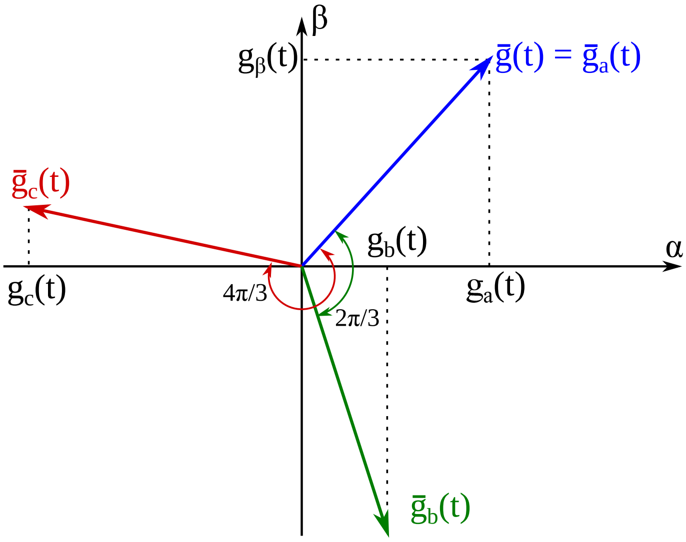

Figure 1.2: Spatial vector definition in an $\alpha\beta$ reference.

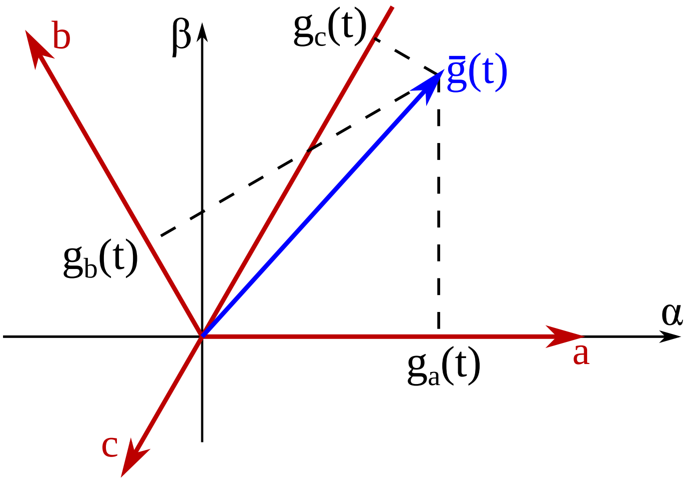

Figure 1.3: Returning of the starting quantities from the spatial vector.

three different equations. The generic transformation can now be written as follows:

$$\begin{cases} g_\alpha(t) = \frac{2}{3}\left[g_a(t) - \frac{g_b(t)}{2} - \frac{g_c(t)}{2}\right] \\ g_\beta(t) = \frac{2}{3}\left[\frac{\sqrt{3}}{2}g_b(t) - \frac{\sqrt{3}}{2}g_c(t)\right] \\ g_o(t) = \frac{1}{3}\left(g_a(t) + g_b(t) + g_c(t)\right) \end{cases} \tag{1.6}$$

And inverted transformation is:

$$\begin{cases} g_a(t) = g_\alpha(t) + g_\beta(t) + g_o(t) \\ g_b(t) = -\frac{1}{2}g_\alpha(t) + \frac{\sqrt{3}}{2}g_\beta(t) + g_o(t) \\ g_c(t) = -\frac{1}{2}g_\alpha(t) - \frac{\sqrt{3}}{2}g_\beta(t) + g_o(t) \end{cases} \tag{1.7}$$

All these equations can be grouped in a more compact way using the matricial form.

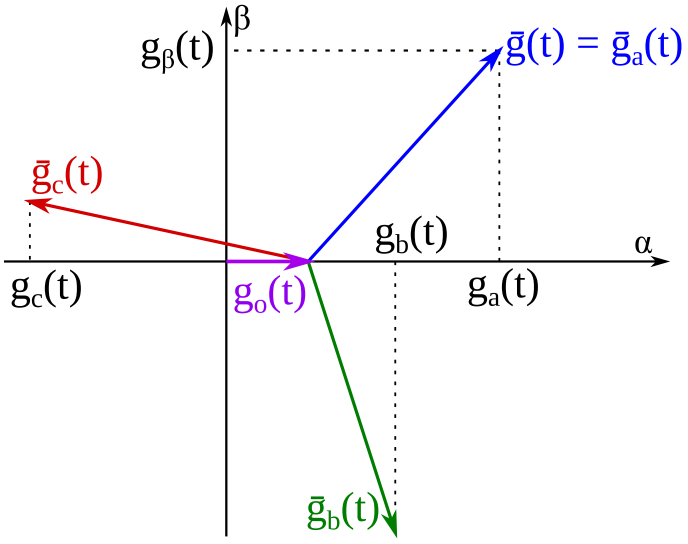

Figure 1.4: determination of g_a, g_b, g_c for an unbalanced system.

Here we define the expression:

$$g_{\vec{\alpha\beta o}} = \left[\vec{T}_{abc\quad\alpha\beta o}\right] \cdot g_{\vec{abc}} \tag{1.8}$$

where the matrix $\left[\vec{T}_{abc\quad\alpha\beta o}\right]$ is the expression of the system 1.6, so it is given by:

$$\left[\vec{T}_{abc\quad\alpha\beta o}\right] = \frac{2}{3}\begin{bmatrix} 1 & -\frac{1}{2} & -\frac{1}{2} \\ 0 & \frac{\sqrt{3}}{2} & -\frac{\sqrt{3}}{2} \\ \frac{1}{2} & \frac{1}{2} & \frac{1}{2} \end{bmatrix} \tag{1.9}$$

In an similar way it is defined the matricial form of 1.7:

$$g_{\vec{abc}} = \left[\vec{T}_{\alpha\beta o\quad abc}\right] \cdot g_{\vec{\alpha\beta o}} \tag{1.10}$$

where the matrix $\left[\vec{T}_{\alpha\beta o\quad abc}\right]$ is given by:

$$\left[\vec{T}_{\alpha\beta o\quad abc}\right] = \begin{bmatrix} 1 & 0 & 1 \\ -\frac{1}{2} & \frac{\sqrt{3}}{2} & 1 \\ -\frac{1}{2} & -\frac{\sqrt{3}}{2} & 1 \end{bmatrix} \tag{1.11}$$

From the previously written equations it can be introduced the instantaneous power absorbed by the three phase load:

$$p(t) = u_a(t)i_a(t) + u_b(t)i_b(t) + u_c(t)i_c(t) \tag{1.12}$$

that can be translated in the $\alpha\beta$ system using 1.11:

$$p(t) = \frac{3}{2}\left[u_\alpha(t)i_\alpha(t) + u_\beta(t)i_\beta(t)\right] + 3u_o(t)i_o(t) \tag{1.13}$$

From equation 1.13 it can be noticed that this transformation is not conservative for the electric power, indeed the formula has to be corrected with the 3/2 term in such a way to have the real power of the system. In case of a balanced system the zero sequence components are null and the equation 1.13 can be simplified to:

$$p(t) = \frac{3}{2} Re\left[\vec{u}(t)\vec{i}(t)\right] \tag{1.14}$$

where $\vec{u}(t)$ is the spatial vector associated to the balanced system voltages, and $\vec{i}(t)$ is the conjugate if the currents spatial vector.

1.1.1 dq coordinates system

In the field of electrical synchronous machines is often convenient to define a coordinate system which is rotating. In particular it is introduced the dq coordinate system with axis fixed on the rotor in such a way that its movement is synchronous whit the rotor one. Between the two systems $\alpha\beta$ and dq there is a different speed, and if $\alpha\beta$ is fixed (stationary system) it can be called ω the angular speed between the two systems.

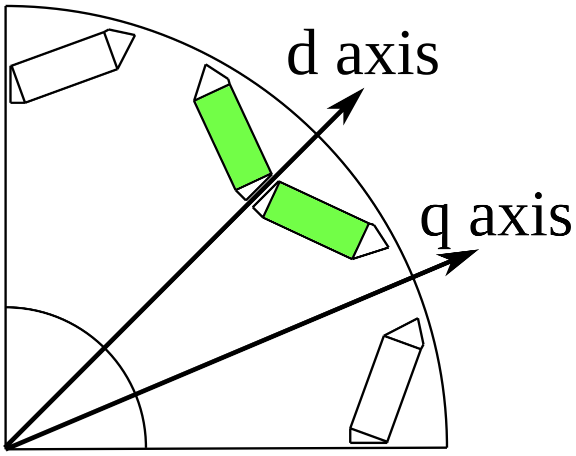

Figure 1.5: dq-axis system definition for an IPM machine.

Now it can be introduced the transformation which connect the two systems:

$$\vec{g}_{\alpha\beta} = \vec{g}\ e^{j(\gamma_{dq}+\vartheta_{dq})} = \vec{g}\ e^{j\gamma_{dq}} + e^{j\vartheta_{dq}} = \vec{g}_{dq}e^{j\vartheta_{dq}} \tag{1.15}$$

And so it can be called:

$$\vec{g}_{dq} = \vec{g}_{\alpha\beta}e^{-j\vartheta_{dq}} \tag{1.16}$$

This equation can be traduced in a matricial form:

$$\begin{bmatrix} g_d \\ g_q \end{bmatrix} = \begin{bmatrix} cos(\vartheta_{dq}) & sin(\vartheta_{dq}) \\ -sin(\vartheta_{dq}) & cos(\vartheta_{dq}) \end{bmatrix} \begin{bmatrix} g_\alpha \\ g_\beta \end{bmatrix} = \begin{bmatrix} \vec{T}_{\alpha\beta \quad dq} \end{bmatrix} \begin{bmatrix} g_\alpha \\ g_\beta \end{bmatrix} \tag{1.17}$$

In equation 1.17 the matrix is orthonormal and for this reason its inverse coincides with its transposed. Due to this fact the transformation $\alpha\beta$ dq and vice-versa are conservative to the powers hence the power calculated in dq system has to be multiplied by $3/2$.
In the most general case it has to be introduced the zero sequence component in the transformation, therefore the matrix becomes:

$$\left[\vec{T}_{dqo\quad\alpha\beta o}\right] = \begin{bmatrix} cos(\vartheta_{dq}) & sin(\vartheta_{dq}) & 0 \\ -sin(\vartheta_{dq}) & cos(\vartheta_{dq}) & 0 \\ 0 & 0 & 1 \end{bmatrix} \tag{1.18}$$

Through the application of the matrices 1.9 and 1.18 it can be obtained the complete matrix associated to the transformation $abc \quad dqo$:

$$\left[\vec{T}_{abc\quad dqo}\right] = \frac{2}{3}\begin{bmatrix} cos(\vartheta_{dq}) & cos(\vartheta_{dq}-2\pi/3) & cos(\vartheta_{dq}-4\pi/3) \\ -sin(\vartheta_{dq}) & -sin(\vartheta_{dq}-2\pi/3) & -sin(\vartheta_{dq}-4\pi/3) \\ 1/2 & 1/2 & 1/2 \end{bmatrix} \tag{1.19}$$

These equations are needed to explain the various types of motors presented below.

1.1.2 dq inductances

In electrotechnic the inductance is simply defined as:

$$L = \frac{\phi}{i} \tag{1.20}$$

Where ϕ is the *flux density* and i is the current that produces the flux. Again ϕ can be obtained from the law:

$$\phi = \int_{\Delta S} (B \cdot n) dS \tag{1.21}$$

The equation 1.21 can be simplified if the surface if maintained fixed, and becomes the easier: $\phi = B \cdot S$.
In the case of a synchronous machine the surface S is related to the area of a pole, in other words:

$$S = S_{pole} = \frac{\pi D}{p} \cdot L_{stk} \tag{1.22}$$

The flux density has to be evaluated as the first harmonic of the air-gap induction: $B = \hat{B}_g$. The two inductances L_d and L_q are necessary to understand the model of the Synchronous motor. They can now be introduced as:

$$\begin{cases} L_d = \frac{\phi_d}{i_d} \\ L_q = \frac{\phi_q}{i_q} \end{cases} \tag{1.23}$$

The figure 1.6 below show the flux density of d-axis and q-axis for a six poles reluctance motor.
The synchronous motors can be classified in basis to type of the rotor, in particular it can be observed that if the Permanent Magnets are on the surface of the rotor then the d,q inductances are the same because is indifferent the rotor position in the production of the flux density by the stator currents. In other words if the PMs are on the surface the rotor is an *isotropic* one and $L_d = L_q$. In the other cases in which the magnets are inside the rotor, or there are only rotor barriers without magnets the d and q axis inductances are different, and this is due to the difference in the permeability of the flux paths in the rotor. This can be seen in figure 1.6.This type of electric machine is also called *anisotropic*.

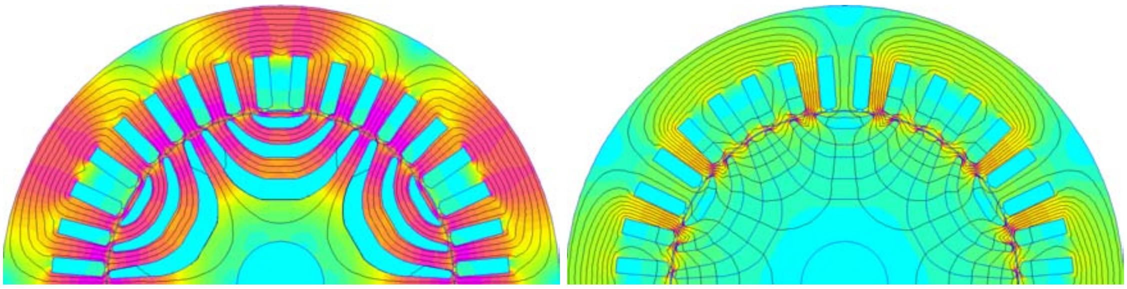

Figure 1.6: Example of d-axis and q-axis fluxes in a reluctance machine

1.2 Surface Permanent Magnet Motors

The SPM motor is manufactured in such a way to put the PMs on the rotor surface in front of the air-gap. The stator is similar to the typical IM one where is placed a poly-phase winding.

Figure 1.7: Example of a SPM rotor.

The electro-mechanic conversion is based on the interaction between stator flux density produced by electric currents in the conductors and magnetic fields created by the PMs. In the figure 1.8 is represented the disposition of PMs on the rotor and conductors in the stator. The PMs create a *no-load* induction at the air-gap which is similar to a square-wave one 1.8(a). On the contrary, it can be supposed a sinusoidal distribution of conductors in front to the air-gap. This disposition leads to a sinusoidal waveform of the induction produced by the stator currents 1.8.
Due to the magnet disposition on the rotor the motor is an isotropic machine and the direct axis and the quadrature axis inductances are equal.

1.2.1 SPM $\alpha\beta$ model

To describe the operation behaviour of a SPM motor the general voltage equations are introduced:

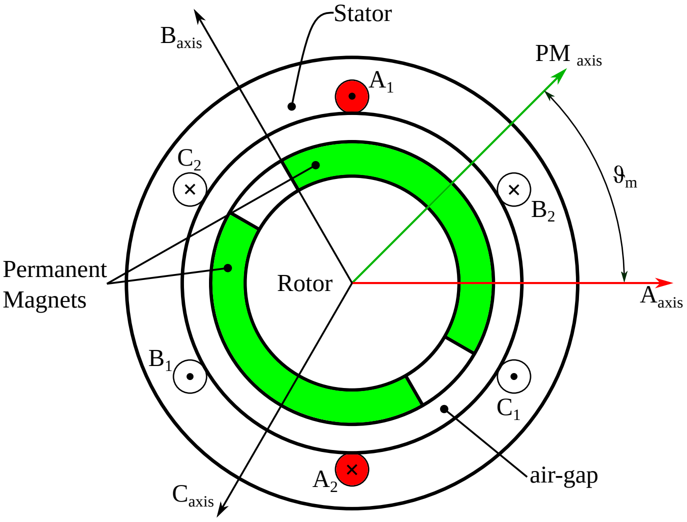

Figure 1.8: Main definitions of a SPM machine

$$\begin{cases} u_a(t) = Ri_a(t) + \frac{d\lambda_a(t)}{dt} = Ri_a(t) + \frac{d}{dt}\left(\lambda_{a,mg}(t) + \lambda_{a,i}(t)\right) \\ u_b(t) = Ri_b(t) + \frac{d\lambda_b(t)}{dt} = Ri_b(t) + \frac{d}{dt}\left(\lambda_{b,mg}(t) + \lambda_{b,i}(t)\right) \\ u_c(t) = Ri_c(t) + \frac{d\lambda_c(t)}{dt} = Ri_c(t) + \frac{d}{dt}\left(\lambda_{c,mg}(t) + \lambda_{c,i}(t)\right) \end{cases} \tag{1.24}$$

In these equations there are (u_a, u_b, u_c) that are phase-to-neutral voltages. (i_a, i_b, i_c) are the phase currents and $(\lambda_a, \lambda_b, \lambda_c)$ are the fluxes concatenated by the phases. Through the hypothesis of *absence of iron saturation* these fluxes have been separated in λ_{mg} which is the PM contribution to the flux and λ_i that is the current produced flux.

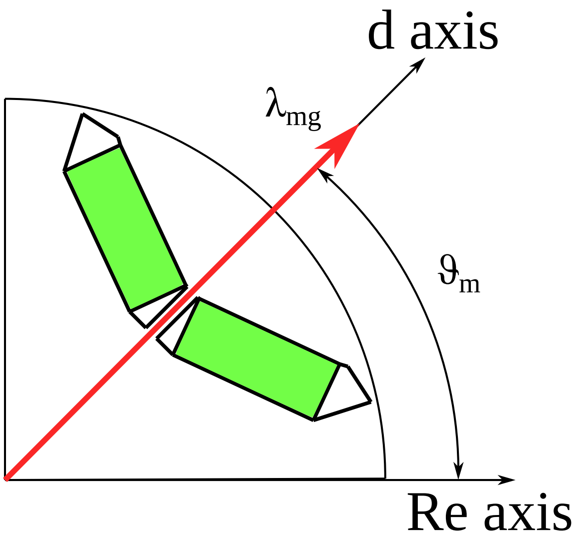

Figure 1.9: PM flux representation in a generic interior permanent magnet machine

If now the spatial vector equations are introduced 1.2 the model in *abc* can be translated in the stationary coordinate system $\alpha\beta$. In particular the concatenated flux due to the PMs is described by:

$$\lambda^s_{mg} = \Lambda_{mg} e^{j\theta_{me}} \tag{1.25}$$

Due to isotropic structure of the machine the self-inductances and the mutual-inductances are equal, in other words the following simplification can be introduced:

$$L_a = L_b = L_c = L_{ss} \tag{1.26}$$

$$L_{M,ab} = L_{M,bc} = L_{M,ca} = -L_{Mss} \tag{1.27}$$

In this way the total flux linkage can be written as:

$$\begin{cases} \lambda_a = L_{ss} i_a - \ L_{Mss} \ (i_b + i_c) + \Lambda_{a,mg} \\ \lambda_b = L_{ss} i_b - \ L_{Mss} \ (i_a + i_c) + \Lambda_{b,mg} \\ \lambda_c = L_{ss} i_c - \ L_{Mss} \ (i_a + i_b) + \Lambda_{c,mg} \end{cases} \tag{1.28}$$

In this system it is usually verified that the sum of phase currents is equal to zero: $i_a + i_b + i_c = 0 \ \forall t$. In this condition it can be defined the *synchronous inductance* as: $L = L_{ss} + L_{Mss}$.
Now the voltage equations can be particularized using the synchronous inductance:

$$\begin{cases} u_a(t) = Ri_a(t) + L\frac{di_a}{dt} + e_a \\ u_b(t) = Ri_b(t) + L\frac{di_b}{dt} + e_b \\ u_c(t) = Ri_c(t) + L\frac{di_c}{dt} + e_c \end{cases} \tag{1.29}$$

In the previous equations have been introduced the back-electromotive forces due to the PMs movement with respect the stator windings.

$$\begin{cases} e_a(t) = \frac{d\lambda_{a,mg}}{dt} = \Lambda_{mg}\omega_{me} cos(\theta_{me} + \pi/2) \\ e_b(t) = \frac{d\lambda_{b,mg}}{dt} = \Lambda_{mg}\omega_{me} cos(\theta_{me} + \pi/2 - 2\pi/3) \\ e_c(t) = \frac{d\lambda_{c,mg}}{dt} = \Lambda_{mg}\omega_{me} cos(\theta_{me} + \pi/2 - 4\pi/3) \end{cases} \tag{1.30}$$

In the previously cited equations there is the quantity ω_{me} which is the electro-mechanic speed and can be obtained by the system frequency as:

$$\omega_{me} = 2\pi f \tag{1.31}$$

If is known the rational in [rpm] the frequency can be defined as:

$$f = \frac{pn}{60} = \frac{p\omega_m}{2\pi} \tag{1.32}$$

Assuming a star-connected winding on the stator it can be defined the rms value of the back-emf as:

$$E_{ll,rms} = \sqrt{3} E_{ln,rms} = \frac{\sqrt{3}}{\sqrt{2}}\hat{E} = \frac{\sqrt{3}}{\sqrt{2}}\omega_{me}\Lambda_{mg} = \frac{\sqrt{3}}{\sqrt{2}} p\omega_m\Lambda_{mg} \tag{1.33}$$

Being the back-emf a balanced triad of sinusoidal waves *free from the zero sequence component* it is possible to write them as spatial vector:

$$\mathbf{u}^s = R\mathbf{i}^s + L\frac{d\mathbf{i}^s}{dt} + \mathbf{e}^s \tag{1.34}$$

where the vector $\mathbf{e}^s$ is the spatial vector associated to the back-emf triad:

$$\mathbf{e}^s = j\omega_{me}\lambda_{mg}^s \tag{1.35}$$

If the equation 1.34 is decomposed in its real and imaginary parts it is obtained:

$$\begin{cases} u_\alpha = Ri_\alpha + L\frac{di_\alpha}{dt} - \omega_{me}\lambda_{\alpha,mg} \\ u_\beta = Ri_\beta + L\frac{di_\beta}{dt} - \omega_{me}\lambda_{\beta,mg} \end{cases} \tag{1.36}$$

From the energetic balance in $\alpha\beta$ system and remembering that the transformation is not conservative for the powers, it can be defined the expression of the torque as:

$$m = \frac{3}{2}p\left[\lambda_{\alpha,mg}i_\beta - \lambda_{\beta,mg}i_\alpha\right] \tag{1.37}$$

This equation can be rearranged in such a way to see the role of the phase shift angle between the spatial vectors of the currents and the stator flux:

$$m = \frac{3}{2}pIm\left[i_s^s \cdot \lambda_s^s\right] = \frac{3}{2}p\ \ i_s\ \ \ \lambda_s\ \ sin(\theta_i^\lambda) \tag{1.38}$$

1.2.2 SPM dq model

Through the transformation in dq coordinates 1.15 and its matrix 1.17 it can be decided to express the spatial vectors in the rotating coordinate system. We assume that this dq coordinates system is synchronous with the rotor, i.e. it is rotating at the speed ω_{me} and the d-axis is placed on the rotor polar axis. In this way the spatial vector associated to the PMs flux has only the real component and this leads to a simplification in the formulation.

$$u^r = Ri^r + L\frac{di^r}{dt} + j\omega_{me}Li^r + j\omega_{me}\Lambda_{mg} \tag{1.39}$$

This relation can be decomposed in the real and imaginary components:

$$\begin{cases} u_d = Ri_d + L\frac{di_d}{dt} - \omega_{me}Li_q \\ u_q = Ri_q + L\frac{di_q}{dt} - \omega_{me}Li_d + \omega_{me}\Lambda_{mg} \end{cases} \tag{1.40}$$

As seen in the previous section it can be obtained the expression of the torque from the energetic balance. It is necessary to multiply u_d by $i_d dt$ and u_q by $i_q dt$ and then summing them term to term. From the term $\omega_{me}\Lambda_{mg}i_q dt$ it is obtained the torque equation remembering the relation $\omega_{me} = p\omega_m$ and the $3/2$ term due to the non conservative aspect of the abc to dq transformation:

$$m = \frac{3}{2}p\Lambda_{mg}i_q \tag{1.41}$$

In this equation there is a direct dependence of the torque from the q current component and this means that in dq plane the ISO-TORQUE curves are horizontal lines.

1.2.3 SPM operating regions

First of all has to be said that each machine has to respect the voltage and current limits. These limits are specified in the nominal values of the motor and power supply. To determine the operating conditions of the machines it is assumed that the operations is in *steady state*. With steady state is identified that operation in which voltages and currents are sinusoidal wave form with constant amplitude and frequency, and the rotational speed

ω_m is constant and fixed as Ω_m. Hence in steady state operations the electric quantities in dq synchronous system are constant and denoted as: U_d, U_q, I_d, I_q.
The current limit can be defined with:

$$I_d^2 + I_q^2 \leq I_N^2 \tag{1.42}$$

where I_N is the amplitude of the spatial vector of stator currents, corresponding to the nominal value of the phase current. With the previously defined matrices is equal to: $I_N = \sqrt{2} I_{nom}$. Analogously the voltage limit is:

$$U_d^2 + U_q^2 \leq U_N^2 \tag{1.43}$$

where is: $U_N = \sqrt{\frac{2}{3}} U_{nom}$.
In a SPM, if it is considered extinct the initial transient and assuming steady state operation, the equations 1.40 become:

$$\begin{cases} U_d = RI_d - \Omega_{me} L I_q \\ U_q = RI_q + \Omega_{me} L I_d + \Omega_{me} \Lambda_{mg} \end{cases} \tag{1.44}$$

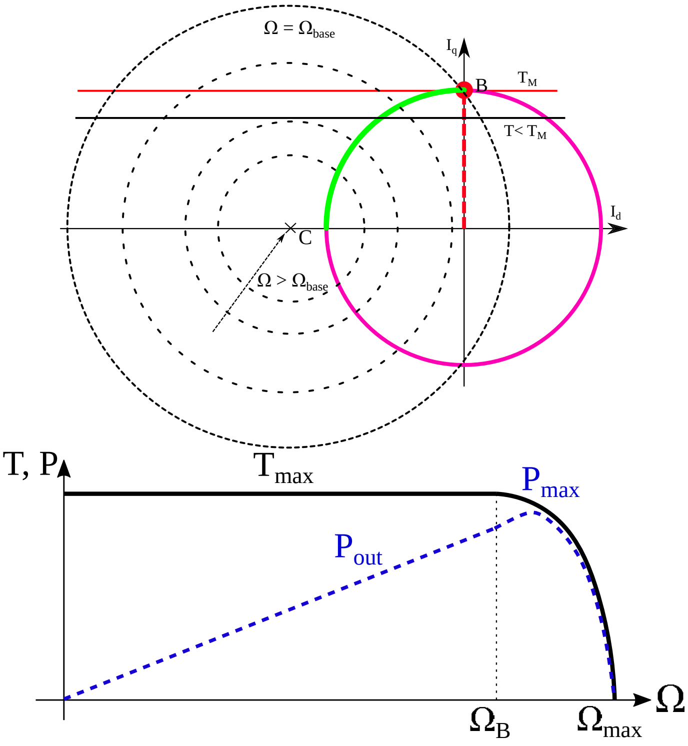

Figure 1.10: Operation limits for a SPM with $I_{C,d} \geq I_N$ and example of torque and power curves in the same SPM motor.

These two equations 1.44 can be put into the 1.43 equation, and neglecting the resistance voltage drop it is obtained:

$$(\Omega_{me} L I_q)^2 + (\Omega_{me} L I_d + \Omega_{me} \Lambda_{mg})^2 \leq U_N^2 \tag{1.45}$$

which rearranged becomes:

$$\left(I_d + \frac{\Lambda_{mg}}{L}\right)^2 + I_q^2 \le \frac{U_N^2}{\Omega_{me}^2 L^2} \tag{1.46}$$

This 1.46 is the equation of a circumference of radius dependent on the electro-mechanic speed $(U_N^2/\Omega_{me}^2 L^2)$ and centred in the point $(I_{C,d}, I_{C,q}) = (\frac{\Lambda_{mg}}{L}, 0)$.
In the figure 1.10 it can be noted the line from the axis origin to B, this segment is the MTPA loci (Maximum Torque per Ampere), on which there is tangency between ISO-TORQUE lines and the current limits. In the picture we can also see the *base speed* where the voltage limit circumference touches points B. Until the base speed the motor is able to produce its maximum torque and above that point the torque decreases because the working point follows the current limit and rotates in anticlockwise direction (for example L point). In these points the torque is lower because it depends directly from i_q current reduction.

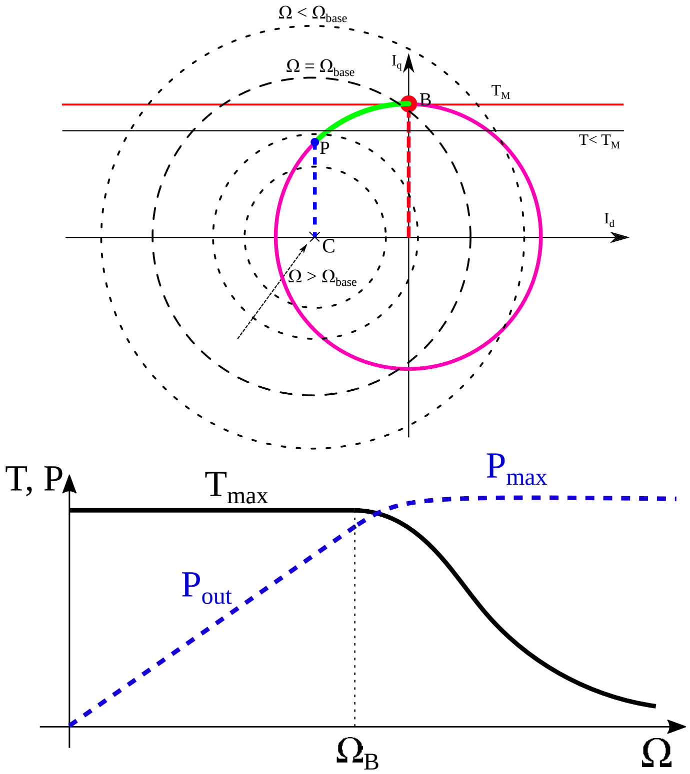

Figure 1.11: Operation limits for a SPM with $I_{C,d} \le I_N$ and example of torque and power curves in the same SPM motor.

If the centre of the voltage limits is inside the current limit than exist a point P where Iso-torque line is tangent to the voltage limit. In this condition is convenient to supply the motor with a current such that the motor works on the vertical line which passes through the short-circuit current as can be seen in figure 1.11. This vertical line is also called MTPV loci (Maximum Torque per Volts).

1.3 Interior Permanent Magnet Motors

If the PMs are disposed in the rotor in such a way to create a difference in the dq-axis paths then we have an IPM. In an IPM the rotor structure loses its isotropy and presents, in non saturation conditions, a marked difference in the values of the d and q axis inductances. This is due to the fact that PMs are characterized by a permeability similar to the air's one. The electro-mechanic conversion follows the two principles of the electro-dynamic and reluctance systems hence the output torque is the composition of these two components.

Figure 1.12: Examples of different rotor structures for actual automotive IPM motors.

1.3.1 IPM dq model

As previously said the dq-axis paths are now different and this makes that the considerations done for the SPM motor are not valid any-more. In particular self and mutual inductances are position-dependent and the dq equations 1.39 are now characterized by a different L_d and L_q:

$$\begin{cases} u_d = Ri_d + L_d \frac{di_d}{dt} - \omega_{me} L_q i_q \\ u_q = Ri_q + L_q \frac{di_q}{dt} - \omega_{me} L_d i_d + \omega_{me} \Lambda_{mg} \end{cases} \tag{1.47}$$

The two inductances are now defined as seen in 1.23. For the IPM motor now it can be obtained the torque expression again from the energetic balance where the u_d and u_q components are multiplied by $i_d dt$ and $i_q dt$ and summed term to term. From the same considerations seen in the SPM section we obtain the torque equation for an IPM:

$$m = \frac{3}{2} p \Lambda_{mg} i_q + \frac{3}{2} p (L_d - L_q) i_d i_q \tag{1.48}$$

If this expression is compared with the SPM one is noted the presence of a further term called *reluctance torque* which is caused by the difference between L_d and L_q. This new term leads to a non linear dependence of the torque by the current. Indeed the IPM torque expression is now an hyperbolic one with two asymptotes: the d-axis and the vertical line $I_d = \Lambda_{mg}/(L_q - L_d)$.

1.3.2 IPM operating regions

To determine the operating conditions of the machines it is assumed that the operations is in *steady state*. Hence the dq electric quantities are constant and denoted as: U_d, U_q, I_d, I_q. The current limit can be defined with 1.42 and the voltage limit is given by 1.43. In an IPM, assuming steady state operation, the equations 1.40 become:

$$\begin{cases} U_d = RI_d - \Omega_{me} L_q I_q \\ U_q = RI_q + \Omega_{me} L_d I_d + \Omega_{me} \Lambda_{mg} \end{cases} \tag{1.49}$$

With the same passages seen in the SPM motor it can now be written:

$$\left(I_d + \frac{\Lambda_{mg}}{L_d} \right)^2 + \left(\frac{L_q}{L_d} I_q \right)^2 \leq \frac{U_N^2}{\Omega_{me}^2 L_d^2} \tag{1.50}$$

Differently from what seen for the SPM motor, now the voltage limit describes an ellipses family centred in $(I_{C,d}, I_{C,q}) = (\frac{\Lambda_{mg}}{L_d}, 0)$. The ellipses axis depends on the L_q/L_d ratio.

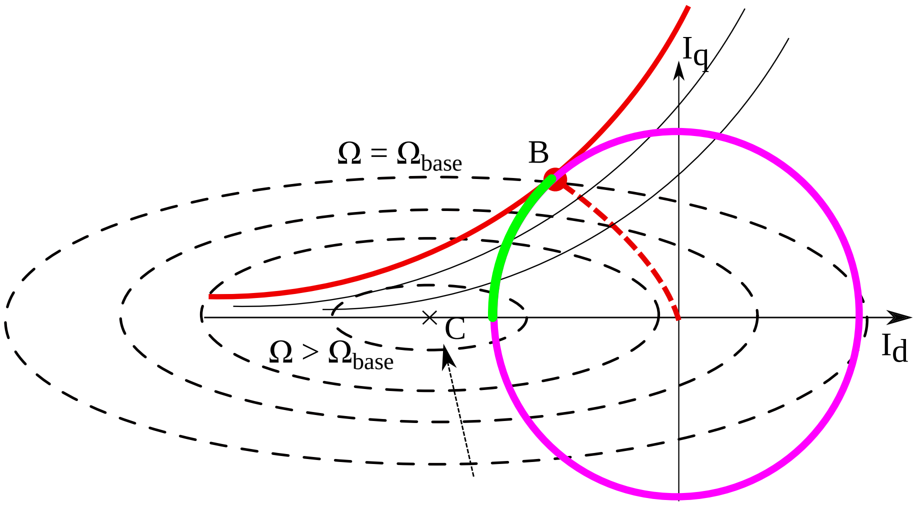

Figure 1.13: Operation limits for an IPM with $I_{C,d} \geq I_N$

The current limit is the same as seen in SPM case. In the IPM the MTPA curve is no longer a vertical line but is a 2-D curve described by the equation 1.51:

$$I_q = \pm\sqrt{\frac{I_d[\Lambda_{mg} + (L_d - L_q)I_d]}{(L_q - L_d)}} \tag{1.51}$$

This expression is obtained by imposing the orthogonality of the tangent to the iso-torque curve with the straight line that connect the axis origin with that point.
If the short-circuit current is lower than the nominal one then the working region of the motor is slightly different at the high speed as seen in the SPM motor (fig. 1.14).

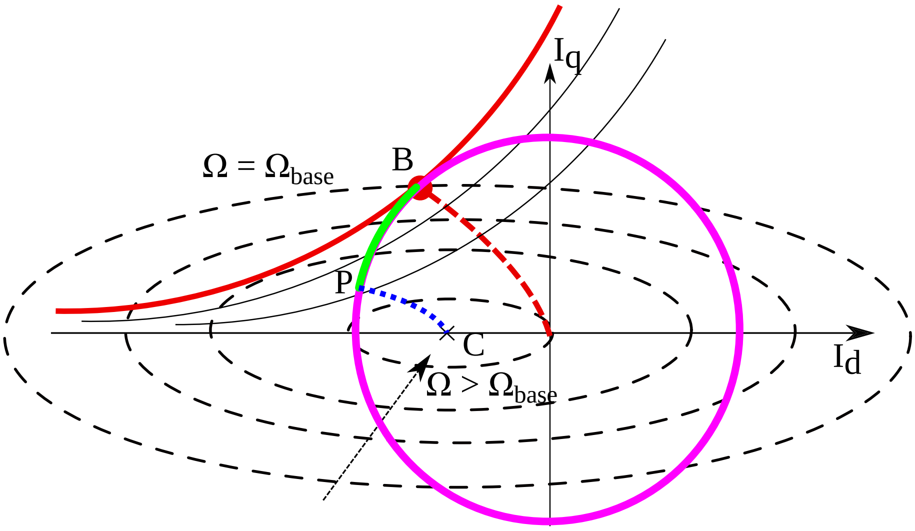

Figure 1.14: Operation limits for an IPM with $I_{C,d} \leq I_N$

In this case there isn't a maximum speed of the motor and after the point P (or P′) is convenient to follow the curve P-to-C which is the MTPV. This curve is obtained equating the tangent point to the iso-torque with the voltage limit ellipses and its expression is:

$$I_q = \pm\frac{L_d}{L_q}\sqrt{\frac{-(I_d + \frac{\Lambda_{mg}}{L_d})[\Lambda_{mg} + (L_d - L_q)I_d]}{(L_q - L_d)}} \tag{1.52}$$

1.4 Synchronous Reluctance Motor

Synchronous reluctance motor is a particular case of an-isotropic machine which is characterized by the absence of PMs in the rotor, hence the output torque is produced only by the reluctance effect.

As noticeable in figure 1.15 the rotor is constituted only of iron laminations in which there are flux barriers. In order to guarantee mechanical stability in the barriers centres is visible the iron link which cause as drawback a magnetic flux leakage.

Figure 1.15: Example of a 4 poles Synchronous Reluctance motor.

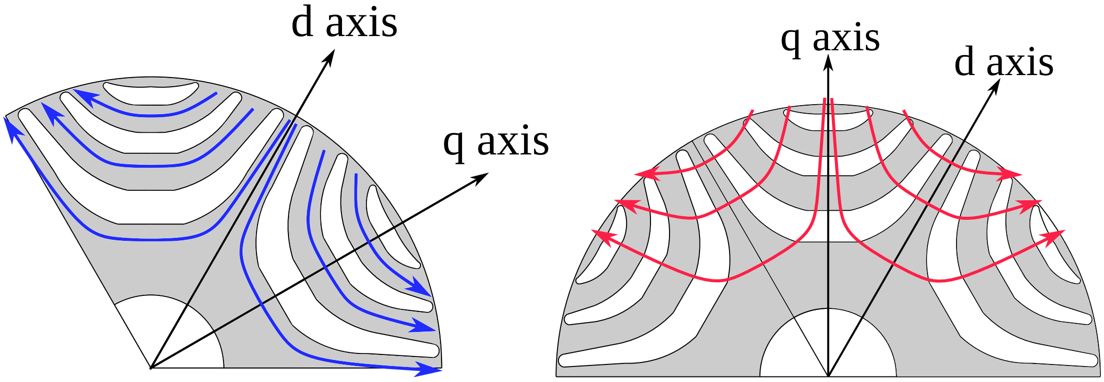

Figure 1.16: Reluctance motor fluxes: blue one is pure d flux and red one is pure q flux.

1.4.1 REL model

As said before synchronous reluctance motor can be seen from the model perspective as a particular case of IPM in which the PM has been removed. In this case the equations that describe this motor are the same of the IPM but without the term related to the PM back-emf. In other words:

$$\begin{cases} U_d = RI_d - \Omega_{me} L_q I_q \\ U_q = RI_q + \Omega_{me} L_d I_d \end{cases} \tag{1.53}$$

Substituting these two equations into the voltage limit it is obtained:

$$(I_d)^2 + \left(\frac{L_q}{L_d} I_q\right)^2 \leq \frac{U_N^2}{\Omega_{me}^2 L_d^2} \tag{1.54}$$

Torque is given by the equation 1.48 private of the PM component:

$$m = \frac{3}{2} p (L_d - L_q) i_d i_q \tag{1.55}$$

1.4.2 REL operating regions

Because of the absence of PM component now the torque hyperbole have as asymptotes the d and q axis. If it is *neglected* the iron *saturation* then the expression of MTPA become:

$$I_q = \pm I_d \tag{1.56}$$

and MTPV:

$$I_d = \pm \frac{L_d}{L_q} I_d \tag{1.57}$$

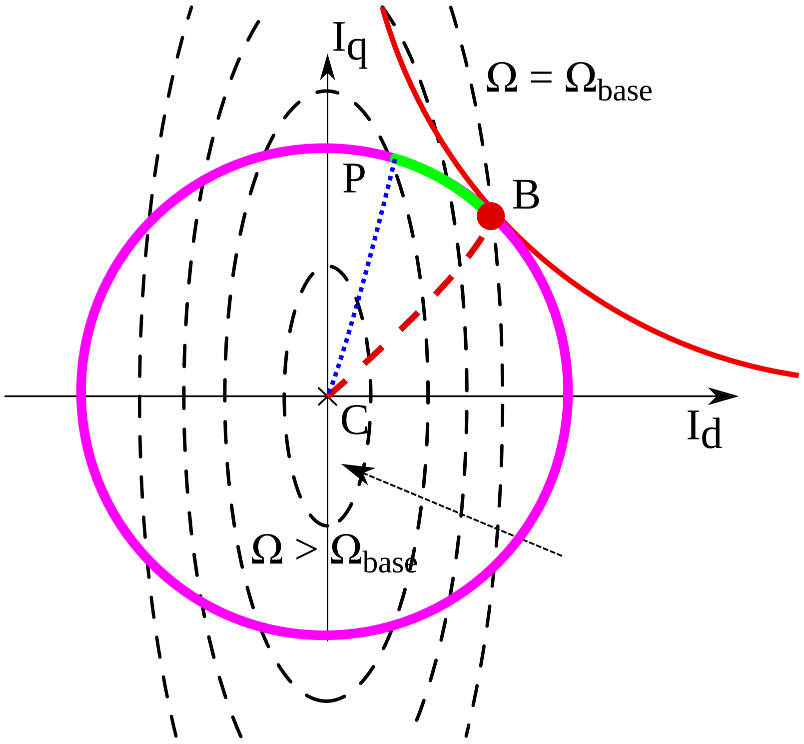

Figure 1.17: Sync. REL operating limits

The pure reluctance motor can be modified in Permanent magnet assisted motor introducing on the -q axis a Ferrite magnet in order to improve flux weakening performances. The resulting operations limits are similar to the IPM ones as shown in figure 1.18

It is important to observe that in the Synchronous Reluctance motor the effect of the Iron Saturation is no longer negligible hence the graphs and equations previously seen have just a qualitative value.

1.4.3 Iron saturation

In presence of iron saturation relations between flux linkage and currents are no longer linear and can present cross-effects (cross-saturation) in which the current af an axis produces flux linkage on the other.

Taking in account the possible saturation the magnetic characteristics become function of the supply current:

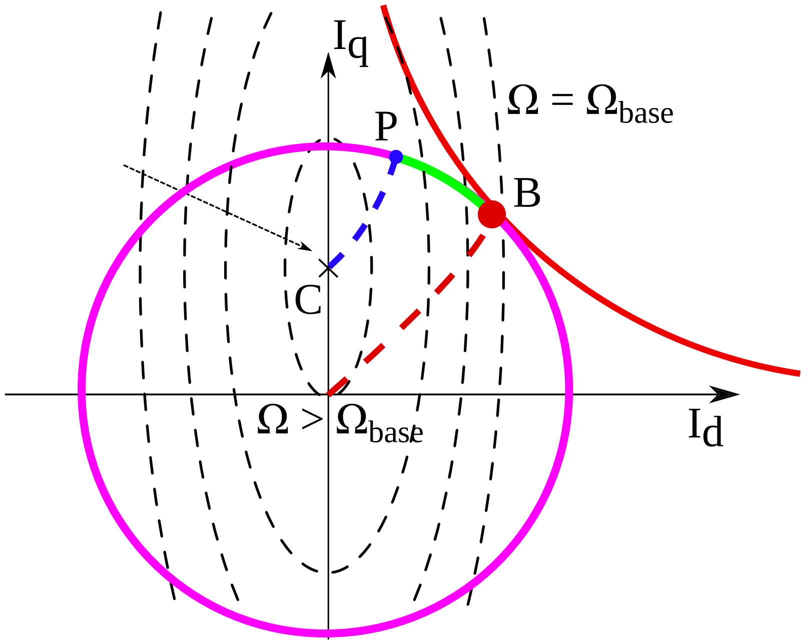

Figure 1.18: Permanent magnet assisted reluctance motor operation limits.

$$\begin{cases} \lambda_d = \lambda_d(i_d) = \Lambda_{mg} + \lambda_{d,i}(i_d) \\ \lambda_q = \lambda_q(i_q) \end{cases} \tag{1.58}$$

In this system the cross-saturation is not taken in account. The voltage equations in rotating reference system are always valid and from them it can be written:

$$\begin{cases} u_d = Ri_d + \frac{d\lambda_d(i_d)}{dt} - \omega_{me}\lambda_q i_q \\ u_q = Ri_q + \frac{d\lambda_q(i_q)}{dt} + \omega_{me}\lambda_d i_d \end{cases} \tag{1.59}$$

Then the terms can be separated as:

$$\begin{cases} u_d = Ri_d + \frac{d\lambda_d(i_d)}{di_d}\frac{di_d}{dt} - \omega_{me}\lambda_q i_q = Ri_d + \tilde{L}_d(i_d)\frac{di_d}{dt} - \omega_{me}\lambda_q i_q \\ u_q = Ri_q + \frac{d\lambda_q(i_q)}{di_q}\frac{di_q}{dt} + \omega_{me}\lambda_d i_d = Ri_d + \tilde{L}_q(i_q)\frac{di_q}{dt} - \omega_{me}\lambda_d i_d \end{cases} \tag{1.60}$$

In these equations 1.60 have been introduced the *differential inductances*:

$$\begin{cases} \tilde{L}_d(i_d) = \frac{d\lambda_d(i_d)}{di_d} \\ \tilde{L}_q(i_q) = \frac{d\lambda_q(i_q)}{di_q} \end{cases} \tag{1.61}$$

These inductances represents the slope of the magnetic characteristics in each point. *Apparent inductances* are defined as:

$$\begin{cases} L_d(i_d) = \frac{\lambda_d(i_d) - \Lambda_{mg}}{i_d} \\ L_q(i_q) = \frac{\lambda_q(i_q)}{i_q} \end{cases} \tag{1.62}$$

These apparent inductances are the slope of the straight lines that connect the point in exam of the magnetic characteristic with the point $(0, \Lambda_{mg})$ or with the origin of the axis. The dq torque expression 1.48 maintain its validity also in presence of saturation:

$$m(i_d, i_q) = \frac{3}{2} p \Lambda_{mg} i_q + \left[L_d(i_d) - L_q(i_q) \right] i_d i_q \tag{1.63}$$

If the iron saturation is at higher levels the flux of each axis depends on both the currents and this leads to a most general expression:

$$\begin{cases} \lambda_d = \lambda_d(i_d, i_q) \\ \lambda_q = \lambda_q(i_d, i_q) \end{cases} \tag{1.64}$$

In this case it happens as if exist a mutual coupling between the two axis d and q. This phenomenon is explained by taking in account that there are iron paths commons to the two axis and consequently the saturation of these paths from one of the two axis currents produces a flux variation in the other axis though its current has remain the same.

Chapter 2

Automotive Motors Comparison

This chapter deals with the comparison of actual synchronous motors installed on ″today″ commercial vehicles. First a set of data relative to the automotive power-train has been collected in order to start the analysis. This set of information comes mainly from cars producers, researches of the Oak Ridge National Laboratories [8],[18],[19], and technical documentation of the vehicles [26], [27].

2.1 Terms of comparison

In this section are presented the main comparative terms that have been used to build a performance chart of the automotive motors investigated. These data start from the main geometrical dimension of the motor and want to arrive to the output performance on the basis of FEM simulations.
First of all are needed the geometric parameters of the motors. The following necessary data are the electric ones. From these quantities it is carried out the FEM analysis to obtain the simulated power and torque curves. These outputs are in the end compared with the ones from the producers. Simulated models and the comparison documents found are below reported.

Prius 2004	Prius 2010 (F)	Prius 2010 (P)	Lexus LS 600h
Camry 2014	Accord 2014	LEAF	BMW i3

Table 2.1: Automotive models presented in this chapter.

From the table can be noted that there are models belonging to the same producer. In particular there are three Toyota's geometries (Prius 2004, Prius 2010, Camry 2014). The other geometries belong to different producers but the typology of motor is the same: all these motors are in fact IPM with Neodymium-Iron-Boron Permanent Magnet inside the rotor. PMs disposition changes among the models but there are three main concept: V-shaped, Delta-shaped and I-shaped (horizontally).
IPM means that the output torque is produced by the two components: electro-dynamic and reluctance torque in such a way to maximize the shaft torque.

2.1.1 Design aspects of automotive motors

First step is to define the main dimension of the motor geometry. These geometrical data are reported below:

Model	Q_s	D_{ext}	D_{int}	g	L_{stk}	h_{slot}	w_t	h_{bi}	S_{slot}
Prius 2004	48	269	161.9	0.72	84	32.48	8.34	20.4	145.159
Prius 2010 F	48	269	161.9	0.72	50.8	32.48	8.34	20.4	145.159
Prius 2010 P	48	264	161.9	0.73	50.8	30.9	7.5	18.65	158.452
Lexus 600	48	200	130.86	0.89	135.4	19.25	6	13.32	76.784
Camry	48	264	161.9	0.72	60.7	29.9	8.33	20.5	128.647
Accord	48	292	196.6	0.8	61.7	28.98	8.34	18	160.37
LEAF	48	200	130.86	0.89	151	19.25	6	14	76.784
BMW i3	72	242.1	180	0.8	132.2	17.46	4.1	11.95	68.64

Table 2.2: Geometrical data of the automotive analysed models.

From this table it can be noted that the external diameters belong to the range 200 - 292 [mm], the Stack length to the range 50 - 150 [mm] hence there are different D/L ratios, but the number of slot is always 48 slots except for the BMW case. This is linked to the number of poles which is: $2p = 8$ for every geometry except the BMW one where it is: $2p = 12$. If now it is introduced the number of slot per pole per phase q:

$$q = \frac{Qs}{2p \cdot m} \tag{2.1}$$

From this equation it can be observed that for each studied geometry q is equal to 2. This fact can be related with the easier end winding manufacturing and their lower dimension. From the external diameter and the stack length it can be obtained an approximation of the whole motor volume, and the same with the air-gap diameter and the stack length it is obtained the air-gap volume. These two quantities are necessary to compare the motors in term of power and torque density.

$$Vol_{ext} = \frac{\pi}{4} \cdot D_{ext}^2 \cdot L_{FE} \tag{2.2}$$

$$Vol_{int} = Vol_{air-gap} = \frac{\pi}{4} \cdot D_{int}^2 \cdot L_{FE} \tag{2.3}$$

In the simulations carried out, the conductors in the FEM model have the same length of the stack one hence to have the total conductor length we have to estimate the end-winding length through the next equation [7]:

$$L_{ew} \cong 2.5 \cdot \frac{D_{int}}{p} \tag{2.4}$$

To go ahead with the simulations the electrical supply data are required but these parameters not always appear on the data-sheet of the motors. Hence when they are not provided it is necessary to run a series of simulations on order to obtain an estimation of the slot current. This one is the total current in the slot and it is equal to the number of conductor in the slot multiplied by the conductor's current. The slot current is obtained from the simulation when the average output torque of the motor is equal or similar to the one on the data-sheet. Finally the conductor's current is obtained dividing the slot current by the number of conductor in the slot. DC bus voltage and the nominal output values are reported in the table below.

Model	Qs	2p	V_{DC} [V]	T_M [Nm]	$P_{out,max}$ [kW]
Prius 2004 (F)	48	8	500	400	50
Prius 2010 (F)	48	8	650	207	60
Prius 2010(P)	48	8	650	207	60
Lexus 600 (P)	48	8	650	300	165
Camry (F)	48	8	650	270	105
Accord M (I)	48	8	700	300	124
Nissan LEAF (I)	48	8	375	280	80
BMW i3 (I)	72	12	360	250	125

Table 2.3: DC bus voltage, Power and Torque declared producer values

The initial simulation of the various motor have been carried out as if in the slot there would have been a single conductor in which flows the total current [4]. In other words, in the first simulation, the number of conductors in the slot n_c has been fixed equal to one. The same with the parallel path of the machine $n_{pp} = 1$. In this way:

$$n_{cs} = \frac{n_c}{n_{pp}} = 1 \tag{2.5}$$

With $n_{cs} = 1$ it can be obtained an equivalent number of conductor in series per phase:

$$N_s = \frac{n_{cs} \cdot Qs}{m} \tag{2.6}$$

From the number of series conductor per phase can be estimated the electric load of the machine [7]:

$$\hat{K}_s = \frac{m \cdot K_w \cdot N_s \cdot \hat{I}_c}{\pi D_{int}} \tag{2.7}$$

In the equation 2.7 have been introduced: m which is the number of phases of the machine, K_w that is the *winding factor* and takes in account the distribution of the windings at the air-gap. Last one is $\hat{I}_c$ which is the slot current *peak value* (if $n_{cs} = 1$) or the conductor current peak value (if it is used the correct number of conductors in the slot). Equation 2.7 gives an estimation of how much the machine is loaded from the electrical point of view. An usual air cooled electric machine can has an electric loading in the range of 30 to 100 [kA/m] but if are introduced most sophisticated cooling systems this range can be increased.

From the previously defined dimensions and electric loading it can be obtained an estimation of the output torque [7]:

$$T = \hat{K}_s \cdot \hat{B}_g \cdot (\frac{\pi}{4} D_{int}^2 \cdot L_{FE}) \tag{2.8}$$

In this equation appear also the term $\hat{B}_g$ which is the peak value of the air-gap flux density.

In order to obtain an initial estimation the $\hat{B}_g$ can be equalized to one which is not so distant from the real air-gap flux densities of an IPM machine. This value will be corrected with the following analysis of the motors.
Another important parameter to realize the electric loading of the investigated motor is the *current density*. Here it is defined the slot current density as:

$$\hat{J}_{slot} = \frac{\hat{I}_{slot}}{S_{slot}} \tag{2.9}$$

And the current density inside the conductor copper as:

$$\hat{J}_{cu} = \frac{\hat{I}_{slot}}{S_{slot} \cdot K_{fill}} \tag{2.10}$$

where $\hat{I}_{slot} = n_{cs} \cdot \hat{I}_c$ and K_{fill} is the *slot fill factor*. This last term is needed to estimate how much slot area is covered by the copper of the conductors. It is a kind of utilization factor of the slot surface. This fill factor not always is given by the data-sheet hence in some geometries it has been supposed. In a normal motor, where there is no need of high loadings the current density is in the range of 5 to 7 $[A/mm^2]$ [7] but with higher loading and better cooling systems this range can be extended.
Finally it will be examined the ratio between output torque and power and the volume in order to obtain the power and torque densities. These values are needed to do the comparison with the designed motors.

2.2 Toyota Prius 2010 (F)

The Prius 2010 motor is presented here. The rotor magnets disposition is V-shaped. The stator is equal to the one of an asynchronous motor and has 48 slots. The "F" points out that this geometry comes from Flux Motor which is a program created expressly to simulate these kind of motors. The main difference compared to the following Prius 2010 model is that this geometry is less precise and more approximated than the one by Pietrini [20].

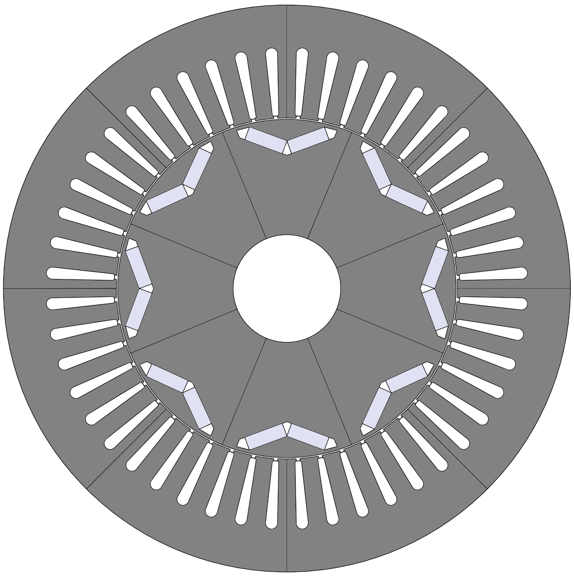

Figure 2.1: Geometry of the Prius 2010 model from Flux

The simulated geometry is here reported fig. 2.1. This figure can be compared with the Pietrini's one in the next section 2.4. The main geometrical data are reported in the table below:

L_{stk} mm	D_{ext} mm	D_i mm	g mm	D_r mm	$D_{r,i}$ mm	PM -	Vol_{ext} l
50.8	269	161.9	0.73	160.44	51	2 V-shape	2.89
h_s mm	$w_{s,i}$ mm	w_t mm	h_{BI} mm	w_{so} mm	τ_p mm	w_{PM} mm	h_{PM} mm
30.9	3.19	8.34	20.4	1.88	63.58	18.9	6.5

Table 2.4: Geometrical data of Prius 2010 from flux.

From the previous geometrical the volumes are evaluated as:

$$Vol_{ext} = \frac{\pi \cdot D_{ext}^2 \cdot L_{iron}}{4} = \frac{\pi \cdot 0.269^2 \cdot 0.0508}{4} = 2.89[l] \tag{2.11}$$

$$Vol_{air-gap} = \frac{\pi \cdot D_{int}^2 \cdot L_{iron}}{4} = \frac{\pi \cdot 0.1619^2 \cdot 0.0508}{4} = 1.05[l] \tag{2.12}$$

The motor performance data are reported in the following table.

Q_s	p	T_{max}	P_{max}	V_{DC}	I_c	n_B	n_{max}
-	-	$[Nm]$	$[kW]$	$[V]$	$[A]$	$[rpm]$	$[rpm]$
48	4	207	60	650	250	2800	13500

Table 2.5: Prius 2010: performance data from the producer

This table shows all the electric data required to carry out the motor simulation and the output parameters that are taken as reference. Conductor current and the reported speeds come from the Pietrini's report [20], power and torque from Toyota technical informations and are confirmed in the report. From an ORNL document [19] it has been possible to obtain the number of conductor in the slot which is equal to:

$$n_c = 11 \tag{2.13}$$

From the number of parallel path knowledge, which is unitary, the equivalent number of series conductor in the slot can be achieved: $n_{cs} = 1$. This is an important number because it is needed to carry out a simulation where the slot is assumed to be filled by one single equivalent conductor. From the knowledge of $\hat{I}_{c,max}$ and n_{cs} the total slot current is obtained as:

$$\hat{I}_{slot,max} = \hat{I}_{c,max} \cdot n_{cs} = 250 \cdot 11 = 2750[A] \tag{2.14}$$

This current is associated with the slot region in the FEM simulation. Hence in this region there is an equivalent conductor which takes the whole current.
The *base speed* is the speed reached when the voltage on the motor equalizes the allowable maximum by the inverter limit. The winding voltage has to be changed in order to comply with the different number of conductor in the simulation. Due to the fact that there is an equivalent single conductor in the slot, at the *base speed* there will be a voltage on it equal to:

$$\hat{V}_{slot} = \frac{V_{DC}/\sqrt{3}}{n_{cs}} = \frac{650/\sqrt{3}}{11} \cong 34[V] \tag{2.15}$$

Hence the first simulation will be carried out with the following equivalent parameter:

Model	n_c	n_{cs}	$\hat{I}_{c,max}$ [A]	$\hat{V}_{c,max}$ [V]
Prius 2010	11	1	2750	34

Table 2.6: Equivalent single conductor electric data used in the first simulation.

From these data, regarding the torque in the base point we gain the following results: $T_{dq} = 283.4$ [Nm] and $T_{maxwell} = 299.1$ [Nm].
These torques are a lot higher than the nominal maximum one which is 207 [Nm]. This is mainly due to the fact that this geometry is approximated by the program and it is not detailed. This happens both in regard to the magnet dimension, which are wider than the real ones, and to the absence of iron link between the magnets.

This leads to an higher flux density at the air-gap hence to higher output torque. The last diversification regards the materials used in the simulation. They could have different properties with respect to the real ones in the motor and these differences are not known. The number of conductor in series per phase is evaluated taking into account the real number of conductors:

$$N_s = \frac{n_{cs} \cdot Qs}{m} = \frac{11 \cdot 48}{3} = 176 \tag{2.16}$$

Finally the electrical loading is given by the equation 2.7:

$$\hat{K}_{s,max} = \frac{3 \cdot 0.9659 \cdot 176 \cdot 250}{\pi 0.1619} = 250674[A/m] \tag{2.17}$$

$$\hat{K}_{s,nom} = \frac{3 \cdot 0.9659 \cdot 176 \cdot 150}{\pi 0.1619} = 150404[A/m] \tag{2.18}$$

In order to evaluate the rated electrical loading, a nominal current equal to 60% of the maximum one has been supposed.

The conductor current density is evaluable by considering the following estimation of the fill factor: $K_{fill} \cong 0.47$ from [20] as:

$$J_{cond} = \frac{2750}{\overline{2} \cdot 145.159 \cdot 0.47} = 28.5[A/mm^2] \tag{2.19}$$

From a single simulation in the base point of the machine the FEM outputs values are grouped in the following table:

PF -	η -	P_{in} $[kW]$	P_{out} $[kW]$	$P_{loss,total}$ $[kW]$
0.65	0.87	95.76	83.11	12.65
$P_{J,s}$ $[W]$	$P_{fe,tooth}$ $[W]$	$P_{fe,BI}$ $[W]$	$P_{fe,total}$ $[W]$	P_{mech} $[W]$
11041	469.2	483.2	952.4	659.6

Table 2.7: Data acquisition in the base point simulation

From these obtained values the following torque and power densities ratios are evaluated:

T_{max}/Vol_{ext} $[Nm/l]$	T_{max}/Vol_{airgap} $[Nm/l]$	$P_{out,max}/Vol_{ext}$ $[kW/l]$	$P_{out,max}/Vol_{airgap}$ $[kW/l]$
98.1	269.9	28.8	79.1

Table 2.8: Torque and power densities of the Prius 2010 (Flux).

The same goes for the losses densities in table 2.9.

$P_{loss,total}/Vol_{ext}$ $[kW/l]$	$P_{loss,total}/Vol_{airgap}$ $[kW/l]$
4.4	12.1

Table 2.9: Loss densities of the Prius 2010 (Flux).

After the base point identification, the torque and power behaviour have to be simulated. To do so the motor mapping is required and it is carried out by a series of simulation changing the d-q axis currents. The map, the torque and power graphs are reported below.

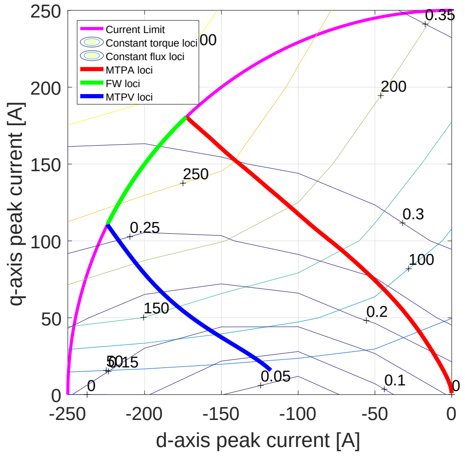

Figure 2.2: Prius 2010 (Flux) dq map.

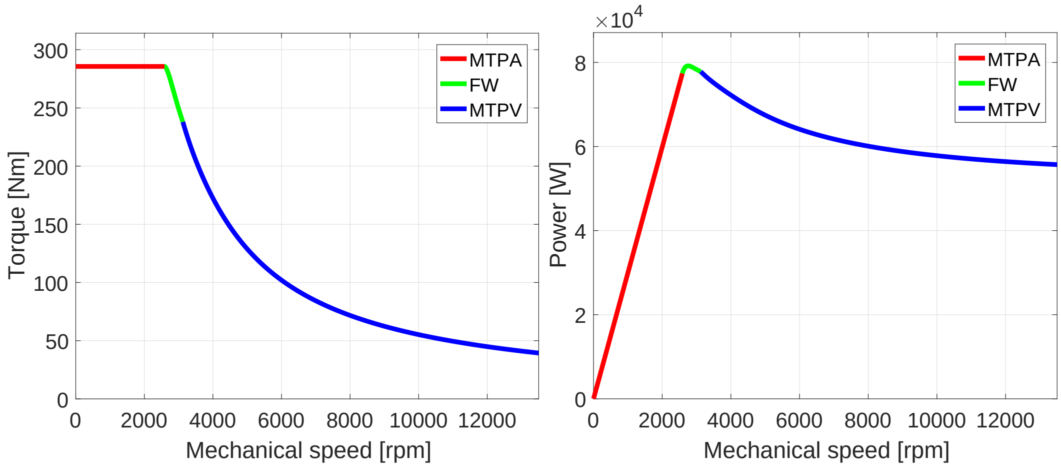

Figure 2.3: Prius 2010 (Flux): Torque and Power vs speed.

2.3 Toyota Prius 2010 (P)

This section illustrates the same motor as before but it is more defined than the previous one in section 2.2, since its geometry derives from Pietrini's report [20]. The stator geometry is the same but with a smaller external diameter which is confirmed by other documents [18], [19].

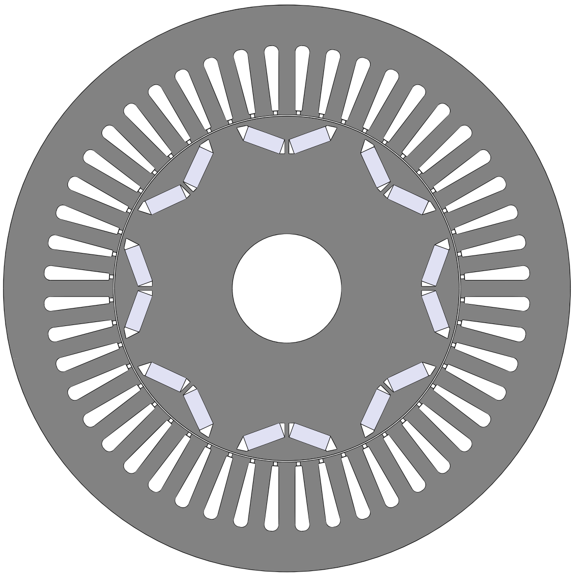

Figure 2.4: Geometry of the Prius 2010 model from Pietrini's document

Another important difference lies in the Permanent Magnets dimension and in the air barrier near the magnet itself. In particular this geometry is characterized by the presence of an iron link between the two V-shaped magnets in such a way to preserve the structural integrity of the rotor. The geometrical data of this motor are reported below.

L_{stk} mm	D_{ext} mm	D_i mm	g mm	D_r mm	$D_{r,i}$ mm	PM -	Vol_{ext} l
50.8	264	161.9	0.73	160.44	51	2 V-shaped	2.78
h_{slot} mm	$w_{slot,i}$ mm	w_t mm	h_{BI} mm	w_{so} mm	τ_p mm	w_{PM} mm	h_{PM} mm
30.9	3.3	7.5	18.65	1.88	63.58	17.88	7.16

Table 2.10: Geometrical data of the model Prius 2010 (Geometry from [20]).

The producer performance data are here reported for convenience.

Table 2.10 highlights some differences from the previous one due to the different external diameter. Another difference is in the slot and tooth width which will cause different flux density and current density values. Most of these data are equal to the motor seen in the previous section, for here appear only the different ones.

Q_s -	p -	T_{max} $[Nm]$	P_{max} $[kW]$	V_{DC} $[V]$	I_c $[A]$	n_B $[rpm]$	n_{max} $[rpm]$
48	4	207	60	650	250	2800	13500

Table 2.11: Prius 2010 (P): Data from the producer

$$Vol_{ext} = \frac{\pi \cdot D_{ext}^2 \cdot L_{FE}}{4} = \frac{\pi \cdot 0.264^2 \cdot 0.0508}{4} = 2.78[l] \tag{2.20}$$

The electric load and the number of conductor are equal. Assuming a $K_{FILL} \cong 0.47$:

$$J_s = \frac{2750}{\overline{2} \cdot 158.452 \cdot 0.47} = 26.1[A/mm^2] \tag{2.21}$$

The base speed in this case has been identified at 3000 [rpm] which slightly higher than the previous section's. This can be justified by the presence of the iron link between the magnets. This causes PM's flux leakage through itself and then there is a lower flux density at the air-gap. This leads to a lower voltage induced in the conductor at the same speed. This worse air-gap flux density leads also to a lower output torque with respect the previous motor. Indeed in the base point the torques are: $T_{dq} = 236.4$ [Nm] and $T_{maxwell} = 261.1$ [Nm]. The same simulation at the base speed has also obtained the following values:

PF -	η -	P_{in} $[kW]$	P_{out} $[kW]$	$P_{loss,total}$ $[kW]$
0.67	0.86	86	74	11.78
$P_{J,s}$ $[W]$	$P_{fe,tooth}$ $[W]$	$P_{fe,BI}$ $[W]$	$P_{fe,total}$ $[W]$	P_{mech} $[W]$
10115	505.8	553.5	1060	610.2

Table 2.12: Data acquisition in the base point simulation.

The torques are worsened with respect the previous section motor and this is confirmed by [20] where there is an evaluation of this motor with and without the iron link between the magnets.

The following ratios are obtained from the base point values at the maximum available torque:

T_{max}/Vol_{ext} $[Nm/l]$	T_{max}/Vol_{airgap} $[Nm/l]$	$P_{out,max}/Vol_{ext}$ $[kW/l]$	$P_{out,max}/Vol_{airgap}$ $[kW/l]$
84.7	225.2	26.6	70.8

Table 2.13: Torque and power densities of the Prius 2010.

And for the loss densities:

$P_{loss,total}/Vol_{ext}$ $[kW/l]$	$P_{loss,total}/Vol_{airgap}$ $[kW/l]$
4.2	11.3

Table 2.14: Loss densities of the Prius 2010.

After the base point simulation, there has been the torque and power behaviour simulation through the motor mapping. Hence the map, torque and power graphs are reported below.

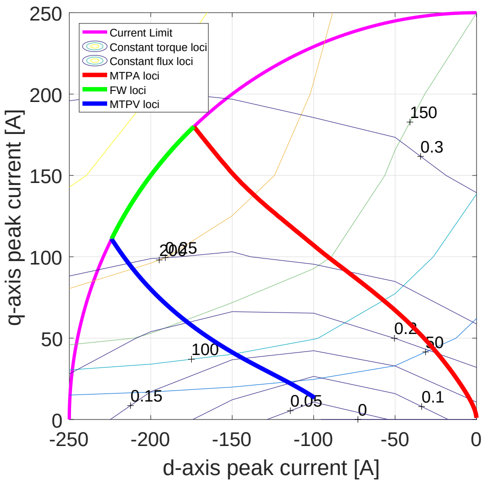

Figure 2.5: Prius 2010 (Pietrini): dq map

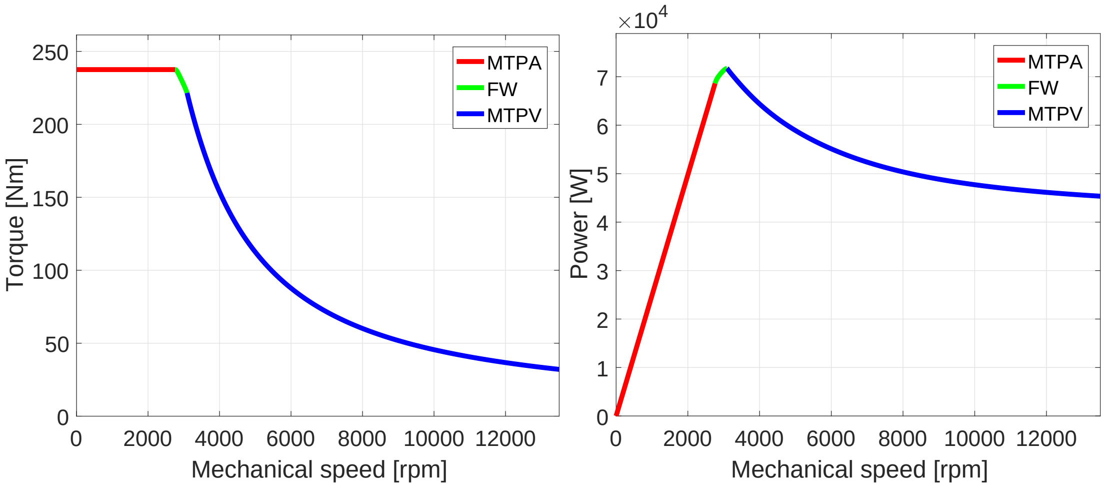

Figure 2.6: Prius 2010 (Pietrini): Torque and power vs speed.

2.3.1 Observation on Prius 2010 models

The previous graphs show that the power and torque are higher than the declared ones from producer data [18]. In particular for the Prius 2010 (Flux) model 2.2 the performances are a lot higher than the model described in this section 2.3.
As previously mentioned the simulated performances of 2.2 are different from the real one because of the great approximation in the rotor geometry, in the outer diameter and in the materials. Hence these main causes are reported in the table below in order to facilitate the comparison with the same but better refined motor of this section.

External Diameter	Different slot	Different iron	iron link absence
Internal Diameter	PMs dimensions	PMs material	n_{cs}

Table 2.15: Possible causes of error in the motor simulation

In particular in 2.3 there are marked differences in the width of the magnetic material, which in this model is more than 2 millimetres wider than the real reported one [19]. This larger part of magnet covers the iron link needed to guarantee the rotor mechanical strength. In this way there is also the absence of magnetic flux leakage due to these iron links. This leakage is very consistent in the case of large iron links as here, and this produces an overestimation of the torque which can be higher than 20% of the real one. These geometrical approximations together with the unknown motor controlling system causes the performances over-estimation.

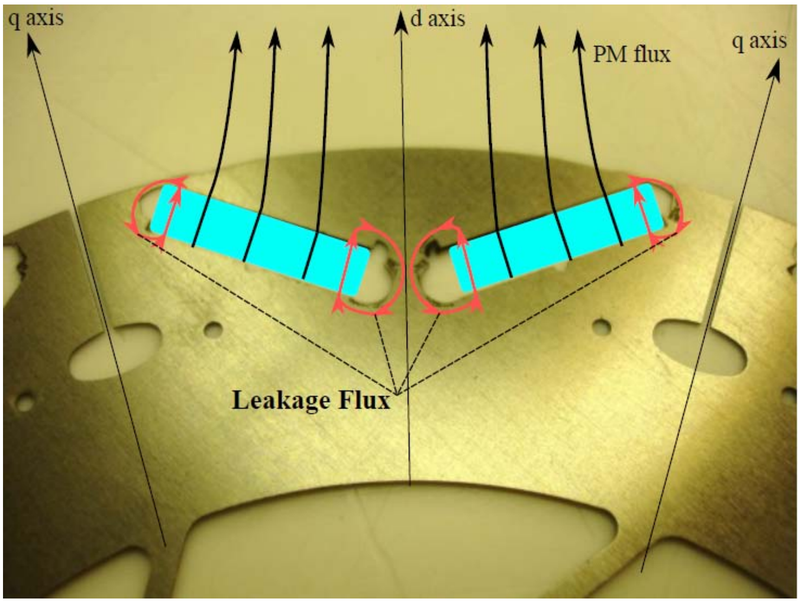

Figure 2.7: Magnetic fluxes in an IPM. In light blue there are the magnets. The red curve is flux leakage due to the iron link presence.

2.4 Toyota Prius 2004

This section is again on a Prius motor although this model is older than the other one. This geometry comes from Flux Motor hence it is a simplified one, in particular regarding the air barriers near the magnets. [23] The main difference from the previous Prius 2010 model is in the iron pack length.

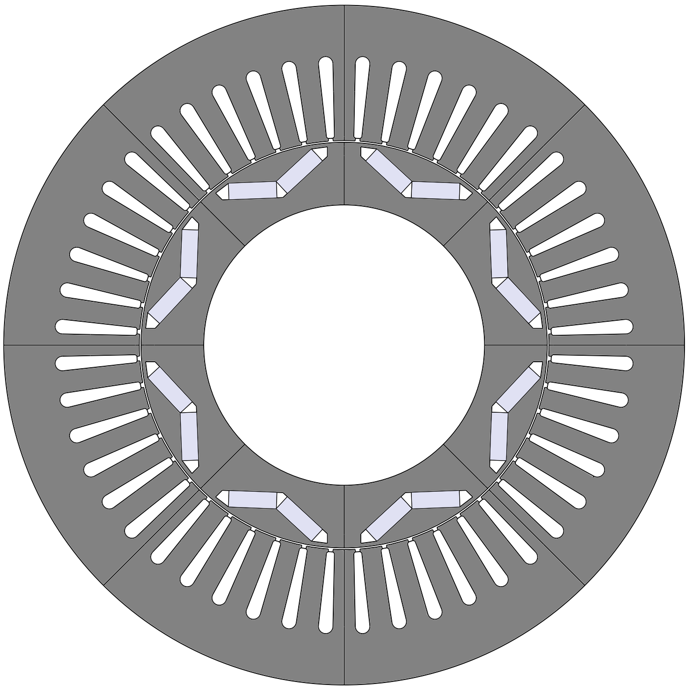

Figure 2.8: Geometry of the Prius 2004 from Flux.

The main geometry has been compared with other data from [23] in such a way to validate the model. The other main difference lies in the electrical parameters: in fact the bus DC voltage is now reduced to 500 [V] and the conductor's current is 200 [A]. These different parameters cause a difference in the torque and power behaviour. The main geometrical data are reported below:

L_{stk} mm	D_{ext} mm	D_i mm	g mm	D_r mm	$D_{r,i}$ mm	PM -	Vol_{ext} l
84	269	161.9	0.73	160.44	51	2 V-shaped	4.77
h_{slot} mm	$w_{slot,i}$ mm	w_t mm	h_{BI} mm	w_{so} mm	τ_p mm	w_{PM} mm	h_{PM} mm
32.48	3.19	8.34	20.4	1.88	63.58	18.9	6.5

Table 2.16: Prius 2004 (Flux) geometrical data.

What is important to notice in table 2.16, is the different length that lead to an higher volume of the machine. Electrical and nominal data are reported in the following table.

This table clearly show the different output of this motor. As a consequence of the

Q_s	p	T_{max}	P_{max}	V_{DC}	I_c	n_B	n_{max}
-	-	$[Nm]$	$[kW]$	$[V]$	$[A]$	$[rpm]$	$[rpm]$
48	4	400	50	500	200	1200	6000

Table 2.17: Nominal data of the model Prius 2004

lower DC bus voltage, together with the longer machine, this motor is characterised by a lower base speeds compared with the previous machine. On the contrary the lower current would produce a lower torque but due to the longer stack there is an output torque higher than the previous model.

One last detail that can be found in the producer's data-sheets is that the peak power of 50 [kW] is available in the speed range of 1200 e 1540 [rpm]. From the geometrical data table it can be calculated:

$$Vol_{ext} = \frac{\pi D_{ext}^2 \cdot L_{FE}}{4} = \frac{\pi 0.269^2 \cdot 0.084}{4} = 4.77[l] \tag{2.22}$$

$$Vol_{airgap} = \frac{\pi D_{int}^2 \cdot L_{FE}}{4} = \frac{\pi 0.1619^2 \cdot 0.084}{4} = 1.73[l] \tag{2.23}$$

From the technical data [19] it is obtained: $n_c = 9$ and $n_{pp} = 1$ hence:

$$n_{cs} = 9 \tag{2.24}$$

$$N_s = \frac{n_{cs} \cdot Qs}{m} = \frac{9 \cdot 48}{3} = 144 \tag{2.25}$$

From a simulation with $n_{cs} = 1$ it is obtained a slot current of 2200 [A] in order to produce an output torque of 400 [Nm]. Hence it is chosen a maximum in the conductor of 250 [A] in such a way in the slot there is a maximum current of $250 \cdot 9 = 2250$ [A].

$$\hat{K}_{s,max} = \frac{3 \cdot 0.9659 \cdot 144 \cdot 250}{\pi 0.1619} = 205097[A/m] \tag{2.26}$$

In the hypothesis that the nominal values are about 60 % of the maximum ones then there are: $I_n = 150$ [A] that produces a nominal torque of 240 [Nm] (these values are just hypothesized). Hence:

$$\hat{K}_{s,nom} = \frac{3 \cdot 0.9659 \cdot 144 \cdot 150}{\pi 0.1619} \cong 123060[A/m] \tag{2.27}$$

Assuming a $K_{fill} \cong 0.47$ like in the previous model :

$$J_s = \frac{2250}{\sqrt{2} \cdot 145.159 \cdot 0.47} = 24.36[A/mm^2] \tag{2.28}$$

From the base point simulation on a single conductor there are almost 25.3 [V] and if this voltage is multiplied by the number of conductor in the slot the following result is obtained: $25.3 \cdot 9 \cong 230$ [V] and then $230 \cdot \sqrt{3} \cong 400$ [V] and this is different from the nominal 500 [V] of the DC bus. This can be justified by the fact that voltage calculation in the base point is done by neglecting the conductor's resistive voltage drop. Other data from the base speed simulation are reported in the table below:

PF -	η -	P_{in} $[kW]$	P_{out} $[kW]$	$P_{loss,total}$ $[kW]$
0.75	0.845	59.8	50.5	9.28
$P_{J,s}$ $[W]$	$P_{fe,tooth}$ $[W]$	$P_{fe,BI}$ $[W]$	$P_{fe,total}$ $[W]$	P_{mech} $[W]$
8641.2	190.7	188.8	380	262.4

Table 2.18: Data acquisition in the base point simulation.

From these data the following ratios are evaluated:

T_{max}/Vol_{ext} $[Nm/l]$	T_{max}/Vol_{airgap} $[Nm/l]$	$P_{out,max}/Vol_{ext}$ $[kW/l]$	$P_{out,max}/Vol_{airgap}$ $[kW/l]$
85.3	235.3	12.8	35.3

Table 2.19: Torque and power densities of the Prius 2004.

$P_{loss,total}/Vol_{ext}$ $[kW/l]$	$P_{loss,total}/Vol_{airgap}$ $[kW/l]$
1.95	5.4

Table 2.20: Loss densities of the Prius 2004.

From these values it can now be carried out the motor dq mapping. The graphs obtained by this simulation are reported in the following page.
These graphs illustrate that the 50 [kW] power is available in a region larger than the reported one [23]. Hence this is an optimistic estimation of the torque and power behaviour. The difference with respect the real one can be grouped in:

- PMs dimensions
- PMs material
- absence of iron links
- approximation of the air barriers
- different iron characteristics

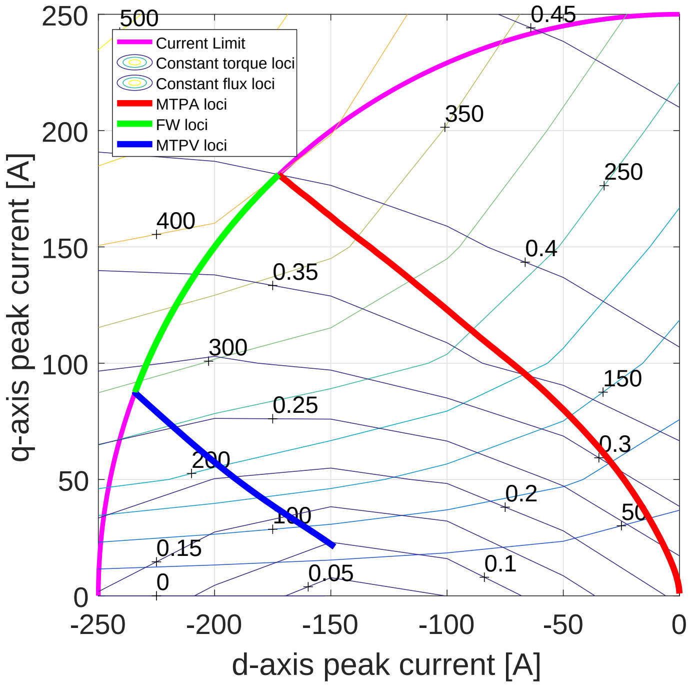

Figure 2.9: Prius 2004 model: dq map.

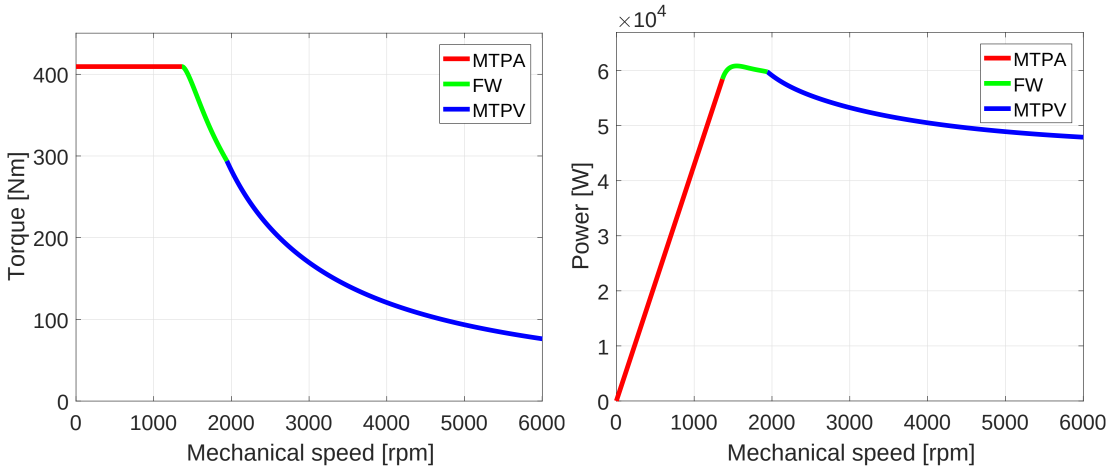

Figure 2.10: Prius 2004 model: Torque and power vs speed.

2.5 Toyota Camry

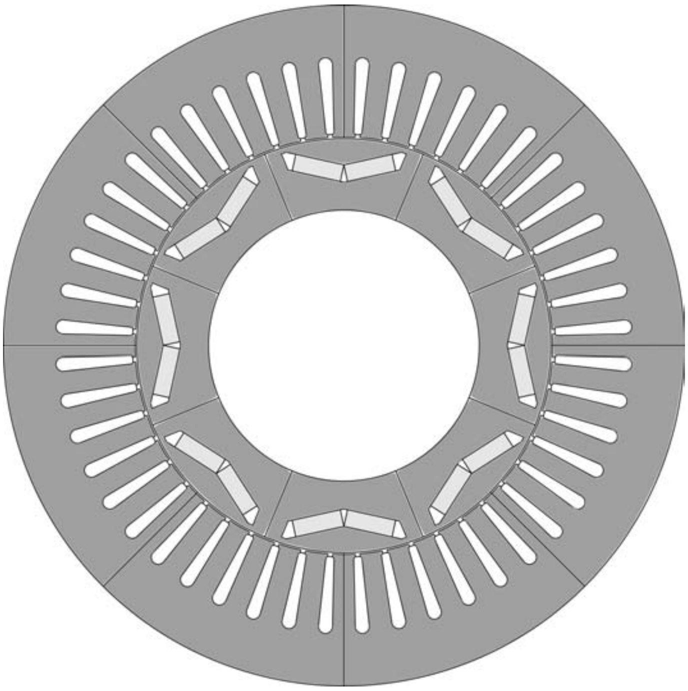

Figure 2.11: Geometry of the Camry from Flux.

In this case, only the motor's main geometry was available and the other data have been searched in producer's documents. In these data-sheets [19] there were the following values:

- $P_{out} = 105$ [kW] @ 4500 [rpm]
- $T_{out} = 270$ [Nm] 0 - 1500 [rpm]

This data do not provide information about the base speed of the motor, but through simple calculations one can obtain at 1500 [rpm]:

$$\omega_m = 1500 \cdot \frac{2\pi}{60} = 157.08[rad/s] \tag{2.29}$$

And in order to gain the shaft power:

$$P_{out,base} = \omega_m \cdot T_{out} = 157.08 \cdot 270 \cong 42.4[kW] \tag{2.30}$$

As it can be noticed by this value the base point power is much lower than the maximum power @ 4500 [rpm]. There are several explanations to this, one of which is that the motor is designed to develop less power than the 105 [kW], for example it has a continuous power of 50 [kW], and the value of 105 [kW] is just a transient value that can be reached by moving the base point at higher speeds.
This means that the base point is translated toward higher speeds when the maximum power is required. This is done by the electronic controller unit in order to optimize the efficiency during the car use. A second base speed for the maximum power operations will be assumed in order to have a complete overview of the motor behaviour.

Another simple explanation is that the motor can produce 270 [Nm] also above the 1500 [rpm] but it is cut-off in order to avoid overheating.
From [19] the following geometrical parameters are obtained and reported in the table:

L_{stk}	D_{ext}	D_i	g	D_r	$D_{r,i}$	PM	Vol_{ext}
mm	mm	mm	mm	mm	mm	-	l
60.7	264	161.9	0.7	160.5	105	2 V-shaped	3.32
h_{slot}	$w_{slot,i}$	w_t	h_{BI}	w_{so}	τ_p	w_{PM}	h_{PM}
mm	mm	mm	mm	mm	mm	mm	mm
29.9	3.2	8.34	20.4	1.88	63.58	19.1	6.6

Table 2.21: Geometrical data of the model Camry 2014 (Flux).

$$Vol_{ext} = \frac{\pi D_{ext}^2 \cdot L_{stk}}{4} = \frac{\pi \cdot 0.264^2 \cdot 0.0607}{4} = 3.32[l] \tag{2.31}$$

$$Vol_{airgap} = \frac{\pi D_{int}^2 \cdot L_{stk}}{4} = \frac{\pi \cdot 0.1619^2 \cdot 0.0607}{4} = 1.25[l] \tag{2.32}$$

From the technical data [19] it is obtained: $n_c = 14$ and $n_{pp} = 2$ hence:

$$n_{cs} = 7 \tag{2.33}$$

$$N_s = \frac{n_{cs} \cdot Qs}{m} = \frac{7 \cdot 48}{3} = 112 \tag{2.34}$$

From the base point simulation with $n_{cs} = 1$ it has been obtained a slot current equal to 2160 [A] in order to produce the maximum output torque of 270 [Nm]. Hence it is chosen a maximum conductor current of 300 [A] so that the slot has a maximum current of $300 \cdot 7 = 2100$ [A]. The obtained base point torques are: $T_{dq} = 267.2$ [Nm] and $T_{maxwell} = 273.3$ [Nm]. From these currents it can be found:

$$\hat{K}_{s,max} = \frac{3 \cdot 0.9659 \cdot 112 \cdot 300}{\pi 0.1619} = 191424[A/m] \tag{2.35}$$

Other motor data are reported below:

Q_s	p	T_{max}	P_{max}	V_{DC}	I_c	n_B	n_{max}
-	-	$[Nm]$	$[kW]$	$[V]$	$[A]$	$[rpm]$	$[rpm]$
48	4	270	105	650	300	1500	5000

Table 2.22: Producer declared data of the model Camry 2014.

From the DC bus voltage it is obtained the peak value of phase voltage as:

$$\hat{V}_{phase} = \frac{650}{\overline{3}} = 375[V] \tag{2.36}$$

Again, a 10 % can be subtracted in order to consider the losses in the power supply system so that it becomes a phase voltage of about 340 [V].

Here are now reported the base point values at the rated speed of 1500[rpm].

PF -	η -	P_{in} $[kW]$	P_{out} $[kW]$	$P_{loss,total}$ $[kW]$
0.73	84.17	49.9	41.9	7.9
$P_{J,s}$ $[W]$	$P_{fe,tooth}$ $[W]$	$P_{fe,BI}$ $[W]$	$P_{fe,total}$ $[W]$	P_{mech} $[W]$
7283	186.5	183	369.5	244

Table 2.23: Data acquisition in the base point @ 1500 [rpm].

The second base point that allows to obtain the maximum power of the motor is reached when the winding voltage reaches 340 [V]. This secondary base point is identified at about 3600 [rpm]. In this condition the following data are obtained:

PF -	η -	P_{in} $[kW]$	P_{out} $[kW]$	$P_{loss,total}$ $[kW]$
0.703	91.3	110.4	100.7	9.7
$P_{J,s}$ $[W]$	$P_{fe,tooth}$ $[W]$	$P_{fe,BI}$ $[W]$	$P_{fe,total}$ $[W]$	P_{mech} $[W]$
7283	737	723	1460	907

Table 2.24: Data acquisition in the base point @ 3600 [rpm]

From the maximum values are deduced the following ratios:

T_{max}/Vol_{ext} $[Nm/l]$	T_{max}/Vol_{airgap} $[Nm/l]$	$P_{out,max}/Vol_{ext}$ $[kW/l]$	$P_{out,max}/Vol_{airgap}$ $[kW/l]$
80.5	213.8	33.4	88.9

Table 2.25: Torque and power densities of the Camry 2014 model.

The current density can be estimated by using the maximum current value in the slot equal to 2100 [A] and assuming a $K_{fill} \cong 0.5$:

$$\hat{J}_s = \frac{2100}{\overline{2} \cdot 128.64 \cdot 0.5} \cong 23.1[A/mm^2] \tag{2.37}$$

$P_{loss,total}/Vol_{ext}$ $[kW/l]$	$P_{loss,total}/Vol_{airgap}$ $[kW/l]$
2.92	7.76

Table 2.26: Loss densities of the Camry 2014 model.

In this page the graphs of the motor mapping at its maximum power are reported .

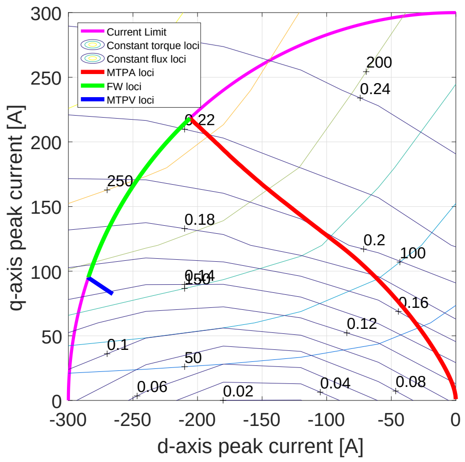

Figure 2.12: Toyota Camry model: dq map.

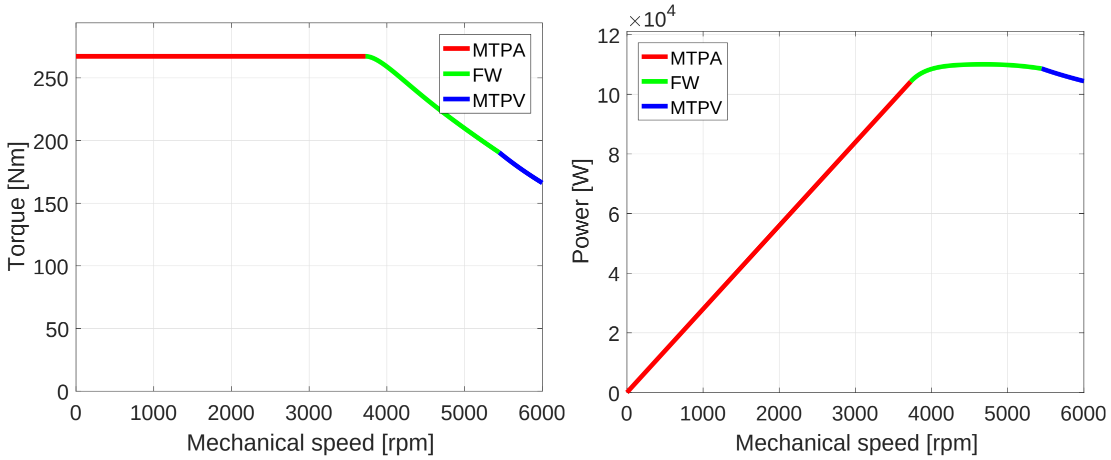

Figure 2.13: Toyota Camry model: Torque and power vs speed.

2.6 Lexus Ls 600h

This model geometry comes from the previous work in [20] and the geometrical data were found in its report. These data are more detailed with-respect the other models that come from Flux motor.

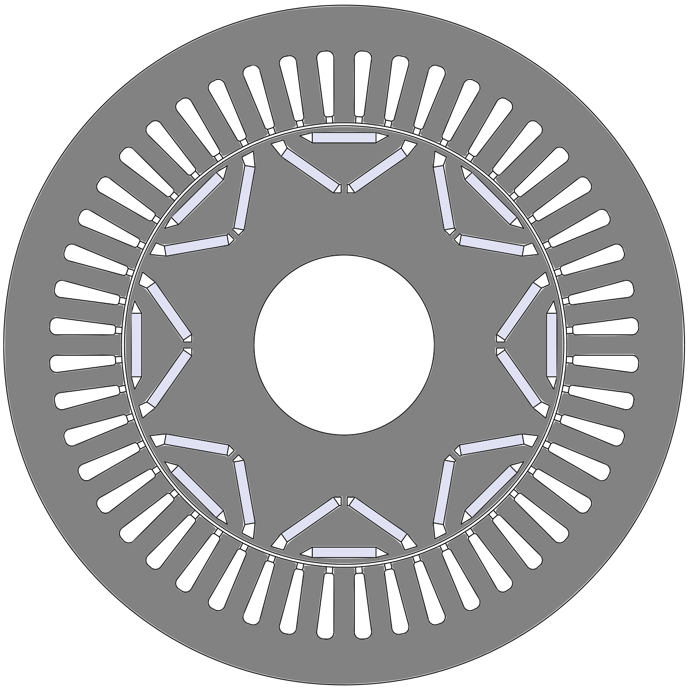

Figure 2.14: Geometry of Lexus LS 600h from Pietrini's document

L_{stk} mm	D_{ext} mm	D_i mm	g mm	D_r mm	$D_{r,i}$ mm	PM -	Vol_{ext} l
135.4	200	130.86	0.89	129.08	53	3 Δ-Shaped	4.25
h_{slot} mm	$w_{slot,i}$ mm	w_t mm	h_{BI} mm	w_{so} mm	τ_p mm	w_{PM} mm	h_{PM} mm
19.25	2.88	6	13.32	1.88	51.388	18.7	3.05

Table 2.27: Geometrical data of the model Lexus LS 600h form [20].

The other nominal values are obtained by the report and confirmed by [8] and [19] reports. These values are reported below:

Another important aspect is the number of conductors in the slot which in this model is: $n_c = 7$ and associated with $n_{pp} = 2$ is needed in order to evaluate:

$$n_{cs} = 7/2 = 3.5 \tag{2.38}$$

The volumes are here evaluated:

$$Vol_{ext} = \frac{\pi D_{ext}^2 \cdot L_{fe}}{4} = \frac{\pi \cdot 0.2^2 \cdot 0.1354}{4} = 4.25[l] \tag{2.39}$$

Q_s	p	T_{max}	P_{max}	V_{DC}	I_c	n_B	n_{max}
-	-	$[Nm]$	$[kW]$	$[V]$	$[A]$	$[rpm]$	$[rpm]$
48	4	300	165	650	400	5000	10230

Table 2.28: Nominal data of the model Lexus Ls600h

$$Vol_{airgap} = \frac{\pi D_{int}^2 \cdot L_{fe}}{4} = \frac{\pi \cdot 0.13086^2 \cdot 0.1354}{4} = 1.82[l] \tag{2.40}$$

This geometry is characterized by different geometrical aspects, in particular is longer and with a smaller diameter than the previously seen geometries. Then there is the PMs quantity and disposition in the rotor which is different. Starting from the DC bus voltage the peak phase voltage is obtained:

$$\hat{V}_{phase} = \frac{650}{\sqrt{3}} = 375[V] \tag{2.41}$$

A 10 % is taken out in order to consider the power supply system losses. This leads to a phase voltage of about 340 [V].

$$N_s = \frac{n_{cs} Qs}{m} = \frac{3.5 * 48}{3} = 56 \tag{2.42}$$

In the hypothesis of a produced torque of 300 [Nm] and with an air-gap flux density of 1 [T] the electrical loading is estimated:

$$\hat{K}_{s,max} = \frac{T}{\frac{\pi}{4} \cdot D^2 \cdot \hat{B}_g \cdot L_{stk}} = \frac{300}{1.821 \cdot 10^{-3}} = 164744.7[A/m] \tag{2.43}$$

The electrical loading allows to evaluate the current needed to produce the output torque previously defined. Hence the conductor current is approximated as:

$$\hat{I}_{c,max} = \frac{\hat{K}_{s,max} \cdot \pi \cdot D}{m \cdot K_w \cdot N_s} = \frac{164744.7 \cdot \pi \cdot 0.13086}{3 \cdot 0.9659 \cdot 56} \cong 415[A] \tag{2.44}$$

This approximation allows to use 400 [A] as first current value in the simulations. This value is then multiplied by the number of equivalent series conductor:

- $\hat{I}_{slot,max} = 400 \cdot 3.5 = 1400$ [A]
- $\hat{V}_{slot,max} = 350/3.5 = 100$ [V]

From these values the base point simulation output are:

- $T_{dq} = 298.15$ [Nm]
- $T_{mxw} = 286.97$ [Nm]
- $n_B \cong 5000$ [rpm]

These obtained values are consistent with what is said in report [20] that indicate as conductor current 400 [A] and as Maxwell torque: $T_{Maxwell} = 283.8$ [Nm]. Looking at the difference of the obtained torques from the [20] one, the following ratios can be evaluated:

$$T_{dq}/T_{mxq,Pietrini} = 298.15/283.8 = 1.05 \tag{2.45}$$

$$T_{mxw}/T_{mxq,Pietrini} = 286.97/283.8 = 1.01 \tag{2.46}$$

This means that there is just 5% of maximum deviation from the reference values found in the report [20]. From the obtained maximum torque and power values the following ratios are evaluated:

T_{max}/Vol_{ext} $[Nm/l]$	T_{max}/Vol_{airgap} $[Nm/l]$	$P_{out,max}/Vol_{ext}$ $[kW/l]$	$P_{out,max}/Vol_{airgap}$ $[kW/l]$
70.2	163.8	39.5	92.3

Table 2.29: Torque and power densities of the Lexus model.

The base point is reached when the winding voltage equalize 340 [V]. This base point is identified at the base speed of about 5000 [rpm] and in this condition it is obtained:

PF -	η -	P_{in} $[kW]$	P_{out} $[kW]$	$P_{loss,total}$ $[kW]$
0.77	92.7	168.5	156.1	12.4
$P_{J,s}$ $[W]$	$P_{fe,tooth}$ $[W]$	$P_{fe,BI}$ $[W]$	$P_{fe,total}$ $[W]$	P_{mech} $[W]$
7800	1429	1477	2906	1656

Table 2.30: Data acquisition in the base point @ 5000 [rpm].

Hence the losses densities are evaluated:

$P_{loss,total}/Vol_{ext}$ $[kW/l]$	$P_{loss,total}/Vol_{airgap}$ $[kW/l]$
2.9	6.8

Table 2.31: Losses densities of the Lexus model.

By using the correct values of conductor′s current the electrical loading is obtained:

$$\hat{K}_{s,max} = \frac{3 \cdot 0.9659 \cdot 56 \cdot 400}{\pi \cdot 0.13086} = 157900[A/m] \tag{2.47}$$

Therefore a nominal current of 250 [A] is assumed in order to approximate the rated electrical loading:

$$\hat{K}_{s,nom} = \frac{3 \cdot 0.9659 \cdot 56 \cdot 250}{\pi \cdot 0.13086} \cong 99000[A/m] \tag{2.48}$$

From the assumption of a $K_{fill} = 0.47$ the current density is estimated as follows:

$$\hat{J}_s = \frac{1400}{\overline{2} \cdot 76.784 \cdot 0.47} \cong 27.4[A/mm^2] \tag{2.49}$$

The motor dq mapping and the power and torque vs speed graphs are reported below:

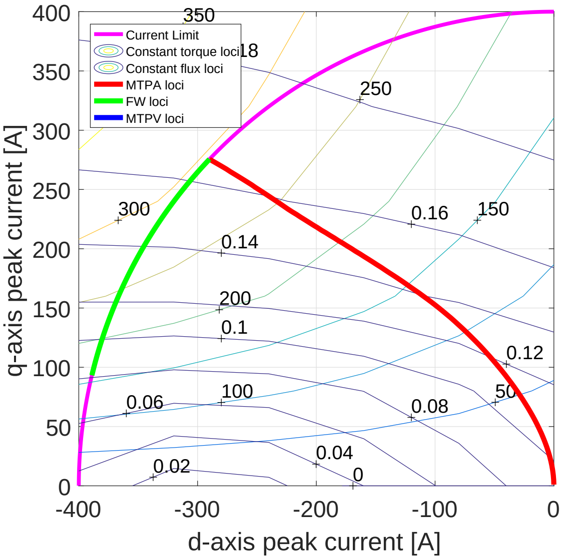

Figure 2.15: Lexus Ls 600h: dq map.

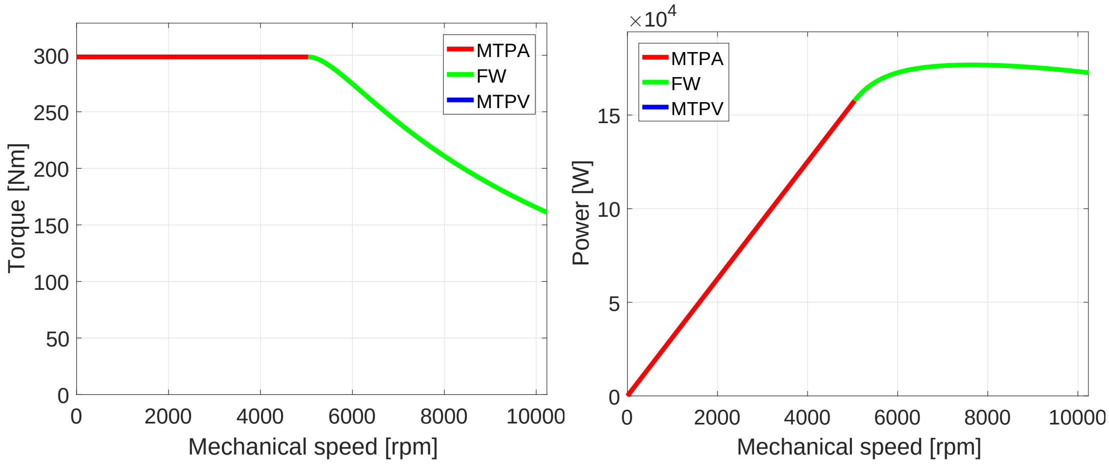

Figure 2.16: Lexus Ls 600h: torque and power vs speed.

2.7 Honda Accord M

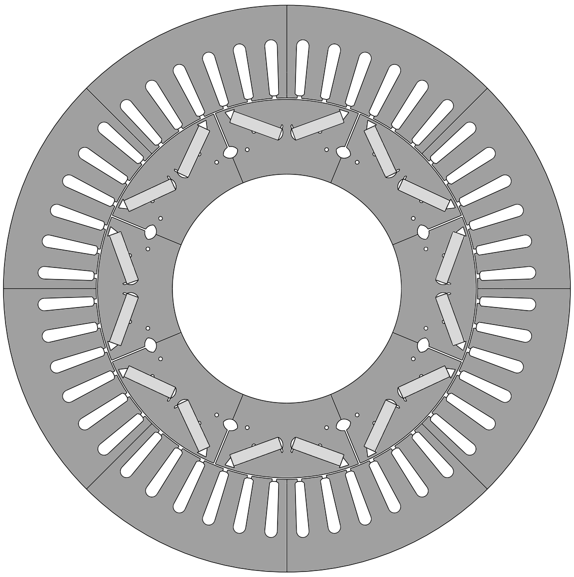

Figure 2.17: Geometry of the Accord model

The M in the name means Motor, and it is needed in order to distinguish it from the generator mounted on the same car. The motor and the generator are characterized by the same geometry (both with V-shaped permanent magnet rotor) but the motor is longer than the generator (61.7 [mm] vs 37.6) [19]. Here it is presented the machine that works as motor (M).

Due to the absence of precise dimension the air barriers have been approximated. The geometrical data are reported in the next table:

L_{stk} mm	D_{ext} mm	D_i mm	g mm	D_r mm	$D_{r,i}$ mm	PM -	Vol_{ext} l
61.7	291.34	196.6	0.8	195	118	2 V-shaped	4.11
h_{slot} mm	$w_{slot,i}$ mm	w_t mm	h_{BI} mm	w_{so} mm	τ_p mm	w_{PM} mm	h_{PM} mm
28.98	4.8	8.34	17.8	2.34	77.2	25.5	6.28

Table 2.32: Geometrical data of the motor installed in the Accord model.

This model has been tested also in other documents of the ORNL [9] hence the obtained values will be compared with theirs.

Q_s -	p -	T_{max} $[Nm]$	P_{max} $[kW]$	V_{DC} $[V]$	I_c $[A]$	n_B $[rpm]$	n_{max} $[rpm]$
48	4	300	124	700 (max)	350	4000	12000

Table 2.33: Declared data of the Honda Accord 2014 electric motor.

$$Vol_{ext} = \frac{\pi D_{ext}^2 \cdot L_{fe}}{4} = \frac{\pi \cdot 0.29134^2 \cdot 0.0617}{4} = 4.11[l] \tag{2.50}$$

$$Vol_{traferro} = \frac{\pi D_{int}^2 \cdot L_{fe}}{4} = \frac{\pi \cdot 0.1966^2 \cdot 0.0617}{4} = 1.87[l] \tag{2.51}$$

$$\hat{V}_{phase} = \frac{700}{\sqrt{3}} \cong 400[V] \tag{2.52}$$

From this voltage it can be subtracted a 10 % in order to take in account the power losses in the supply system so that the maximum phase voltage will be equal to 360 [V]. It has to be noticed that the number of conductors in the slot is not known for this model. This means that the simulation of the motor is carried out with a unitary number of conductor, and this leads to:

$$n_{cs} = 1 \tag{2.53}$$

$$N_s = \frac{n_{cs} Qs}{m} = \frac{1 \cdot 48}{3} = 16 \tag{2.54}$$

In the hypothesis of producing 300 [Nm] and with an approximated flux density of 1 [T] at the air-gap an estimation of the electric loading can be obtained as:

$$\hat{K}_{s,max} = \frac{T}{\frac{\pi}{4} \cdot \hat{B}_g \cdot D^2 \cdot L_{fe}} = \frac{300}{1.87 \cdot 10^{-3}} = 160170[A/m] \tag{2.55}$$

And from this last value an estimated slot current is obtained as:

$$\hat{I}_{slot,max} = \frac{\hat{K}_{s,max} \cdot \pi \cdot D}{m \cdot K_w \cdot N_s} = \frac{160170 \cdot \pi \cdot 0.1966}{3 \cdot 0.9659 \cdot 16} = 2133[A] \tag{2.56}$$

As first slot current it can be used 2100 [A], and from this value in the presumed base point the following values are obtained :

- $T_{dq} = 305.95$ [Nm]
- $T_{mxw} = 287.72$ [Nm]
- $n_B = 4000$ [rpm]

By using $n_{cs} = 1$ the voltage obtained on the single conductor is equal to 57 [V]. The real number of conductor in the slot can be estimated as:

$$n_{cs} = \frac{340 \div 400}{57} \cong 6 \div 7 \tag{2.57}$$

For example $n_{cs} = 6$ is taken while also assuming $n_{pp} = 1$ the number of series conductor in a phase is get:

$$N_s = \frac{n_{cs} Qs}{m} = \frac{6 \cdot 48}{3} = 96 \tag{2.58}$$

From the slot current and the supposed number of conductors the peak value of the conductor′s current is obtained as $2100/6 = 350$ [A]. The estimated electrical data are reported in the table below:

Other useful data from the simulation in the base point are:

Model -	$\hat{I}_{slot,max}$ $[A]$	$\hat{V}_{slot,max}$ $[V]$	$\hat{I}_{c,max}$ $[A]$	$\hat{V}_{phase,max}$ $[V]$	n_c estimated -
Accord	2100	$\cong 60$	350	360	6

Table 2.34: Approximated electrical parameters.

PF -	η -	P_{in} $[kW]$	P_{out} $[kW]$	$P_{loss,total}$ $[kW]$
0.74	92.6	138.4	128.2	10.2
$P_{J,s}$ $[W]$	$P_{fe,tooth}$ $[W]$	$P_{fe,BI}$ $[W]$	$P_{fe,total}$ $[W]$	P_{mech} $[W]$
7077.1	845.3	1050.9	1896.3	1215.8

Table 2.35: Data acquisition in the base point @ 4000 [rpm].

From the table it can be observed that the output power reached in the base point is slightly higher than the rated maximum power of 124 [kW]. This can be justified by taking into account the considerations of the PMs dimension, unknown, the material used both for the iron and the PMs that may have different properties from the real ones, and the unknown dimensions of the air barriers. From the obtained values we can evaluate the following density ratios:

T_{max}/Vol_{ext} $[Nm/l]$	T_{max}/Vol_{airgap} $[Nm/l]$	$P_{out,max}/Vol_{ext}$ $[kW/l]$	$P_{out,max}/Vol_{airgap}$ $[kW/l]$
74.5	163.6	33.6	73.8

Table 2.36: Torque and power densities of the Accord model.

The power loss density are:

From the estimated N_s and the peak conductor current value we gain the electric load:

$$\hat{K}_{s,max} = \frac{3 \cdot 0.9659 \cdot 96 \cdot 350}{\pi \cdot 0.1966} = 157720[A/m] \tag{2.59}$$

$$\hat{K}_{s,nom} = \frac{3 \cdot 0.9659 \cdot 96 \cdot 200}{\pi \cdot 0.1966} = 90124[A/m] \tag{2.60}$$

Lastly an estimation of the current density can be obtained through the assumption of $K_{fill} = 0.45$:

$$\hat{J}_s = \frac{2100}{\overline{2} \cdot 160.37 \cdot 0.45} \cong 20.6[A/mm^2] \tag{2.61}$$

$P_{loss,total}/Vol_{ext}$ $[kW/l]$	$P_{loss,total}/Vol_{airgap}$ $[kW/l]$
2.5	5.44

Table 2.37: Loss densities of the Accord model.

The motor mapping is here reported:

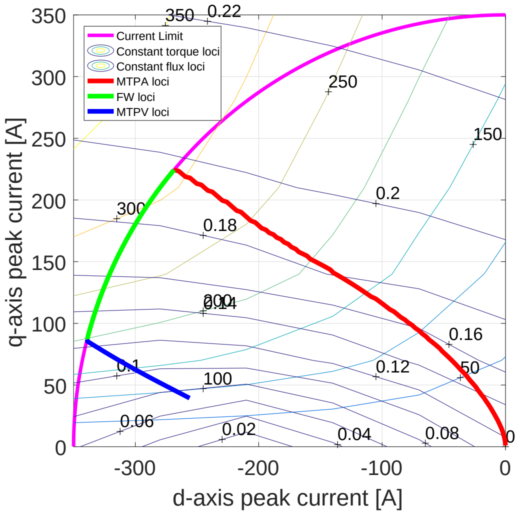

Figure 2.18: Accord Motor model: dq map.

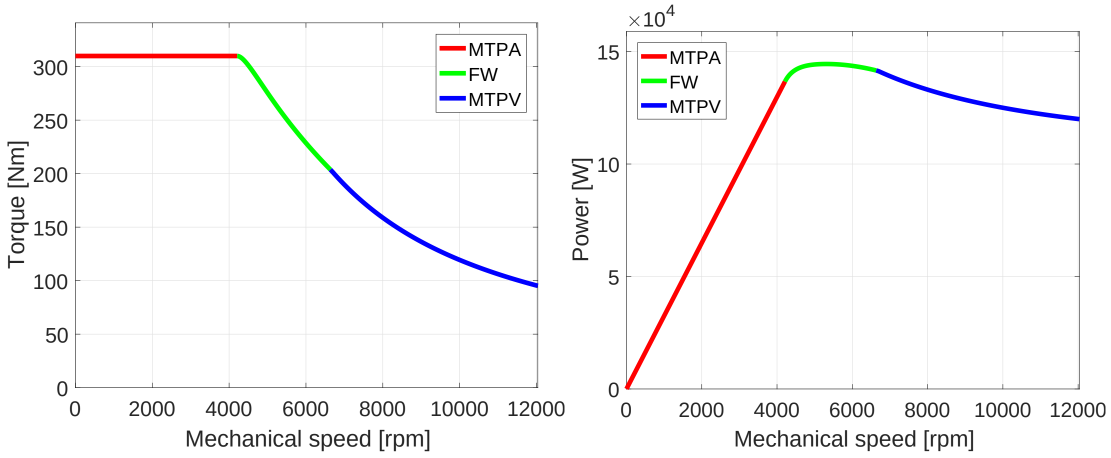

Figure 2.19: Accord Motor model: Torque, Power vs speed

2.8 Nissan LEAF

Nissan Leaf motor has been reproduced following the drawings and the main data in the ORNL documents [19], [9] and in the thesis [29].

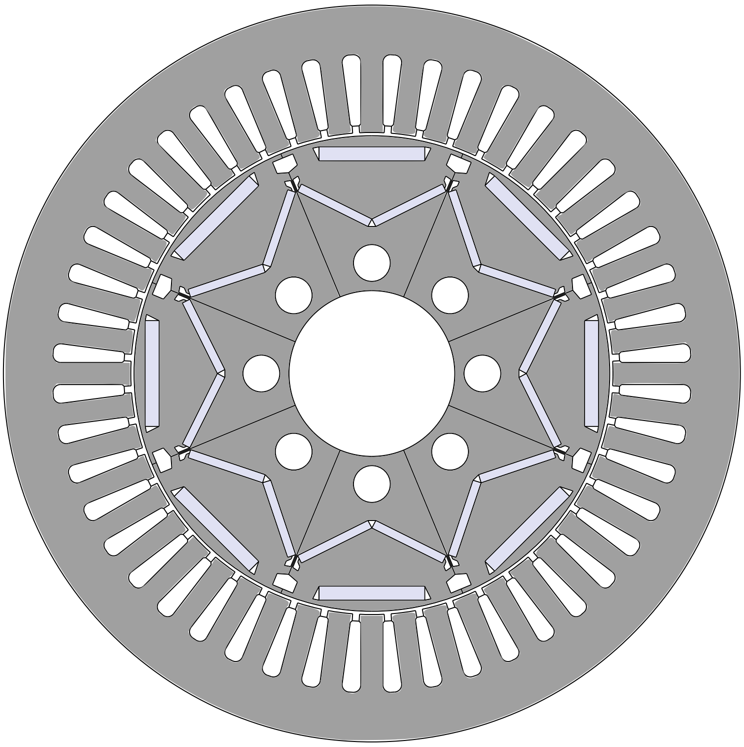

Figure 2.20: Geometry of the Leaf model

The geometrical data are below reported:

L_{stk} mm	D_{ext} mm	D_i mm	g mm	D_r mm	$D_{r,i}$ mm	PM -	Vol_{ext} l
151	200	131	0.89	129.08	45	3 Δ-shaped	4.74
h_{slot} mm	$w_{slot,i}$ mm	w_t mm	h_{BI} mm	w_{so} mm	τ_p mm	w_{PM} mm	h_{PM} mm
19.25	2.88	6	14	1.88	51.42	28.7 & 21.35	3.79 & 2.32

Table 2.38: Geometrical data of the Nissan Leaf model.

The volumes of the machine are obtained for these data:

$$Vol_{ext} = \frac{\pi D_{ext}^2 \cdot L_{FE}}{4} = \frac{\pi \cdot 0.2^2 \cdot 0.151}{4} = 4.74[l] \tag{2.62}$$

$$Vol_{airgap} = \frac{\pi D_{int}^2 \cdot L_{FE}}{4} = \frac{\pi \cdot 0.131^2 \cdot 0.151}{4} = 2.04[l] \tag{2.63}$$

The other performance data comes from the producer's documents and they are reported in the following table:

Q_s -	p -	T_{max} $[Nm]$	P_{max} $[kW]$	V_{DC} $[V]$	I_c $[A]$	n_B $[rpm]$	n_{max} $[rpm]$
48	4	280	80	375	625	2100	10000

Table 2.39: Producer declared values of the Leaf motor.

In particular the maximum power has to be obtained at the speed of 3000 [rpm] whereas the torque of 280 [Nm] should be available until 2100 [rpm].
Observation: in this model the exact geometry is not given, hence for some dimensions the Lexus geometry and as been considered and scaled in such a way to have an approximation of the motor. The Lexus was chosen because it is the geometry whose main dimensions are the closes to the Leaf one.
From the DC bus voltage it is obtained the peak value of the phase voltage as:

$$\hat{V}_{phase} = \frac{375}{\sqrt{3}} = 216.5[V] \tag{2.64}$$

A subtraction of 10 % is effected from this value in order to take into account the power losses in the supply system, hence the maximum phase voltage will be equal to 200 [V].
From the number of slot conductors and the parallel paths it can be defined:

$$n_{cs} = n_c/n_{pp} = 8/4 = 2 \tag{2.65}$$

The series conductors per phase can be evaluated from this number:

$$N_s = \frac{n_{cs} \cdot Qs}{m} = \frac{2 \cdot 48}{3} = 32 \tag{2.66}$$

The electric loading estimation can be carried out by assuming a torque of 280 [Nm] and a flux density at the air-gap B_g equal to 1 [T]:

$$\hat{K}_{s,max} = \frac{T}{\frac{\pi}{4} \cdot \hat{B}_g \cdot D^2 \cdot L_{stk}} = \frac{280}{2.03521 \cdot 10^{-3}} \cong 137600[A/m] \tag{2.67}$$

Hence the slot current is estimated starting from that electrical loading:

$$\hat{I}_{slot,max} = \frac{\hat{K}_{s,max} \cdot \pi D}{m \cdot K_w \cdot N_s} = \frac{137600 \cdot \pi \cdot 0.131}{3 \cdot 0.9659 \cdot 32} \cong 610[A] \tag{2.68}$$

These evaluation allows to consider a first conductor current equal to 600 [A] for the FEM simulation. In the base point the following values are evaluated:

- $T_{dq} = 288.32$ [Nm]
- $T_{mxw} = 295.72$ [Nm]
- $n_B = 2100$ [rpm]

In the base speed simulation the voltage on a single conductor is about of 90 [V]. Indeed, if this value is multiplied by $n_{cs} = 2$, a winding total voltage of 180 is gained and is slightly lower than the previously evaluated 200 [V]. There are many reasons that produces this difference, the most important is that the geometry is approximated, and the PM material and dimension is not exactly the same of the real motor. This is the same for the lamination material. Other useful data obtained in the base point are here reported:

PF -	η -	P_{in} $[kW]$	P_{out} $[kW]$	$P_{loss,total}$ $[kW]$
0.86	88.5	71.7	63.4	8.3
$P_{J,s}$ $[W]$	$P_{fe,tooth}$ $[W]$	$P_{fe,BI}$ $[W]$	$P_{fe,total}$ $[W]$	P_{mech} $[W]$
7223.4	313.3	294.5	607.8	435.8

Table 2.40: Data acquisition in the base point @ 2100 [rpm].

These data allows to evaluate the following ratios:

T_{max}/Vol_{ext} $[Nm/l]$	T_{max}/Vol_{airgap} $[Nm/l]$	$P_{out,max}/Vol_{ext}$ $[kW/l]$	$P_{out,max}/Vol_{airgap}$ $[kW/l]$
60.8	141.2	16.9	39.2

Table 2.41: Torque and power densities of the Leaf model.

$P_{loss,total}/Vol_{ext}$ $[kW/l]$	$P_{loss,total}/Vol_{airgap}$ $[kW/l]$
1.7	4.1

Table 2.42: Loss densities of the Leaf model.

Taking into account the real conductor current the electrical loading previously predicted is here confirmed:

$$\hat{K}_{s,max} = \frac{3 \cdot 0.9659 \cdot 32 \cdot 600}{\pi \cdot 0.131} = 135190[A/m] \tag{2.69}$$

By assuming a nominal current equal to 60 % of the maximum one, i.e. of $0.6 \cdot 600 = 360$ [A] the rated electrical loading can be defined as:

$$\hat{K}_{s,nom} = \frac{3 \cdot 0.9659 \cdot 32 \cdot 360}{\pi \cdot 0.131} \cong 81100[A/m] \tag{2.70}$$

The current density approximation can be done by assuming a $K_{fill} = 0.45$:

$$\hat{J}_s = \frac{1200 \cdot \sqrt{2}}{76.76 \cdot 0.45} \cong 24.6[A/mm^2] \tag{2.71}$$

The 1200 [A] used in the current density formula is the peak value of the total slot current. In the following page there are the graphs of the mapping simulation which are compared with the producer declared specifications.

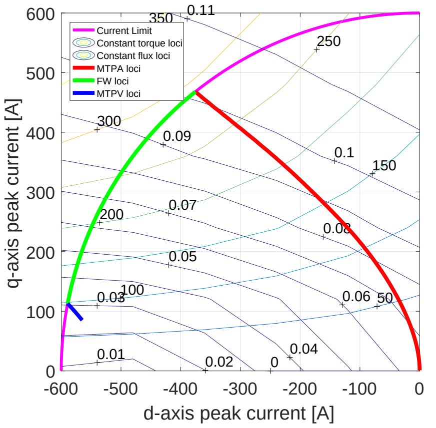

Figure 2.21: Nissan Leaf motor: dq map.

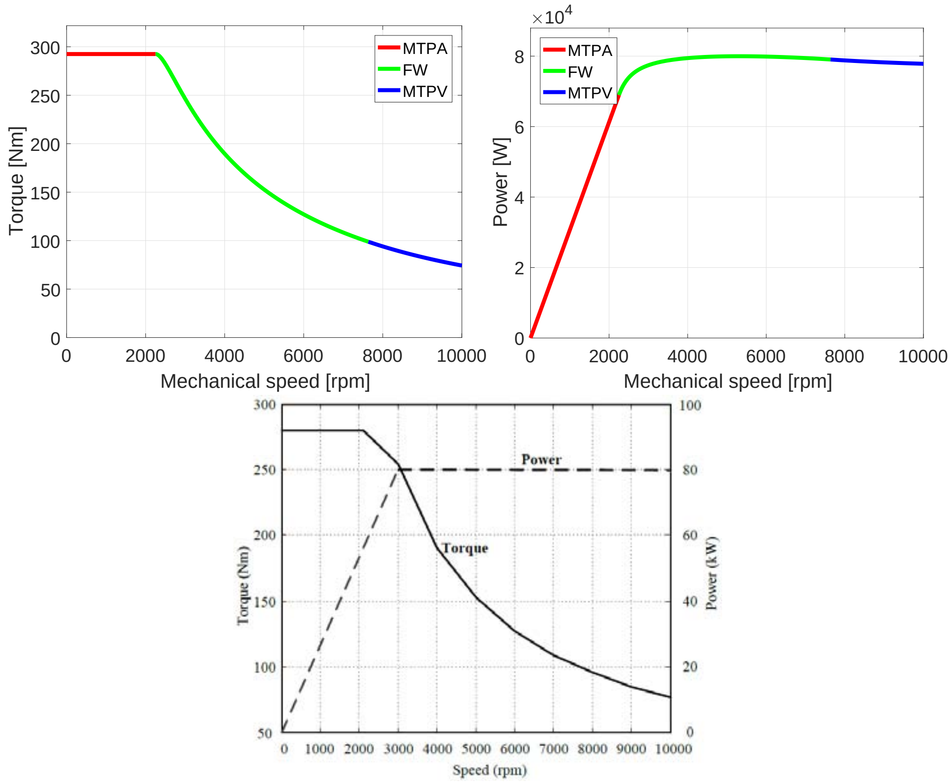

Figure 2.22: Leaf: torque and power behaviour (above) and declared performances (below).

It is important to notice that the simulated power and torque behaviour reported in figure 2.22 (above) are very similar to the declared specifications (below). This fact means that the geometry obtained from approximated data is similar to the real one despite the great presence of small air barriers of unknown dimensions in the rotor. In particular the torque is slightly above the real one but the base point is almost correct. This produces an output power which is very similar to the real declare one.

2.9 BMW i3

For this model the main geometrical dimensions come from the report [20] although not all of them are known. In particular the PMs in the rotor and the air barriers have been approximated from the pictures from the [25], [27] and [26].

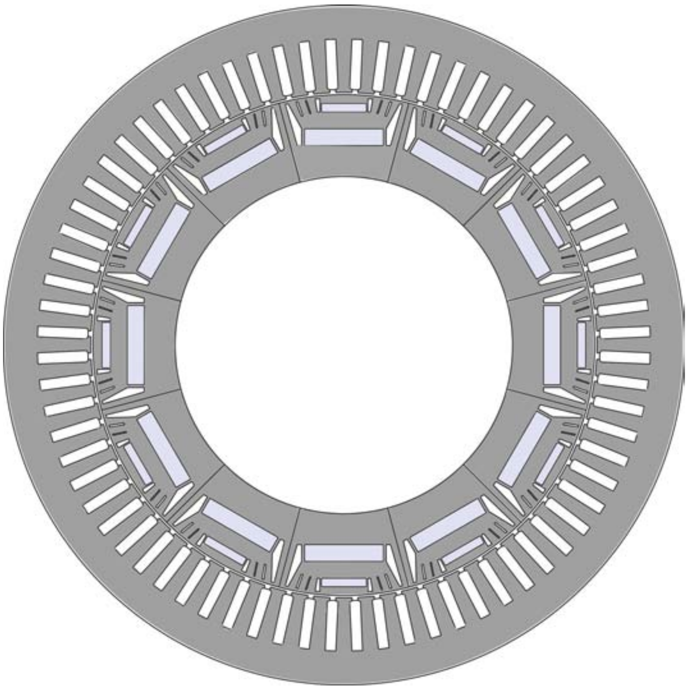

Figure 2.23: Geometry of the i3 model

Bearing this in mind, the following data will be affected by this approximation in the geometry. The geometrical data of the simulated motor are below reported:

L_{stk} mm	D_{ext} mm	D_i mm	g mm	D_r mm	$D_{r,i}$ mm	PM -	Vol_{ext} l
132.2	242.1	180	0.7	178.4	120	2 planar	6.1
h_{slot} mm	$w_{slot,i}$ mm	w_t mm	h_{BI} mm	w_{so} mm	τ_p mm	w_{PM} mm	h_{PM} mm
17.47	3.89	4.1	12.1	2.1	47.1	28 and 16	6 and 3

Table 2.43: Geometrical data of the model BMW i3.

The machine volumes can be evaluate from the values reported in the previous table:

$$Vol_{ext} = \frac{\pi \cdot D_{ext}^2 \cdot L_{fe}}{4} = \frac{\pi 0.2421^2 \cdot 0.1322}{4} = 6.08[l] \tag{2.72}$$

$$Vol_{airgap} = \frac{\pi \cdot D_i^2 \cdot L_{fe}}{4} = \frac{\pi 0.180^2 \cdot 0.1322}{4} = 3.36[l] \tag{2.73}$$

Producer's specifications are reported in the following table:

Some of these values comes from the report [20], and in particular:

Q_s -	p -	T_{max} $[Nm]$	P_{max} $[kW]$	V_{DC} $[V]$	I_c $[A]$	n_B $[rpm]$	n_{max} $[rpm]$
72	6	250	125	360	400	4000	11400

Table 2.44: Producer specifications of the model BMW i3

- $V_{DC} = 360$ [V]
- $P_{out} = 125$ [kW] @ 4000 - 8000 [rpm]
- $T_{max} = 250$ [Nm] @ 4000 [rpm]

It has to be noticed that this machine has an higher number of poles with respect the previous ones, and this is done in order to reduce the back-iron and the rotor yoke at their minimum. Furthermore small air barriers are positioned at the PMs side in order to maximize the reluctance torque component. Observation: this model geometry is not exactly known and some dimensions like tooth and slot width have been approximated. From the DC bus voltage value the peak phase voltage can be evaluated by the following relationship:

$$\hat{V}_{phase} = \frac{360}{\sqrt{3}} = 207[V] \tag{2.74}$$

A small percentage of this evaluated voltage is subtracted in order to take into account the losses in the power supply system. Hence the peak phase voltage is set $\hat{V}_{phase} \cong 200$ [V]. The winding number of conductor and parallel path come from [20] and are reported below:

- $n_c = 9$
- $n_{pp} = 6$

These two values allows to calculate the equivalent number of series conductor: $n_{cs} = 1.5$, which leads to the number of series conductor per phase equal to:

$$N_s = \frac{n_{cs}Qs}{m} = \frac{1.5 \cdot 72}{3} = 36 \tag{2.75}$$

In the hypothesis of developing 250 [Nm] and with 1 [T] of flux density at the air-gap the electrical loading can be estimated:

$$\hat{K}_{s,max} = \frac{T}{\frac{\pi}{4} \cdot D^2 \cdot L_{stk} \cdot \hat{B}_g} = \frac{250}{3.3641 \cdot 10^{-3} \cdot 1} = 74300[A/m] \tag{2.76}$$

The electrical loading allows to approximate the peak value of the conductor current in the following way:

$$\hat{I}_{c,max} = \frac{\hat{K}_{s,max} \cdot \pi D}{m \cdot K_w \cdot N_s} = \frac{74300 \cdot \pi \cdot 0.180}{3 \cdot 0.9659 \cdot 36} = 402.8[A] \tag{2.77}$$

Hence 400 [A] are set as first conductor current. The first simulation with this value produce a output torque of about 205 [Nm] and this means that the current has to be raised up to: 460 [A] in order to have 250 [Nm]. Indeed from this current the following base point values are given by the simulation:

- $T_{dq} = 251.1$ [Nm]
- $T_{mxw} = 233$ [Nm]
- $n_B = 4000$ [rpm]

The following set of useful data still comes from the base point simulation:

PF -	η -	P_{in} $[kW]$	P_{out} $[kW]$	$P_{loss,total}$ $[kW]$
0.87	94.1	111.8	105.2	6.6
$P_{J,s}$ $[W]$	$P_{fe,tooth}$ $[W]$	$P_{fe,BI}$ $[W]$	$P_{fe,total}$ $[W]$	P_{mech} $[W]$
2055.9	3070.4	489.4	3560	998

Table 2.45: Data acquisition in the base point @ 4000 [rpm].

This data set allows to evaluate the following density ratios which are needed in order to compare the different automotive motors:

T_{max}/Vol_{ext} $[Nm/l]$	T_{max}/Vol_{airgap} $[Nm/l]$	$P_{out,max}/Vol_{ext}$ $[kW/l]$	$P_{out,max}/Vol_{airgap}$ $[kW/l]$
41.3	74.7	21.4	38.7

Table 2.46: Torque and power densities of the i3 model.

$P_{loss,total}/Vol_{ext}$ $[kW/l]$	$P_{loss,total}/Vol_{airgap}$ $[kW/l]$
1.1	1.97

Table 2.47: Loss densities of the i3 model.

The new current value is needed in order to calculate a better estimation of the electric loading:

$$\hat{K}_{s,max} = \frac{3 \cdot 0.9659 \cdot 475 \cdot 36}{\pi \cdot 0.180} = 87625[A/m] \tag{2.78}$$

By assuming a rated current equal to 300 [A], which is almost 60 % of the maximum one, the rated electrical loading is evaluated by the following equation:

$$\hat{K}_{s,nom} = \frac{3 \cdot 0.9659 \cdot 300 \cdot 36}{\pi \cdot 0.180} = 55342[A/m] \tag{2.79}$$

Finally the current density is estimated by assuming a $K_{fill} = 0.45$:

$$\hat{J}_s = \frac{712.5}{\overline{2} \cdot 68.64 \cdot 0.45} \cong 16[A/mm^2] \tag{2.80}$$

This value of current density is much lower of the previously presented automotive motors and this comes from the lower electrical loading needed in order to develop a lower peak power but for a longer time. This is required by the substantial vehicular difference between the i3 and the previously analysed models. Indeed the i3 is a pure electric vehicle and the other are mainly parallel hybrid cars.
The mapping of this motor is carried out with the previous cited values and the results are hereafter presented.

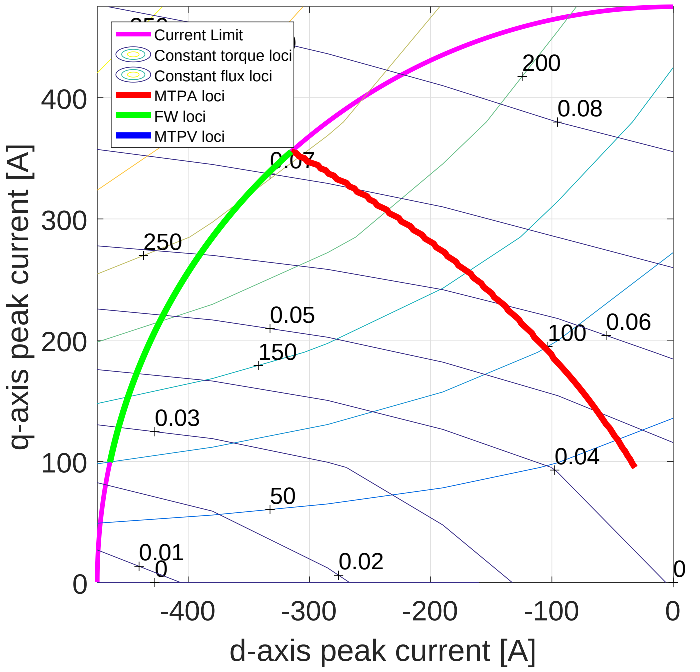

Figure 2.24: BMW i3 motor: dq map.

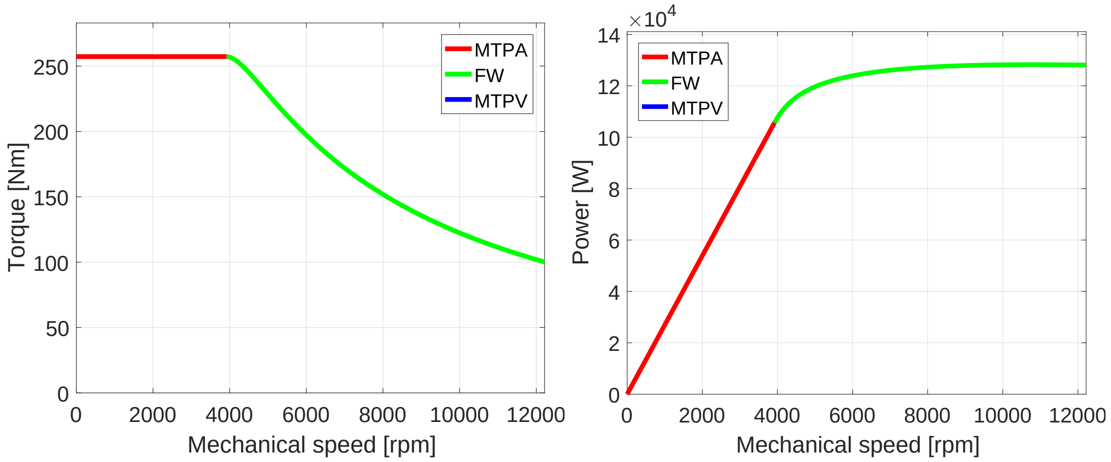

Figure 2.25: BMW i3 motor: torque and power behaviour.

2.9.1 Differences from the real model

The difference between the producer's power vs speed specification [25] and the one obtained by the dq mapping can be justified by several reasons. The first one is the simple fact that the rotor geometry is an approximation of the real one. Another important cause of the different power behaviour can be found in the motor control. Indeed in the figure 2.26 is reported a power curve that can be the result of a control in such a way of maximize the efficiency for each speed. On the contrary the power curve obtained by the dq mapping is the one that follows the maximum achievable power.

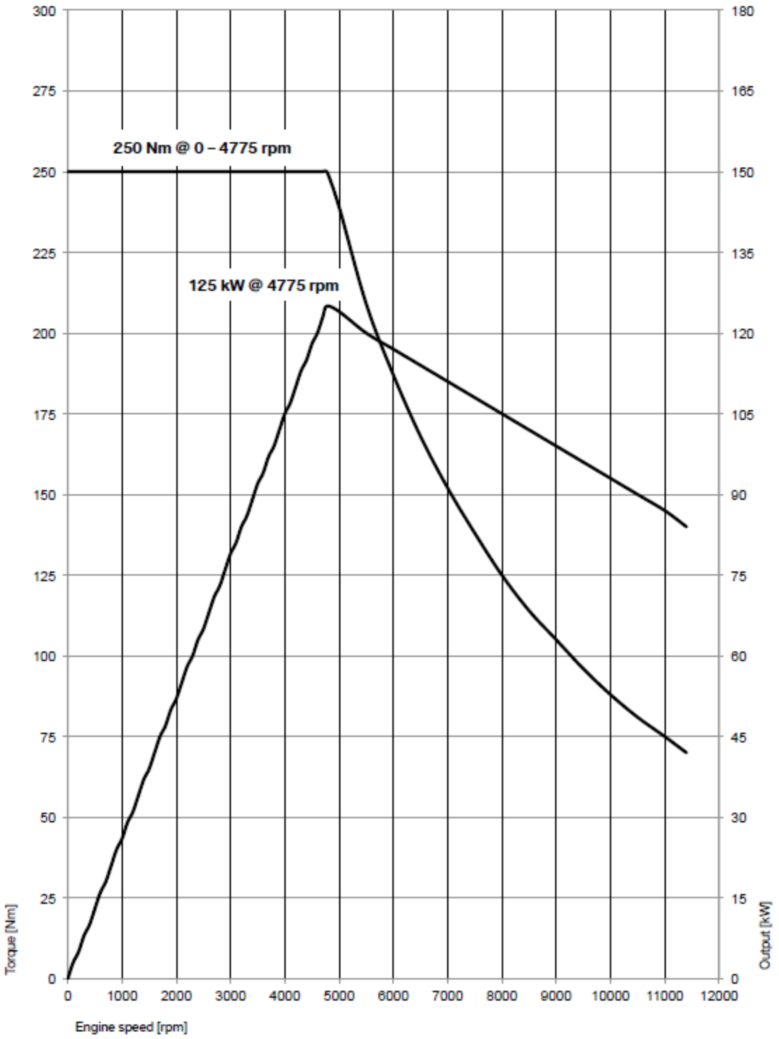

Figure 2.26: Torque and Power specification of BMW

2.10 Automotive comparison

In this section data of the automotive motors are grouped and compared. First of all in the following table the geometrical details of the analysed motors are reported:

Model -	Q_s -	D_{ext} mm	D_{int} mm	g mm	L_{stk} mm	Vol_{int} l	Vol_{ext} l	S_{slot} mm^2
Prius 2004 (F)	48	269	161.9	0.72	84	1.73	4.77	145.16
Prius 2010 (F)	48	269	161.9	0.72	50.8	1.05	2.89	145.16
Prius 2010(P)	48	264	161.9	0.73	50.8	1.05	2.78	158.45
Lexus 600 (P)	48	200	130.86	0.89	135.4	1.82	4.25	76.78
Camry (F)	48	264	161.9	0.72	60.7	1.25	3.32	128.65
Accord M (I)	48	292	196.6	0.8	61.7	1.87	4.11	160.37
LEAF (I)	48	200	130.86	0.89	151	2.04	4.74	76.78
BMW i3 (I)	72	242.1	180	0.8	132.2	3.36	6.09	68.64

Table 2.48: Automotive motors main geometrical data comparison.

This shows the main dimension differences of the automotive motors. There are different external diameters that varies from 200 to 292 [mm] and stack lengths from 50 to 150 [mm]. This fact leads to have different L/D ratios which influence the performance and thermal behaviours. Other differences come from the internal diameter which influences the active volume and the output torque. For example there are Lexus, Accord, Prius 04 and LEAF that own almost the same air-gap volume but they are characterized by different torque and powers. From these geometrical data the comparison in per unit of volume will be presented in table 2.52.
In following table 2.49 the maximum declared output performances are reported, in particular torques, powers and currents are presented. These values together with the internal diameter and the number of slots allows to evaluate the electrical loading which is also reported in the table 2.49.

Model -	Q_s -	2p -	V_{DC} $[V]$	$\hat{I}_{c,max}$ $[A]$	T_M $[Nm]$	$P_{out,max}$ $[kW]$	$\hat{K}_{s,max}$ $[kA/m]$
Prius 2004 (F)	48	8	500	200	400	50	205.1
Prius 2010 (F)	48	8	650	250	207	60	250.7
Prius 2010(P)	48	8	650	250	207	60	250.7
Lexus 600 (P)	48	8	650	400	300	165	157.9
Camry (F)	48	8	650	300	270	105	191.4
Accord M (I)	48	8	700	350	300	124	157.7
LEAF (I)	48	8	375	600	280	80	135.2
BMW i3 (I)	72	12	360	475	250	125	87.6

Table 2.49: Declared automotive motors performances.

The output performances together with the machine volumes and the electrical input values are grouped in table 2.50. These are the required data in order to evaluate power and torque densities and in order to understand the thermal loading of the different motors. The conductor peak current density is also reported. It shows very high peak values and this means that the peak power requested to the motors can be developed for short period of time because all these Joule losses have to be extracted from the cooling system but during the peak power developing the motor is similar to an adiabatic system.

Model -	Vol_{int} $[l]$	Vol_{ext} $[l]$	T_{max} $[Nm]$	$P_{out,max}$ $[kW]$	$\hat{J}_{c,max}$ $[A/mm^2]$	$\hat{K}_{s,max}$ $[kA/m]$
Prius 2004 (F)	1.73	4.77	400	50	24.4	205.1
Prius 2010 (F)	1.05	2.89	207	60	28.5	250.7
Prius 2010(P)	1.05	2.78	207	60	26.1	250.7
Lexus 600 (P)	1.82	4.25	300	165	27.4	157.9
Camry (F)	1.25	3.32	270	105	23.1	191.4
Accord M (I)	1.87	4.11	300	124	20.6	157.7
LEAF (I)	2.04	4.74	280	80	24.6	135.2
BMW i3 (I)	3.36	6.08	250	125	16	87.6

Table 2.50: Output performances together with electrical loadings and machine volumes.

Finally power and torque densities computation are carried out from the previously presented values and reported in table 2.51.

Model -	T_{max}/Vol_{int} $[Nm/l]$	T_{max}/Vol_{ext} $[Nm/l]$	$P_{out,max}/Vol_{int}$ $[kW/l]$	$P_{out,max}/Vol_{ext}$ $[kW/l]$
Prius 2004 (F)	231.4	83.9	28.9	10.5
Prius 2010 (F)	197.1	71.6	57.1	20.8
Prius 2010 (P)	197.1	74.5	57.1	21.6
Lexus 600 (P)	164.8	70.6	94.5	41.6
Camry (F)	216.0	81.3	84.0	31.6
Accord M (I)	160.4	73.0	66.3	30.2
LEAF (I)	137.3	59.1	39.2	16.9
BMW i3 (I)	74.4	41.1	37.2	20.6

Table 2.51: Power and torque densities evaluated on the basis of producer's data.

The values in the previous table 2.51 have to be compared with the following ones which are the same torque and power densities but evaluated on the basis of FEM simulations.

2.11 Conclusion

In this chapter today's automotive motors have been analysed at their maximum output performances. This analysis allows to understand how much these typology of motor are electrically loaded as noticeable in table 2.50. It has to be said that these so high loadings can be sustained for a short period of time in order to avoid overheating in the motor windings. For example these peak performances are guaranteed for periods in the order of 15-20 seconds in the case of the Lexus model [8]. Hence the rated values of torque and power must be assumed to be in the range of 60 % of the maximum ones. This is stated following [25] where the power of 75 [kW] is guaranteed for 30 minutes, which is a proper time considering a classical automotive application.

Anyway the torque densities reported in table 2.52 are very high both considering external or internal volume. This fact comes from the so elevated current loading combined with

Model -	T_{max}/Vol_{int} $[Nm/l]$	T_{max}/Vol_{ext} $[Nm/l]$	$P_{out,max}/Vol_{int}$ $[kW/l]$	$P_{out,max}/Vol_{ext}$ $[kW/l]$
Prius 2004 (F)	235.3	85.3	35.3	12.8
Prius 2010 (F)	269.9	98.1	84.4	30.1
Prius 2010 (P)	225.2	84.7	77.8	29.3
Lexus 600 (P)	163.8	70.2	92.3	39.5
Camry (F)	213.8	80.5	88.9	33.4
Accord M (I)	163.6	74.5	73.8	33.6
LEAF (I)	141.2	60.8	39.2	16.9
BMW i3 (I)	74.7	41.3	41.2	22.8

Table 2.52: Power and torque densities evaluated on the basis of the FEM simulations.

the IPM rotor typology chosen. This allows elevated peak torque ratios but produces also high iron saturation in the motor. The maximum torque density is for the Prius 2004 which has also the higher output torque of 400 [Nm]. This, combined with the lower DC bus voltage (500 V), reduces the base speed compared with other IPM.

The BMW i3 motor has the highest volumes and at the same time the lower electrical loading. This, combined with the higher number of poles, helps in reducing the iron flux density and produces a more equilibrated machine.

Focusing on the power densities the Lexus model is the one with the highest output power and power density. This is caused by the relative high internal volume combined with three magnets and high DC bus voltage (650 V). These three factors combined allow to move the base speed toward higher speeds (5000 [rpm]) and with that high torque it produces the highest output power.

LEAF and i3 motors are similar machines despite the different number of poles. They have the highest volumes and are not too much electrically loaded which leads to similar output power densities. Hence the application of these two motors is different from the Lexus or Camry models. Indeed i3 and LEAF models are the only ones pure electric model. The other IPM motors are developed as engine assistance in fast accelerations and in order to increase the whole power-train efficiency.

Chapter 3

Modified automotive motors

This chapter deals with three geometries previously seen in chapter 2. In particular, the effect of the rotor that changes from IPM to Ferrite assisted REL as well as the pure reluctance is observed and analysed. Hence, the different obtained motors are compared in order to understand how much performance is lost by the new rotors.

3.1 Terms of comparison

The examined machine stators remain unchanged as this section only deal with the rotor shape. The initial IPM rotors have been first replaced with a pure reluctance and then with a PMREL rotor. The magnets in the PMREL are Ceramic Ferrite type. The inverter output has been left untouched in order to compare the motors with the same electrical input. The reason why this choice was made regards the fact that the impact of the rotor type in this section is studied in the same working region of the commercial IPM motors.

3.1.1 Design changes

The following geometries have been chosen as representative of the motors previously seen. They were selected on the basis of their main dimension and number of poles, in particular:

- Prius 2010 P
- Lexus LS600 h
- BMW i3

Model	2p	Qs	D_{int}	L_{fe}	L_{fe}/D_{int}
Prius 2010 (P)	8	48	161.9	50.8	0.314
Lexus LS600 h	8	48	130.86	135.4	1.027
BMW i3	12	72	180	132.2	0.734

Table 3.1: Geometrical parameters of the studied models.

The rotors of the selected geometries have been first changed in pure reluctance ones and then in PM Assisted REL. The reluctance rotors have been designed following the flux lines inside a pure iron rotor and the air barriers were created with a series of arcs that follow the flux lines. Later Ferrite PMs have been inserted in the barriers to produce the PMREL version of the motor. In this way the comparison between different machines can be carried out. The geometries that have been obtained are reported in the figures below.

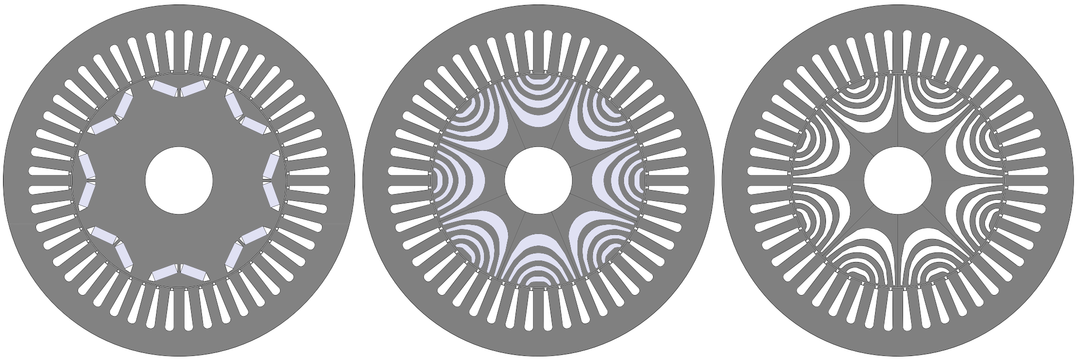

Figure 3.1: Prius rotor comparison

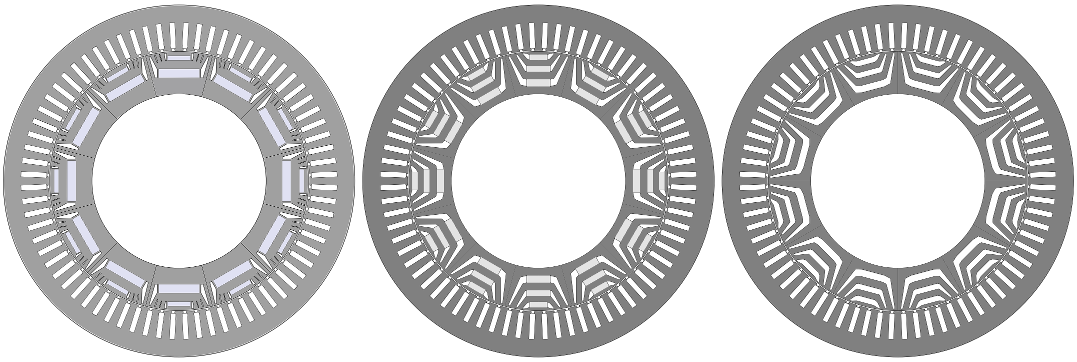

Figure 3.2: BMW rotor comparison

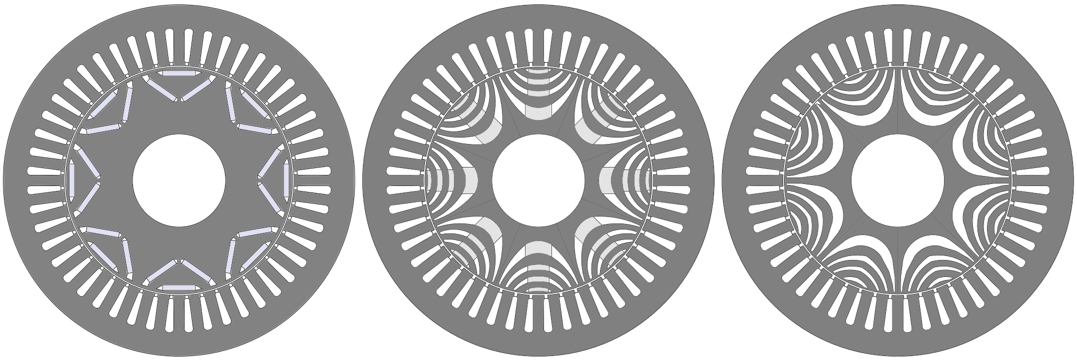

Figure 3.3: Lexus rotor comparison

3.1.2 IPM motors performance comparison

Firstly the three IPM motors presented in chapter two are compared in this section and they will be taken as references.

Model	Q_s	2p	V_{DC}	$\hat{I}_{slot}$	Vol_{int}	Vol_{ext}	n_B	T_B	P_B	PF	$P_{out,max}$
Prius	48	8	650	2750	1.05	2.78	3040	236.5	75.7	0.67	79.1 @ 3410
(p.u.)	1	1	1	1.96	0.57	1.53	0.603	0.79	0.480	0.81	0.50 @ 0.677
Lexus	48	8	650	1400	1.82	4.25	5040	298.6	157.6	0.82	176.8 @ 7725
(p.u.)	1	1	1	1	1	2.33	1	1	1	1	1.12 @ 1.53
i3	72	12	360	712.5	3.36	6.09	4240	246.2	109.3	0.85	134.6 @ 10700
(p.u.)	1.5	1.5	0.55	0.51	1.84	3.34	0.841	0.82	0.69	1.04	0.85 @ 2.12

Table 3.2: IPM motors main data comparison.

The first value to consider is the torque produced in the base point. As expected, when a machine's volume is higher than another one, its output torque too is higher than the other one. This is linked to the fact that the torque is directly proportional to the active volume of the machine. An example of this can be found when comparing Prius (p.u.) and Lexus (p.u.) where the torque ratio is 0.79 vs 1 but the internal volume ratios is 0.57 vs 1. The difference between the evaluated torque ratio and the volume ratio lies in the difference in the electrical loadings of the two machines. Hence the following values are introduced : $\hat{K}_{s,max} = 250.8$ [kA/m] for the Prius and 158 [kA/m] for the Lexus model. The ratio between these electrical loadings is 1.59 vs 1 for the Prius model. If these values are now multiplied, the estimated torque ratio between the two considered models is: $0.57 \cdot 1.58 = 0.9$. The ratio is still higher than the 0.79 of the real torque ratio. This happens because one last parameter has to be taken into account: it is the flux density at the air-gap, respectively 0.77 [T] for Prius and 0.84 [T] for Lexus. The $\hat{B}_{go}$ ratio is equal to 0.916. Eventually the torque estimation between the two motors can be carried out by using the following equation:

$$\frac{T_B}{T_{B,ref}} = \frac{\hat{K}_s}{\hat{K}_{s,ref}} \cdot \frac{Vol_{int}}{Vol_{int,ref}} \cdot \frac{\hat{B}_{go}}{\hat{B}_{go,ref}} = 1.588 \cdot 0.57 \cdot 0.916 = 0.829 \tag{3.1}$$

From the formula 3.1 Prius' estimated torque is equal to 82.9% of Lexus' but this value is slightly different from the real value which is 79%. This difference can be justified on the grounds of the geometrically different rotor which leads to a discrepancy in the reluctance torque component. Hence this comparison is realistic when the rotor is similar, with the same amount of reluctance and PM torque.

The comparison of i3 and Lexus can be carried out by means of similar passages:

$$\frac{T_{i3}}{T_{Lexus(ref)}} = \frac{\hat{K}_{s,i3}}{\hat{K}_{s,Lexus}} \cdot \frac{Vol_{int,i3}}{Vol_{int,Lexus}} \cdot \frac{\hat{B}_{go,i3}}{\hat{B}_{go,Lexus}} = 0.556 \cdot 1.846 \cdot 0.797 = 0.818 \tag{3.2}$$

This value is roughly different from the one obtained which is equal to 82.3 %. An explanation for this difference lies in the fact that these two motors are characterised by a distinct number of poles and a PMs disposition. In particular, as noticed in the figures 3.2 and 3.3 the magnets in the i3 are horizontally placed and there are several small air barriers

that constrain the flux and increase the reluctance torque component. On the contrary in the Lexus IPM the magnets are disposed in a Delta shape that, together with the lower number of poles, results in a higher flux density at the air-gap.
The main terms in the previous formulation (3.1) apart from the volume are the electrical loading and the flux density at the air-gap. If the comparison focuses now on these terms it can be said that the flux density depends on the combination of the magnetic properties relative to the PM inside the rotor with the induced flux density at the air-gap by the stator currents. The other term is the electrical load 2.7 which depends on the number of conductors, the current and the internal diameter. Hence, in order to compare the electric loadings of two similar machines the following ratio is illustrated:

$$\frac{\hat{K}_s}{\hat{K}_{s,ref}} = \frac{m}{m_{ref}} \cdot \frac{K_w}{K_{w,ref}} \cdot \frac{N_s}{N_{s,ref}} \cdot \frac{\hat{I}_c}{\hat{I}_{c,ref}} \cdot \frac{D_{int,ref}}{D_{int}} \tag{3.3}$$

By assuming that all the presented motors have the same number of phases and introducing the simplification that $K_w \cong 1$ the previous equation can be simplified as:

$$\frac{\hat{K}_s}{\hat{K}_{s,ref}} \cong \frac{N_s}{N_{s,ref}} \cdot \frac{\hat{I}_c}{\hat{I}_{c,ref}} \cdot \frac{D_{int,ref}}{D_{int}} \tag{3.4}$$

This ratio can be further simplified if the slot current and the number of slot are introduced. Indeed the series conductor ratio can be written as:

$$\frac{N_s}{N_{s,ref}} = \frac{n_{cs} \cdot Q_s}{m} \cdot \frac{m}{n_{cs,ref} \cdot Q_{s,ref}} = \frac{n_{cs}}{n_{cs,ref}} \cdot \frac{Q_s}{Q_{s,ref}} \tag{3.5}$$

In this way the electrical loadings ratio can be approximated as:

$$\frac{\hat{K}_s}{\hat{K}_{s,ref}} = \frac{Q_s}{Q_{s,ref}} \cdot \frac{\hat{I}_{slot}}{\hat{I}_{slot,ref}} \cdot \frac{D_{int,ref}}{D_{int}} \tag{3.6}$$

The comparison can also involve the base speed which is related to the number of pole pairs and the frequency. When connecting the base speed of two IPM motors, the following formula can be used:

$$\frac{n_B}{n_{B,ref}} = \frac{f}{f_{ref}} \cdot \frac{p_{ref}}{p} \tag{3.7}$$

From the torque estimation and the base speed the output power in the base point is evaluated as:

$$\frac{P_B}{P_{B,ref}} = \frac{T_B}{T_{B,ref}} \cdot \frac{n_B}{n_{B,ref}} \tag{3.8}$$

From the formula 3.1 a similar expression that links the torque to the slot current and other parameters can be obtained. In particular, this can be done by taking the equation 2.8 and decomposing it in the following one:

$$T = \frac{k_w \cdot Q_s \cdot D_{int} \cdot L_{fe}}{4} \cdot \hat{B}_{g,load} \cdot PF \cdot \hat{I}_{slot} = K_{size} \cdot \hat{B}_{g,load} \cdot PF \cdot \hat{I}_{slot} \tag{3.9}$$

This equation directly links the output torque to the slot current and allows a comparison between different types of motors. The terms in it can be grouped in a simpler coefficient:

$$K_T = K_{size} \cdot \hat{B}_{g,load} \cdot PF \tag{3.10}$$

Is this coefficient a good parameter for describing the motor correctly? To answer this question the table below shows all parameters involved in 3.9 and 3.10 and compares them with simulation values.

Model -	K_{size} $[m^2]$	$\hat{B}_{g,load}$ $[T]$	PF -	$\hat{I}_{slot}$ $[A]$	K_T -	T_B $[Nm]$	$K_{T,simulation}$ -
Prius 04	0.157	1.46	0.75	2250	0.172	407	0.181
Prius 10P	0.095	1.44	0.67	2750	0.092	236	0.086
Lexus	0.204	1.31	0.82	1400	0.218	299	0.214
Camry	0.113	1.45	0.75	2100	0.123	268	0.128
Accord M	0.140	1.28	0.81	2100	0.146	309	0.147
LEAF	0.228	1.29	0.85	1200	0.248	293	0.245
BMW i3	0.411	1.12	0.85	700	0.385	246	0.357

Table 3.3: Comparison of the evaluated K_T with the $K_{T,real}$

In this table the coefficients K_T are evaluated by the calculation in 3.9 and $K_{T,simulation}$ comes from the base torque divided by the slot current that has been used in the simulation. The table illustrates that K_T values are similar to the ones obtained from the simulation. As shown in 3.9, K_T represents geometrical and electrical parameters. The machines' dimensions are necessary in order to understand the torque development in the volume, but they cannot describe the torque behaviour on their own. Hence K_T must contain parameters such as the flux density at the air-gap and the Power Factor. The table highlights a very low Power Factor and this is due to the machine's high electrical loading and its saturation level. In these conditions, the angle with the maximum PF is shifted towards higher angles than the MTPA one and this results in a lower PF when the machine is controlled following the MTPA trajectory. This situation is better for the rated torque requirement where the angle of MTPA is similar to the maximum PF angle.
$\hat{B}_{g,load}$ is required because the torque is directly proportional to it (until the iron saturation occurs). On the other hand the power factor is needed in order to understand the vectors position in the dq plane that describe the motor performance. In this way, in a single expression the torque is connected with the slot current by a simple coefficient.

In figure 3.4 there is a brief motivation of the torque coefficient related to the electrical components. Clearly the current vector contained in the expression $\hat{K}_s$ is present. The second term is the voltage on the machine which is related to the air-gap flux density $\hat{B}_{g,load}$. The last term presented in 3.9 is the Power Factor which is directly linked to the angle between the voltage and the current vectors.
This formulation represents a different way to see the electromagnetic torque from [4] and reported below:

$$\tau_{em} = \frac{\mu_0}{g} \frac{D_{int}^2 L_{fe}}{4} \int_0^{2\pi} -U_r(\theta_r) K_s(\theta_r) d\theta_r \tag{3.11}$$

The torque in 3.9 is the same as the one obtained from the equation of the air-gap tangential

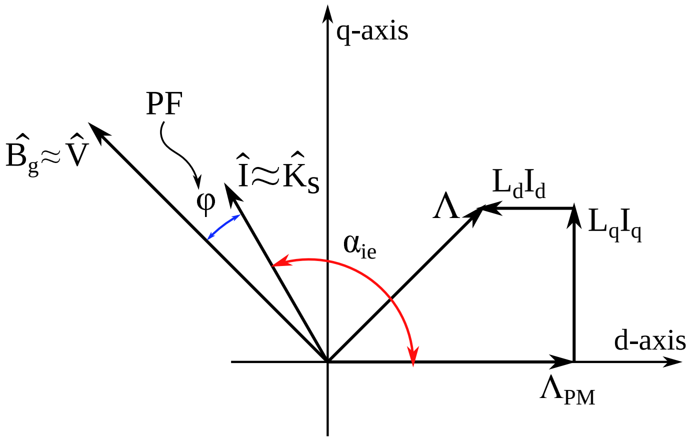

Figure 3.4: Justification of the K_T definition. The graph is related to an IPM machine

force:

$$T = F \cdot \frac{D_{int}}{2} = \frac{\pi}{2} \cdot \sigma D_{int}^2 \cdot L_{fe} \tag{3.12}$$

Where σ is:

$$\sigma = \frac{2}{\pi} \hat{B}_{g,load} \cdot PF \cdot \hat{K}_s \tag{3.13}$$

Hence from this simplified torque expression the base point power can be approximated as:

$$P_B = T_B \cdot \omega_m \cong K_T \hat{I}_{slot} \cdot \frac{2\pi f_B}{p} = K_{Power} \cdot \hat{I}_{slot} \cdot f_B \tag{3.14}$$

3.1.3 Conclusion

In this section the basis for a torque comparison has been established. The expressions 3.9 and 3.14 describe the performances of a generic machine. The coefficients K_T and K_P indicate the load of the machine in a different way, indeed:

$$K_T = \frac{k_w \cdot Q_s \cdot D_{int} \cdot L_{fe}}{4} \cdot \hat{B}_{g,load} \cdot PF = K_{size} \cdot \hat{B}_{g,load} \cdot PF \tag{3.15}$$

$$K_P = K_{Power} = \frac{2\pi}{p} \cdot K_T = \frac{2\pi}{p} \cdot K_{size} \cdot \hat{B}_{g,load} \cdot PF \tag{3.16}$$

Thanks to these coefficients, the comparison of different motors can be carried out.
The discrepancies between simulated and real values are caused by several factors, one above all is the uncertainties on the exact values of the real motors described. From table **??** the following comparisons can be made:

$$\frac{T_B}{T_{B,ref}} = \frac{K_{size}}{K_{size,ref}} \cdot \frac{PF}{PF,ref} \cdot \frac{\hat{B}_{g,load}}{\hat{B}_{g,load,ref}} \cdot \frac{\hat{I}_{slot}}{\hat{I}_{slot,ref}} = \frac{K_T}{K_{T,ref}} \cdot \frac{\hat{I}_{slot}}{\hat{I}_{slot,ref}} \tag{3.17}$$

$$\frac{P_B}{P_{B,ref}} = \frac{T_B}{T_{B,ref}} \cdot \frac{n_B}{n_{B,ref}} = \frac{K_P}{K_{P,ref}} \cdot \frac{\hat{I}_{slot}}{\hat{I}_{slot,ref}} \cdot \frac{f_B}{f_{B,ref}} \tag{3.18}$$

Model	K_{size}	$\hat{B}_{g,load}$	PF	K_T	K_P	$\hat{I}_{slot}$	n_B	T_B	P_B	$K_{T,real}$	$K_{P,real}$
Prius	0.095	1.45	0.67	0.092	0.145	2750	3040	236.5	75.7	0.086	0.135
(p.u.)	0.465	1.12	0.82	0.422	0.424	1.96	0.60	0.791	0.48	0.402	0.401
Lexus	0.204	1.3	0.82	0.218	0.342	1400	5040	299	157.6	0.214	0.336
(p.u.)	1	1	1	1	1	1	1	1	1	1	1
i3	0.411	1.12	0.85	0.391	0.409	700	4240	246.2	109.3	0.357	0.373
(p.u.)	2.02	0.86	1.04	1.794	1.196	0.5	0.84	0.823	0.694	1.668	1.110

Table 3.4: Output coefficient and per unit values of the IPM geometries

These prediction will be applied to the REL and PMREL motors in the following section.

3.2 Investigation on REL and PMREL

In this section the passages that have been done for IPM motors are applied to the reluctance and PMREL built on the IPM geometries. In particular what is wanted is to obtain a comparison of these different typologies of motor based on the previously defined coefficients: K_T and K_P. The simulations of the reluctance and PMREL motors were carried out while maintaining the same values for:

- Main dimensions such as: L_{stk}, D_{int}, g, Q_s
- Slot current: $\hat{I}_{slot}$
- DC-bus voltage: V_{DC}

In this way the comparison focuses on the differences in the air-gap flux density and the different power factor.
First of all, it is known that the PF changes because of the different α_{ie} between the REL and IPM motors. Particularly, by neglecting the iron saturation, α_{ie} angle changes from $\cong 135$ in an IPM to $\cong 45$ in a REL (this angle is between the d-axis and the current vector). This different angle produces a variation in the relative position of voltage and current vectors, i.e. it changes the angle φ between voltage and current vectors. Indeed in an IPM machine φ assumes a lower value with respect the same angle in a reluctance motor.
In a PM assisted REL the q-axis positioned Ferrite magnet produces a flux that helps reduce the q-axis flux and causes a clockwise rotation of the resulting flux as shown in figure 3.7. In this figure the Ferrite PM flux is represented by the red vector and the same goes for the voltage variation. Hence the Ferrite magnets allow the consequent rotation of the voltage vector that moves closer to the current vector and this helps reduce the angle φ, hence the power factor is improved.

The analysis starts from the torque and power values evaluated in the base point. The base speed is also needed in order to understand the output power and the operative frequencies.
Once, it was believed that from the rotor changing, in particular from the IPM to the reluctance typology, the flux in the machine would have been lower. In this way the reluctance type would have presented a lower winding voltage compared with an IPM type at the

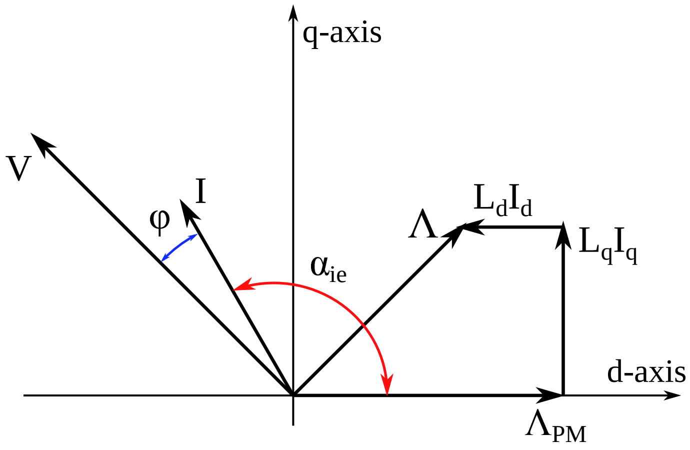

Figure 3.5: Vector diagram of an IPM machine. It is noticeable the low φ angle with-respect the one in the following figures.

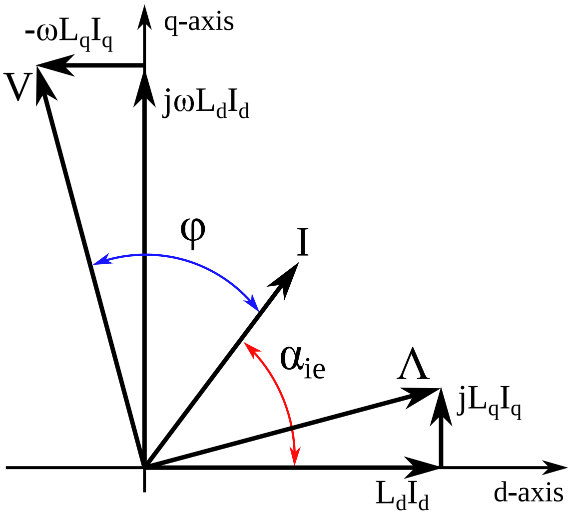

Figure 3.6: Vector diagram of a REL machine.

same speed. This fact would have allowed an higher base speed for the reluctance motor with-respect the equivalent IPM.

As shown in table 3.5 this situation does not occur, and the explanation for this lies in the high saturation of the analysed machines. Indeed the automotive motors presented in chapter 2 are characterised by high values of $\hat{K}_s$ in order to satisfy the peak torque demand. This requested performance is guaranteed for a short period of time because of the machine's thermal limits, but throughout this period the saturation in the machine is so high that the flux variation is very limited with the current variation. Hence those elevated fluxes almost induce the same voltage at the winding terminal at the same speed, meaning that the voltage limit allowed by the inverter and its DC bus is reached at almost the same base speed. In order to increase the base speed two ways are available: the first one is to lessen the saturation by reducing the electrical loading, but this affects the output torque. The second one is to increase the inverter voltage limit although it implies to enhance the electric power of the whole system. A middle way consists in changing the stack length of the motor in order to reduce the flux, but again the output torque is affected by this action. When the base point is reached the machine is working at its maximum values of current

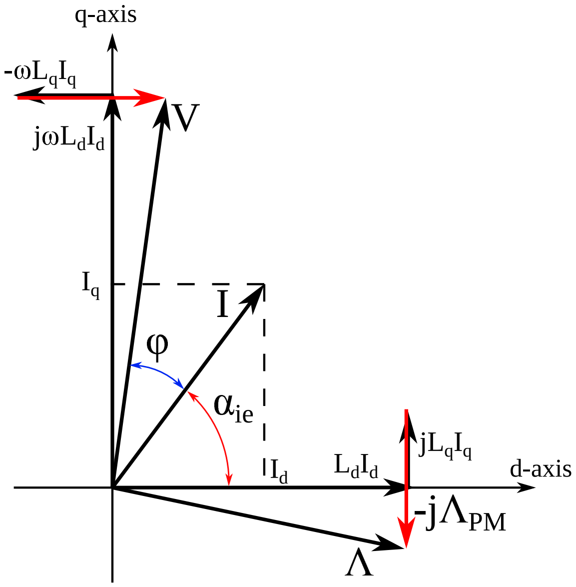

Figure 3.7: Vector diagram of a PM-assisted-REL machine. The red arrows show the assistance of the Ferrite PM.

and voltage. After the base point there is Flux Weakening region, where the current angle α_{ie} is increased while current and voltage vectors are maintained at their maximum in absolute value. This allows the machine to develop its maximum output power in the Flux Weakening region.
As far as pure reluctance motors are concerned, a phenomenon occurs when they are required to work at higher speeds than the base one. By slightly incrementing the speed, the voltage increases beyond the established DC bus limits due to the high saturation. Hence Flux Weakening region (FW) is very restricted and the operational behaviour rapidly starts to follow MTPV region. During the MTPV, it happens that the current is reduced in order for the flux in the machine to be diminished too, enabling to follow the maximum torque per voltage at high speeds.
Due to the high saturation in the MTPV region the current needs to decrease very quickly for a considerable flux reduction leading to a rapid loss of torque with the speed increment. To increase the FW and MTPV performance the introduction of PM assistance is required. On the other hand, the IPM motor shows the FW and MTPV best performances due to higher flux from the rare earth magnets. In the following table 3.5 the same parameters for IPM, PMREL and REL motors are reported in order to have a first base point comparison. In this table the maximum voltages influence the base speeds and the peak powers. Then there are the slot currents and the internal volumes that are related to the machine torque production. The number of poles are requested in order to understand the operational different frequencies. The Power Factor is evaluated in the base speed at the maximum loading. As previously explained it is very low because of the saturation in the machine.

As it has been done in the previous section, two coefficients K_T and K_P are evaluated for the different typologies of motor from the equations introduced in 3.15 and 3.16. The computation starts from the values obtained in the base point simulation. Because of the identical stator geometry K_{size} inside the two equation is the same for all geometries. As a result the terms that change in the coefficients' evaluation are only the PF and the $\hat{B}_{g,load}$. These two coefficients are reported below:

Model	Qs	2p	V_{DC}	$\hat{I}_{slot,max}$	Vol_{int}	Vol_{ext}	n_B	T_B	P_B	PF_B	$P_{out,max}$
Prius 10P											
IPM							3040	236.5	75.7	0.67	79.1 @ 3410
(p.u.)							0.603	0.79	0.48	(0.81)	0.50 @ 0.68
PMREL	48	8	650	2750	1.05	2.78	3100	217.5	70.5	0.64	71.2 @ 3160
(p.u.)	1	1	1	1.96	0.57	1.53	0.615	0.73	0.45	(0.78)	0.45 @ 0.63
REL							2990	169.7	53.1	0.54	53.3 @ 3020
(p.u.)							0.593	0.57	0.34	(0.66)	0.34 @ 0.6
Lexus											
IPM							5040	298.6	157.6	0.82	176.8 @ 7725
(p.u.)							1	1	1	(1)	1.12 @ 1.53
PMREL	48	8	650	1400	1.82	4.25	4910	216.9	111.5	0.64	115.1 @ 5260
(p.u.)	1	1	1	1	1	2.33	0.97	0.73	0.71	(0.78)	0.73 @ 1.04
REL							4820	189.3	95.5	0.58	97.8 @ 5085
(p.u.)							0.96	0.63	0.61	(0.71)	0.62 @ 1.01
BMW i3											
IPM							4240	246.2	109.3	0.85	134.6 @ 10700
(p.u.)							0.841	0.82	0.69	(1.04)	0.85 @ 2.12
PMREL	72	12	360	712.5	3.36	6.09	4370	172.5	78.9	0.63	87.5 @ 5800
(p.u.)	1.5	1.5	0.55	0.51	1.84	3.34	0.867	0.58	0.50	(0.77)	0.56 @ 1.15
REL							4330	142.1	64.5	0.56	69.6 @ 5250
(p.u.)							0.859	0.48	0.41	(0.68)	0.44 @ 1.04

Table 3.5: Comparison between different typologies of motors at the maximum load.

$$K_T = \frac{k_w \cdot Q_s \cdot D_{int} \cdot L_{fe}}{4} \cdot \hat{B}_{g,load} \cdot PF = K_{size} \cdot \hat{B}_{g,load} \cdot PF \tag{3.19}$$

$$K_P = \frac{2\pi}{p} \cdot K_T = \frac{2\pi}{p} \cdot K_{size} \cdot \hat{B}_{g,load} \cdot PF \tag{3.20}$$

The table 3.6 shows that the so-called K_T coefficient is a good indicator for the torque developed in the cases of IPM and PMREL typologies of motor. Due to the presence of the PM torque component the IPM and PMREL motors present an higher K_T with-respect the reluctance type motor built on the same volume. This suggests that the torque density in the IPM motors is greater than the REL torque density, but this first observation will be better evaluated at the end of this chapter.

Each one of the three simulated cases illustrate an overestimation of the output torque, especially in the reluctance motor this coefficient overestimates the output torque too much. Probably, the main causes are:

- High $\hat{B}_{g,load}$ of the investigated reluctance motors. This produces high saturation in the iron that causes a non-linearity in the torque with the current.
- Simplified method that does not take into account the whole harmonic content of the air-gap flux density.

Model	Q_s	k_W	D_{int}	L_{FE}	$\hat{B}_{g,load}$	PF	$\hat{I}_{slot}$	K_T	K_P	T_B	$K_{T,real}$	$K_{P,real}$
Prius 10P												
IPM	48	0.96	0.1619	0.0508	1.51	0.66	2750	0.094	0.148	236	0.086	0.135
PMREL					1.35	0.64	2750	0.082	0.128	218	0.079	0.124
REL					1.39	0.54	2750	0.071	0.112	166	0.060	0.095
Lexus												
IPM	48	0.96	0.13086	0.1354	1.26	0.84	1400	0.216	0.339	299	0.214	0.336
PMREL					1.17	0.66	1400	0.158	0.248	220	0.157	0.247
REL					1.31	0.58	1400	0.155	0.243	190	0.136	0.213
BMW i3												
IPM	72	0.96	0.180	0.1322	1.12	0.84	700	0.390	0.408	248	0.354	0.371
PMREL					0.95	0.65	700	0.254	0.266	185	0.264	0.277
REL					0.95	0.56	700	0.219	0.229	147	0.210	0.219

Table 3.6: Comparison between different typologies of motors.

Later graphs of the maximum performances in torque and power of the evaluated motors are reported. The general performance has a drop when the rotor is changed from the IPM to the PMREL and REL and this is caused mainly by the lower air-gap flux density and lower PF.

Following the order in table 3.6 the first model the figures correspond to, is Prius 2010.

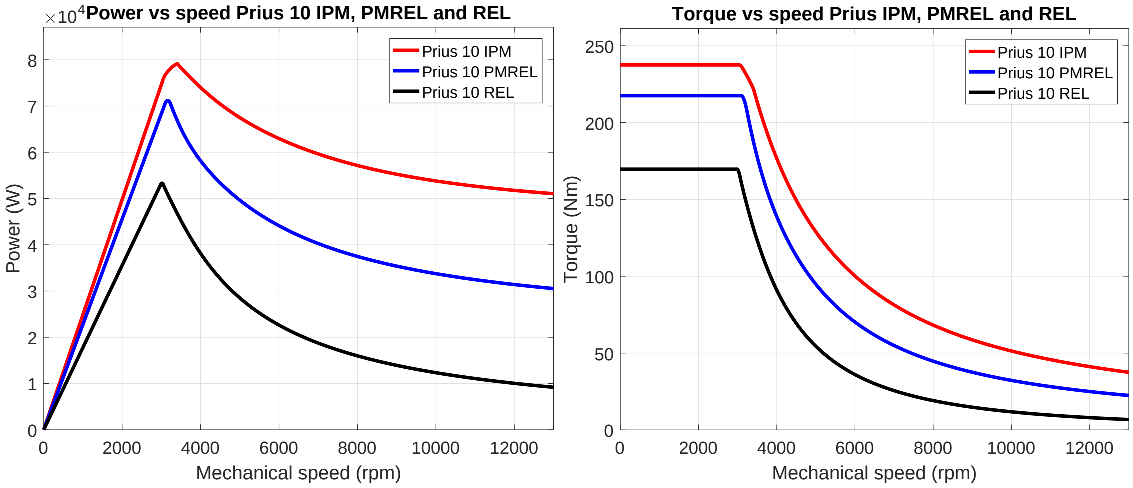

Figure 3.8: Power and torque behaviour of the Prius 10 based models.

As noticeable in figure 3.8 the torque in this model has a sharp drop after the base point. This fact finds an explanation when observing that the $\hat{B}_g$ of this model is the highest. This implies that in the machine iron there is an elevated saturation degree that produces a fast decreasing in the supply current in order to comply with the voltage limit imposed to the machine. This torque drop causes the decrement of the output power at high speeds.

This behaviour is seen in all the Prius 10 based models, in particular the reluctance one shows a peak power above 50 [kW] around 3000 [rpm] but then the output power cannot be kept at those levels ad presents a very rapid drop. In regards to the output performances, it is important to notice that the PMREL version of this motor is comparable with the producer data exposed in the previous chapters up to 6000 [rpm]. This comes from the entirely filled barrier adopted in this motor which greatly helps to improve the high speeds performances.

The following figures represent the torque and the power behaviour of the Lexus based motors.

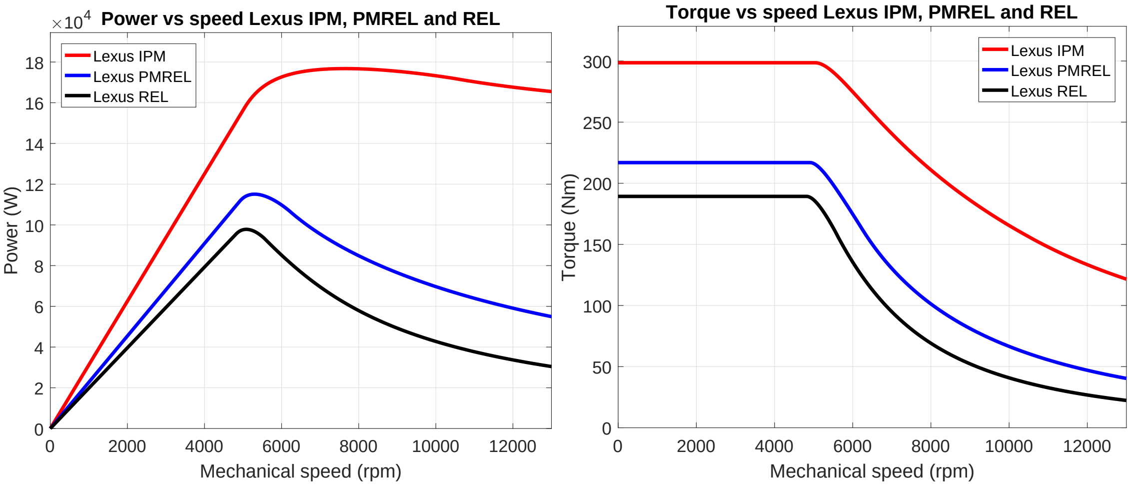

Figure 3.9: Power and torque behaviour of the Lexus based models.

This model shows remarkable performance differences between the three types of motors. The IPM has the highest torque and power and the PMREL version is very far from the IPM performances. The torque of the IPM model presents a smooth drop with the speed rise. This means that the corresponding power is nearly flat as it is clearly visible from the graph on the left.

PMREL version presents a torque which is almost two third of the IPM one but its power does not present flat behaviour at high speeds as expected. It always needs to be charged at the different PM flux density that helps into maintain flux weakening for a wider speed range and so MTPV starts at higher speeds with-respect the PMREL model. The base point is almost the same for the three types which means that PMREL has about the same flux of the IPM model.

The high Torque difference between the two typologies is justified from the observation that PMREL barriers are filled only in minor part with-respect the Prius ones. The reluctance version has half the IPM power in the peak point and presents a power curve at high speeds which is almost half the PMREL one.

The following figures 3.10 represent the BMW i3 model based comparison. The IPM model present the flattest power curve among the analysed motors. The PMREL peak power is almost equal to 70 % of the IPM one but, in this model too, the PMREL motor does not have a flat power behaviour despite being smoother than the others. This occurs because this motor presents the lowest electrical loading which, together with the higher number of poles, helps reduce the flux in the machine, producing a better power behaviour with-respect the 8 poles motors. The pure reluctance type does not show good output

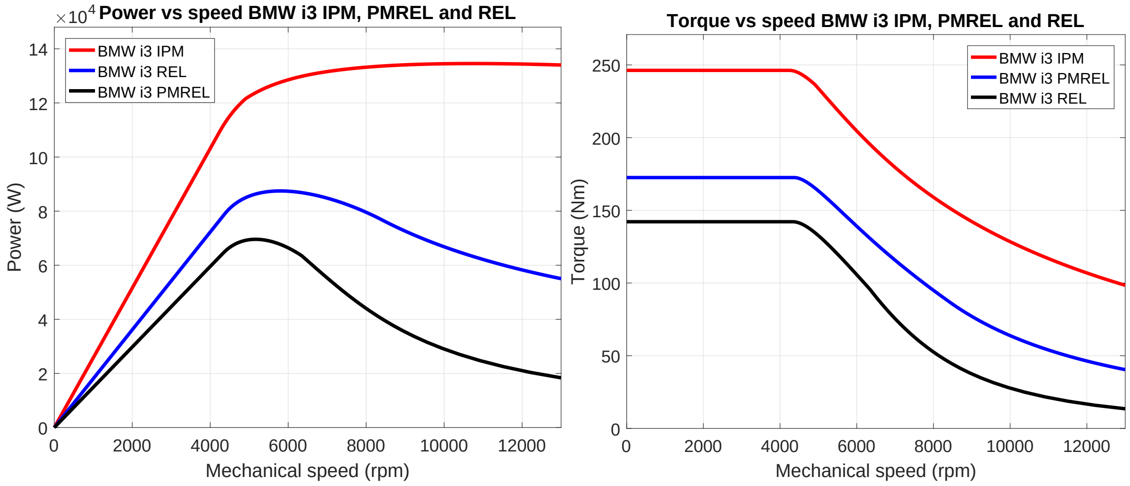

Figure 3.10: Power and torque behaviour of the BMW based models.

values because the reluctance torque is lowered from the higher number of poles. This indicates that for a possible pure reluctance automotive alternative the number of poles must be limited in such a way to have good saliency ratios.
In all three model based motors it is clearly visible how the IPM version presents the highest output performances, and this is related to a better efficiency and power factor. The PM assisted Reluctance motor assumes a middle position between the IPM and the reluctance versions. In the Prius case PMREL is comparable with the IPM version because of the elevated saturation which causes a mediocre exploitation of material also in the IPM version. This feature is not present in the Lexus based models where the PMREL torque is almost equal to two third of the IPM version. BMW based PMREL motor has the flattest power curve compared with the previous PMREL, and this is generated by the lower motor electrical loading and saturation.
Reluctance motor versions present very low output values compared with an IPM and this means that in order to have the same performances this type of machine needs to be larger in dimensions or must be supplied by higher currents or voltages. In an automotive application a wider machine is not the best one because it leads to a heavier power-train and would affect the vehicle's overall performances [22], [10].

3.2.1 Rated torque values

The previous tables and graphs were obtained at the maximum electric input values which lead to the highest torque achievable from the different geometries and typology of motors. This procedure evaluates the motors at their maximum output and creates the following problems:

- High saturation in the magnetic circuit
- Low Power Factor
- High Joule losses
- Non-optimal operational behaviour
- Transient peak values due to thermal limits

The first reported one causes a lot of uncertainties on the simulations. In particular, the current in the slot is not used at its best with high saturation, because, in order to have a small increment of the torque, the current needs to be significantly increased. This implies a higher addition of apparent power with respect to a smaller gain in active power. For this reason the Power factor is very low and the currents required for the maximum output torque contains a large amount of imaginary current [6].
The thermal analysis is needed in order to know the time for the maximum torque to be sustained. Generally in automotive motors these values follow the order of 20 seconds because the typical usage of the vehicle is limited at lower torques. The maximum torque values are reached in particular situations, such as sudden accelerations or road slope raising [28].
The rated torque corresponds to that value that can be sustained for an hypothetical infinite time without critical over-temperatures in the windings. From the articles [27], [22], [8] it is evinced a rated load equal to the 60 % of the maximum one. This value will be maintained for the motors in analysis.
So far the rated loads of the different machines are compared, and in this situation we expect the following performance improvements:

- Lower $\hat{B}_{g,load}$ which leads to a less saturated iron, so to lower Iron Losses
- Higher power factor
- Lower current density, hence lower Joule losses
- Lower Output torque and it is expected varying in a different way from the linear one with the current
- General improvement of efficiency and PF conditions

In the following table the values assumed to be equal to the rated ones are presented.

Model	Qs	2p	V_{DC}	Vol_{int}	Vol_{ext}	$\hat{I}_{s,rated}$	$\hat{K}_{s,rated}$
Prius	48	8	650	1.05	2.78	1650	150
(p.u.)	1	1	1	0.57	1.53	1.96	1.35
Lexus	48	8	650	1.82	4.25	840	111
(p.u.)	1	1	1	1	2.33	1	1
i3	72	12	360	3.36	6.09	420	77
(p.u.)	1.5	1.5	0.55	1.84	3.34	0.5	0.69

Table 3.7: Rated input data of the three analysed automotive IPM motors.

These values are used to let the FEM simulations at the rated load begins. From those simulations the following output are produced and reported in the table 3.8.

This table, together with the one in the previous section, brings to deduce that the lower current leads to a lower flux density in the air-gap and in the iron. This is confirmed both for the BMW and Lexus models, but not for the Prius. Indeed, in the Prius IPM model such a high slot current causes the saturation of the whole machine and induces a too high value of air-gap flux density. These conditions produce a general worse exploitation of the machine active volume. In particular the power factor is lower than the other two models' even in the rated load condition. On the contrary the BMW model is characterized

Model	Q_s	k_w	D_{int}	L_{iron}	$\hat{B}_{g,rated}$	PF	$\hat{I}_{s,rated}$	K_T	K_P	T_B	$K_{T,real}$	$K_{P,real}$
Prius 10P												
IPM	48	0.96	0.1619	0.0508	1.45	0.75	1650	0.103	0.173	165.6	0.100	0.157
PMREL					1.26	0.72	1650	0.086	0.135	147.0	0.089	0.140
REL					1.31	0.59	1650	0.073	0.115	116.3	0.071	0.111
Lexus												
IPM	48	0.96	0.13086	0.1354	1.19	0.88	840	0.214	0.336	176.8	0.211	0.331
PMREL					1.07	0.66	840	0.144	0.226	120.1	0.143	0.225
REL					1.27	0.56	840	0.145	0.228	100.1	0.119	0.187
BMW i3												
IPM	72	0.96	0.180	0.1322	0.97	0.88	420	0.351	0.367	132.4	0.315	0.329
PMREL					0.77	0.61	420	0.193	0.202	76.4	0.182	0.191
REL					0.70	0.50	420	0.144	0.151	56.5	0.135	0.141

Table 3.8: Comparison between the different typologies of motors at rated load.

by a low iron saturation, so low that the power factor of the PMREL and REL models is higher at maximum load than the rated one. This is mainly due to the higher number of poles in the machine that helps reduce the flux. Lexus model presented the higher values of PF at the maximum load although it is exceeded by the Prius PMREL power factor at rated load. Prius model is characterized by a rated PF higher than the other two PMREL. This is caused by the slot current reduction which enables to reach better values of flux density and also by the higher amount of Ferrite PM in the rotor with-respect the other two PMREL. From these observations the following criteria are set up for the future PMREL and REL motors design:

- Slot current limited in order to reach $\hat{K}_s$ of 150 [kA/m] in overload and 100 - 110 [kA/m] at rated loadings
- $\hat{B}_g$ not above 1 - 1.2 [T]
- Higher V_{DC} for better behaviour at high speeds
- Optimize the available volume in order to maximize the machine iron
- Increase the number of poles which allows to minimize the back iron an helps in reducing the flux density
- PMREL machines with the maximum possible amount of Ferrite in the rotor

3.2.2 Torque comparison

The comparison between different types of motor has been accomplished by keeping the main dimension unchanged, i.e. the machine volume. Other important parameters that are equal for each motor are the electrical ones such as V_{DC} and $\hat{I}_{slot}$. In this way the machine's electrical loading is the same. Performances are reported in the following graphs. The first comparison refers to the torque vs α_{ie}, which is needed in order to understand the MTPA trajectory of the motors.

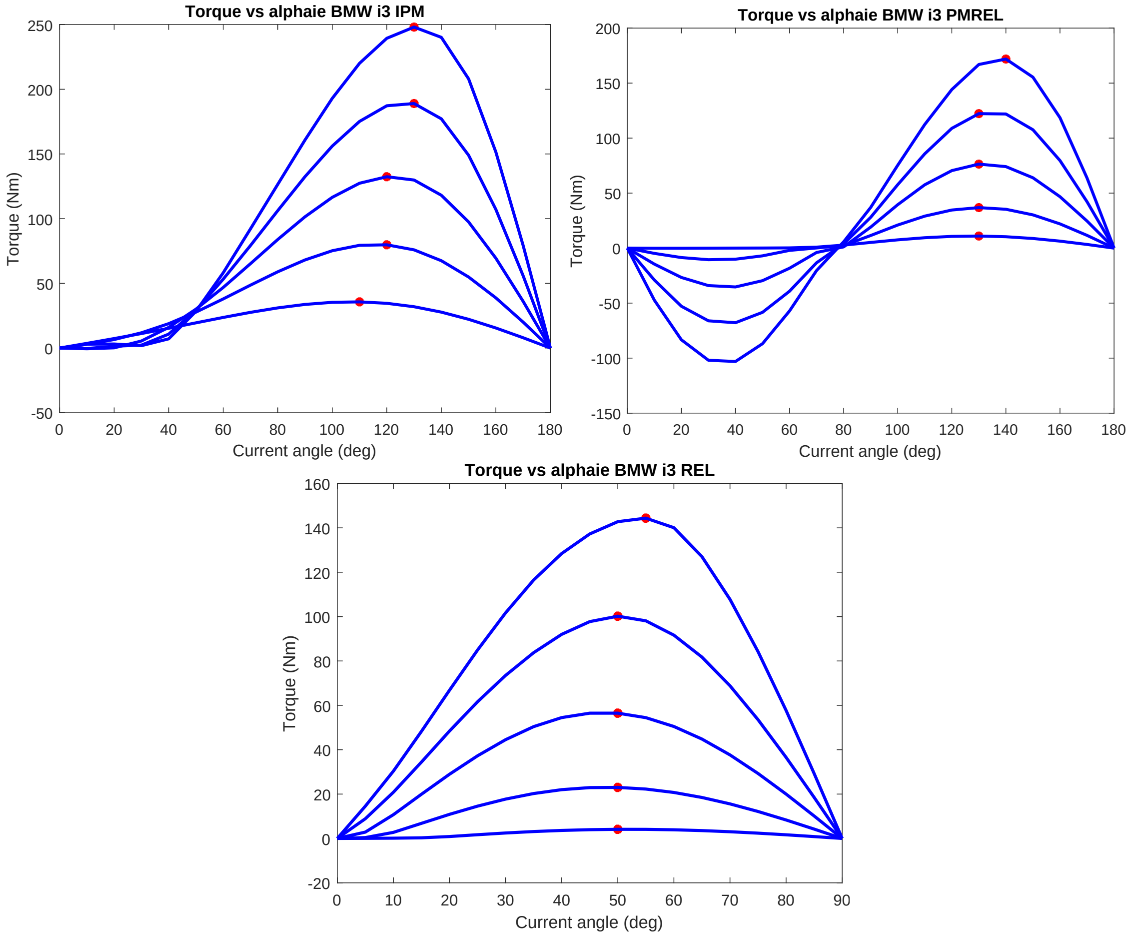

Figure 3.11: BMW i3 IPM, PMREL and reluctance versions: Torque vs α_{ie}.

These three graphs 3.11 are relative to the BMW i3 model with the three different types of rotors. The curves have been obtained from currents varying in a range between 20% up to 100% of the maximum one. These graphs underline that the output torque is lower for PMREL and REL motors. The maximum output torque is approximatively equal to 73% and 60% respectively for PMREL and REL rotor at the maximum current loading. As it can be seen BMW based motors do not present high saturation and this can be evinced from the MTPA trajectory points. Indeed they do not shift towards electrical angle higher than 130-140° for IPM and PMREL types and 50-55° for the reluctance model. Still regarding the torque behaviour it is evident that there is an almost linear variation of the torque with the current and this is again enabled by the low saturation of the magnetic circuit.

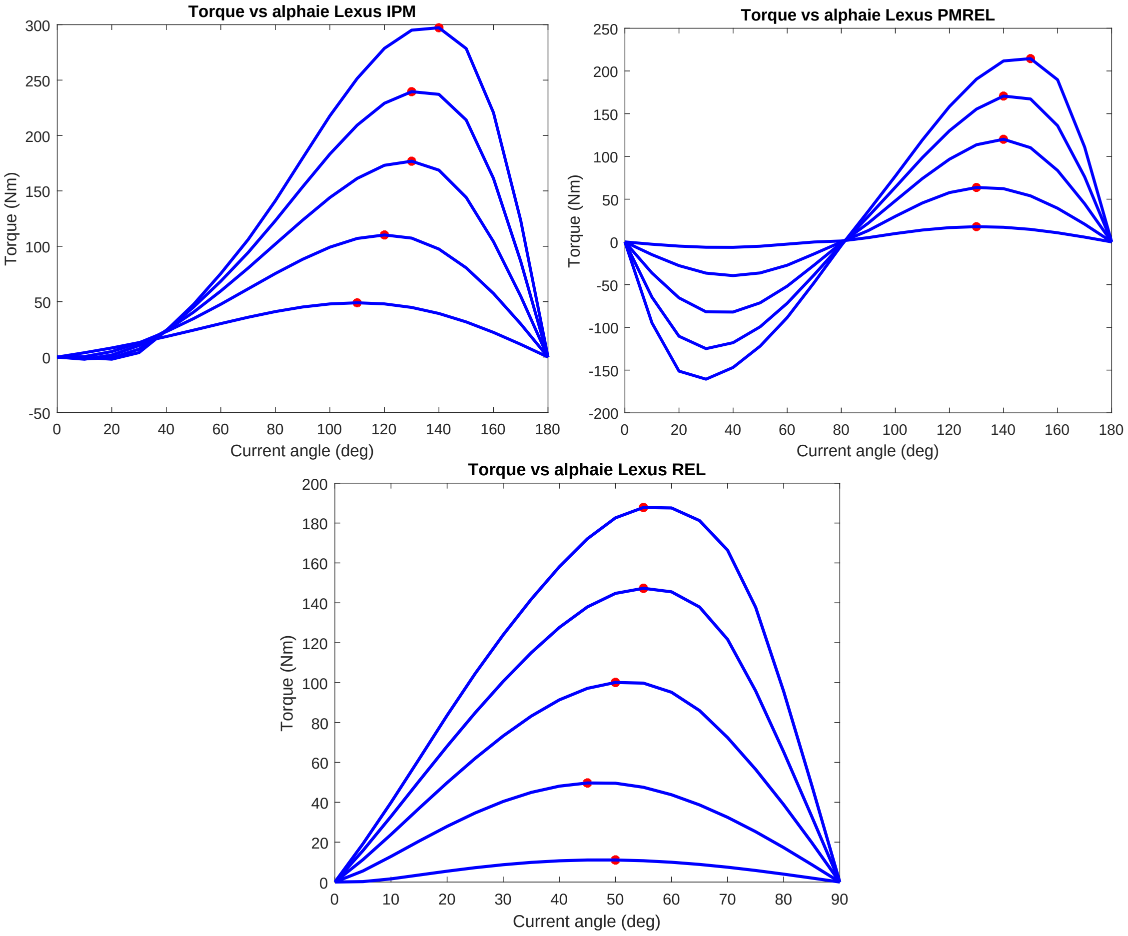

Figure 3.12: Lexus IPM, PMREL, REL: Torque vs α_{ie}

The figures above 3.12 present the torque variation with the current and the angle for the Lexus based motors. Differently from the BMW based models here the current angle moves above 140° and this is index of an increasing saturation for high current values. The maximum output torque is approximately 74% and 63% respectively for PMREL and REL rotor at the maximum loading. The saturation has an higher presence for this model with-respect the BMW motors but this does not cause an evident non-linearity in the output torque as a function of the current.

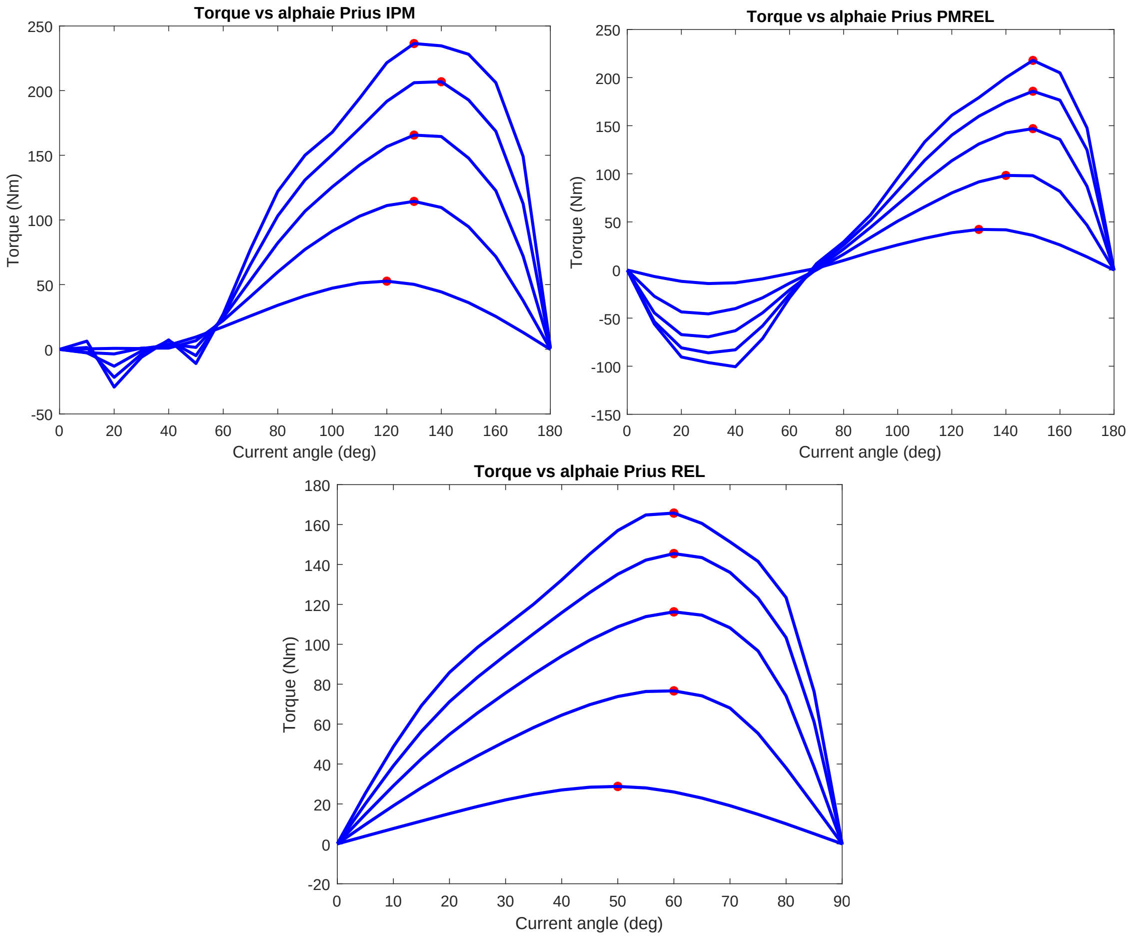

Figure 3.13: Prius IPM, PMREL, REL: Torque vs α_{ie}

In the figure 3.13 torque vs α_{ie} graphs of the Prius 2010 based motors are presented. The particular shape of the torque as function of α_{ie} is due to the V-shape disposition of the magnets. This motor is characterised by a non-negligible saturation and this is evinced from the shape of the graphs. Particularly the current values above the 60% produce an output torque lower than the one obtained in linear conditions. The saturation causes also the shifting of the MTPA trajectory toward higher angles. The maximum output torque is approximately 92% and 70% respectively for PMREL and REL rotor at the maximum load. This puts in evidence that for this model, characterised by these so high values of electric and magnetic loading, the PMREL is a good alternative in order to economize the motor production.

In the following page there are all the different models an typologies output torque directly compared. This allows to understand how much gap there is between the same motor with different rotors and between the differently shaped rotors.

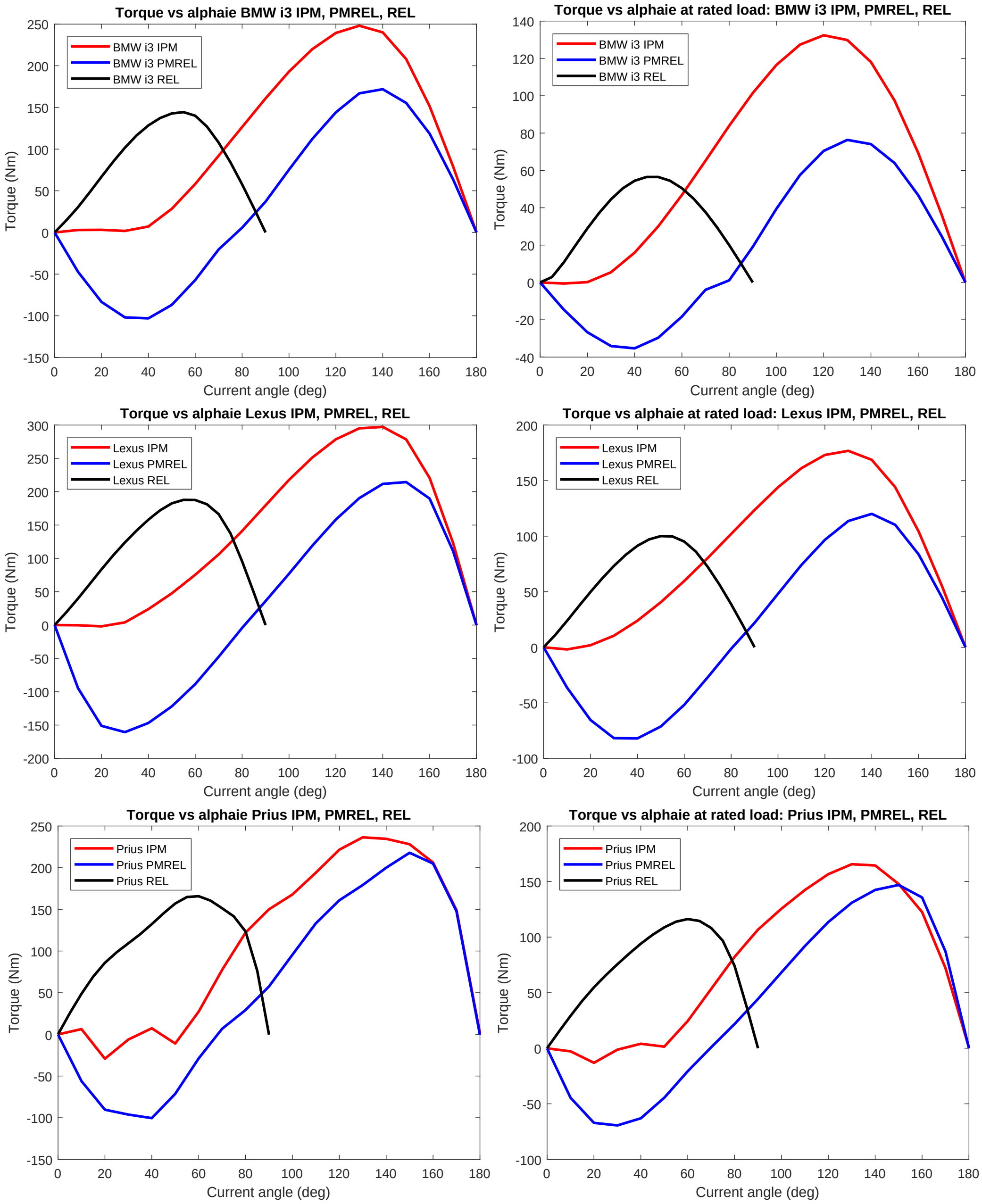

Figure 3.14: Torque vs α_{ie} of the different models. On the right there are maximum load values and on the left at rated load

As previously mentioned, it is evident from this comparison that the BMW and Lexus models suffers from an almost linear drop of torque with the variation of supply current. For Prius based models it is not the same because of the high saturation which starts before the hypothesized rated current equal to the 60% of the maximum one. For the same reason the PMREL model is comparable with the IPM one regarding the torque development. Lastly, the last comparison is between the same typology of motor at the maximum current.

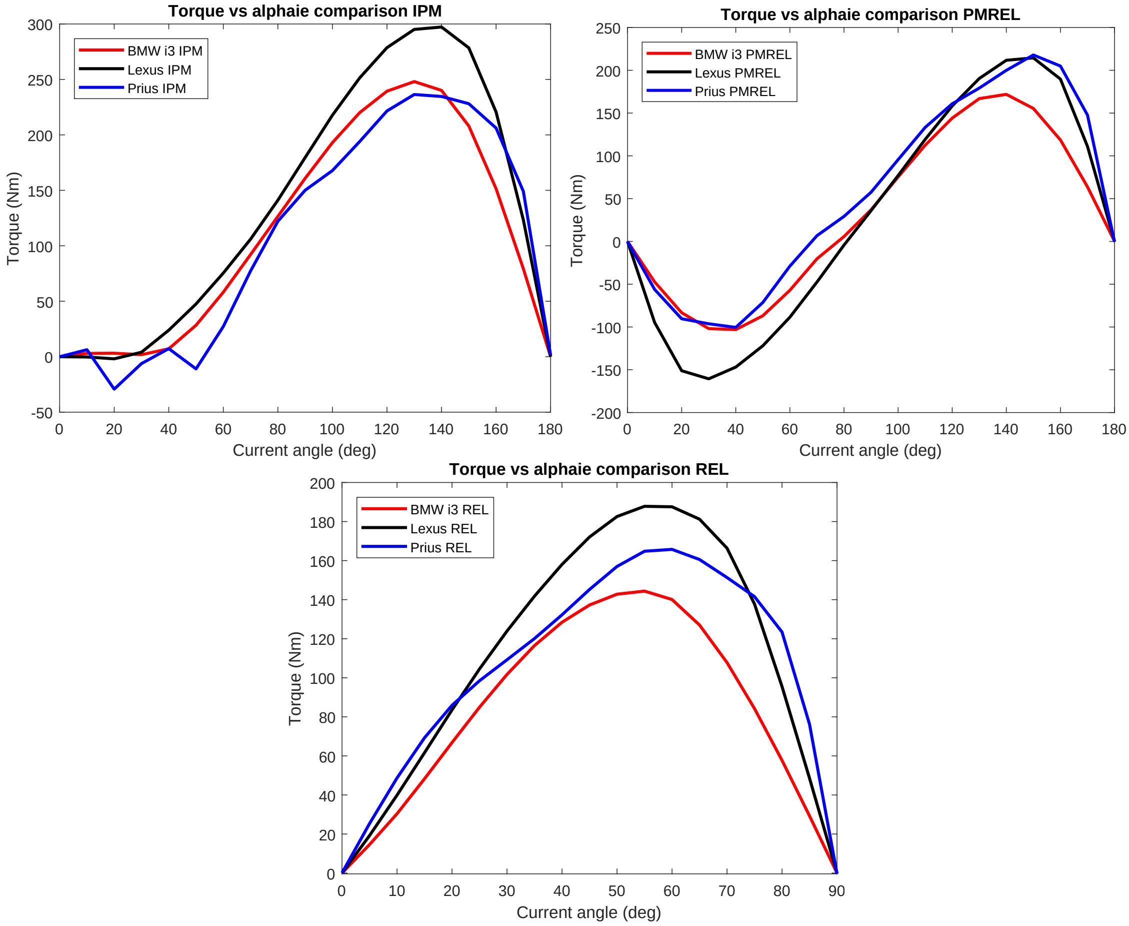

Figure 3.15: Torque vs α_{ie} at maximum load comparison of the same rotor typology.

From figures 3.15 it is evinced that the i3 based models (red one) have a lower output torque than the other two in the case of PMREL and REL despite having an higher active volume. This is caused by the lower $\hat{K}_s$ of this motor and by the higher number of poles in this model which causes a drop in the L_d/L_q ratio. This influences the torque produced by the reluctance effect causing a drop in the total output torque.

In all the three cases the Lexus stator based models (black one) are the best solution because the high active volume is assisted by a good value of electrical loading which does not cause a too elevated saturation in the machine.

3.2.3 Power factor comparison

Power factor (PF) of the machines is a fundamental parameter that carries information about the angle between the supply voltage and current. PF varies as function of many operative conditions, for example when the machine is under lower loads it is unsaturated and the PF assumes high values because the current vector is near the voltage. When the operative load increases the current vector moves, following the MTPA trajectory, toward higher angles due to the increasing saturation. This causes an increment of the angle between voltage and current vectors producing a worsening in the PF value [11]. In the case of a highly saturated machine (high currents), the worst condition occurs for the PF. Indeed the fluxes $\Lambda_{d,q}$ have the same slope, and L_d,L_q reach similar values (worsening of the saliency ratio ξ). This implies that the current vector increases its angle but this is not sufficient in order to cover the increment in the voltage angle caused by the higher fluxes and inductances. PF vs α_{ie} graphs are reported below for the different models.

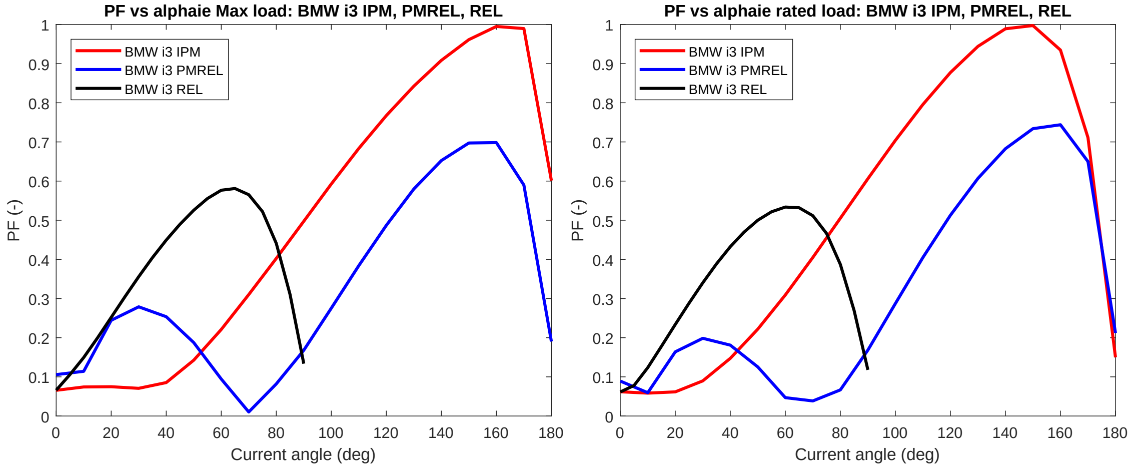

Figure 3.16: PF comparison of the BMW i3 based models. On the right at maximum load and on the left rated load.

In the figure 3.16 the PF of the BMW based models are reported. It represents that the IPM model reaches the $PF = 1$ at 160° and 150° respectively at maximum and rated loadings. These two angles are different from the MTPA angle at the same loads and this can be a cause of discrepancy between the maximum output values obtained by the previous simulations and the producer data. In other words, the real motor control can be done following the maximum of the PF at high speeds and this causes a drop in the output power different from the simulated one in section 2.9.
The PMREL model is characterised by a PF above 0.7 both at maximum and rated load. On the other hand, REL motor has a PF lower than 0.6 and the peculiarity is that the PF is higher at the maximum load than the rated one. This fact can be explained stating that the flux required to magnetize the machine is still low at the rated load and reaches the right values for loads above the hypothesized 60%. This occurs both because of the absence of the PM flux inside the rotor and because of the high number of poles in this machine.

In figure 3.17 the PF of the Lexus models are reported. This IPM model reaches the $PF = 1$ only at rated load for an angle of 160°. On the contrary at the maximum loading the power factor reaches its maximum value above 0.9 but not equal to one. This can be clarify by assuming that both the current and voltage vectors moves at higher angles at such high loads. These vectors shifting cause the current and voltage vectors without ever overlapping with each other. As a consequence the PF cannot reach the unitary value.

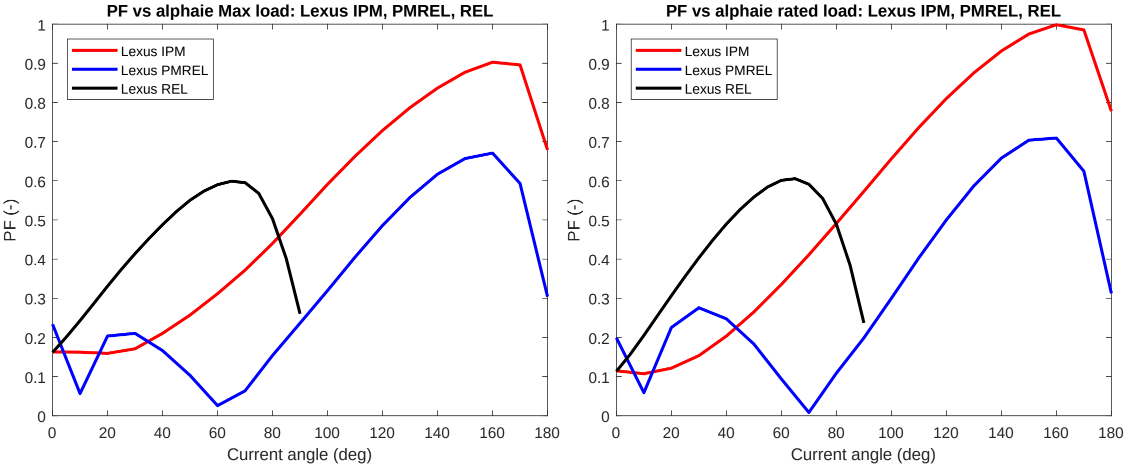

Figure 3.17: PF comparison of the Lexus based models. On the right at maximum load and on the left rated load.

The PMREL motor has PF above 0.65 in the maximum load and reaches values above 0.7 for rated loads. The REL model is characterised by PF in the range of 0.6 but at high loading the angle of maximum PF moves toward 65°.

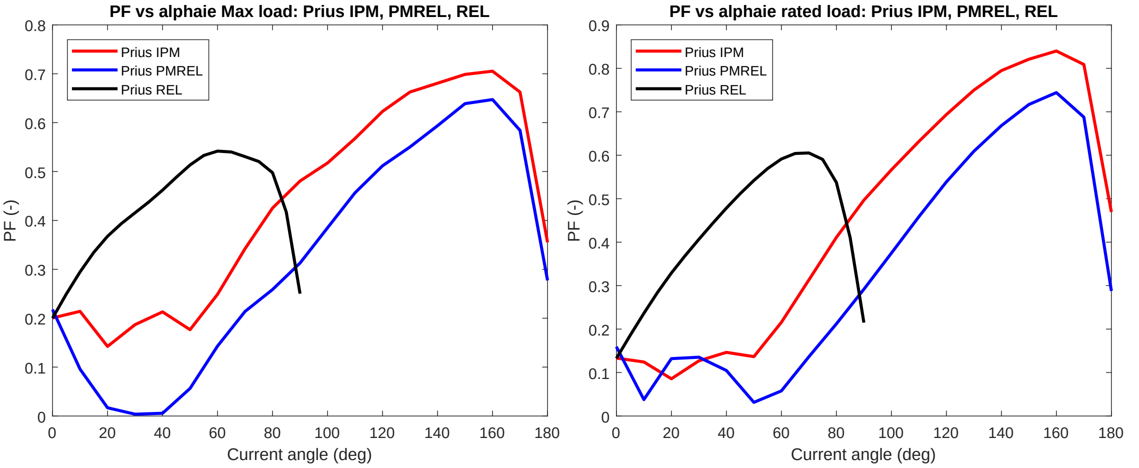

Figure 3.18: PF comparison of the Prius based models. On the right at maximum load and on the left rated load.

The Prius based models PF are reported in figure 3.18. This model, as previously mentioned, is affected by an high saturation of its magnetic circuit. This leads to an overall low power factor and this finds a further confirmation in the figure 3.18, which shows how the PF never reaches the unitary value. The same goes for the rated load condition, where the PF reaches 0.85, that is to say a very low value for this type of motor. Prius PMREL is affected by the same saturation level but the PF of this type is still comparable with the other two PMREL models. The Prius REL is the characterised by the lowest PF at maximum load, equal to about to 0.55.

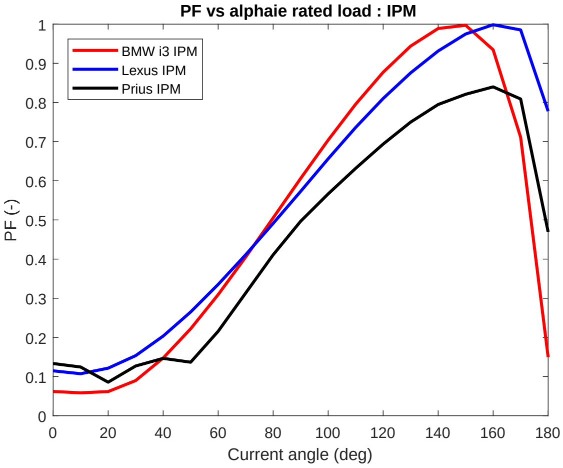

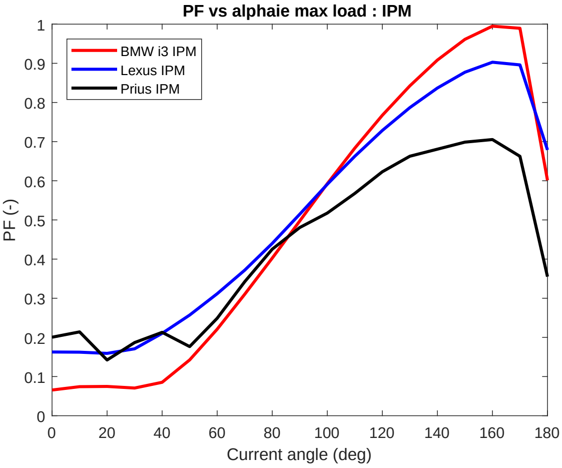

Figure 3.19: IPM motors PF comparison. On the right at maximum load and on the left rated load.

In figure 3.19 the IPM's power factors previously described are directly compared. The maximum PF value reached is a sort of saturation index, indeed the Prius IPM (black) is the worst one both in case of maximum and rated load. In particular this low PF is a disadvantage of this IPM motor compared with the others because it produces an higher amount of inductive current that needs to be compensated.

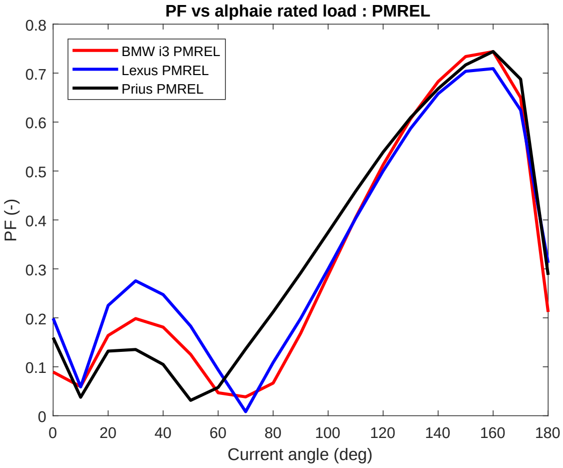

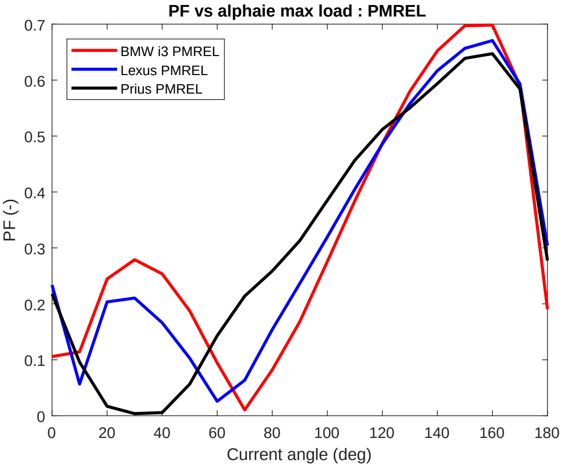

Figure 3.20: PMREL motors PF comparison. On the right at maximum load and on the left rated load.

The PMREL motors PF are compared in figure 3.20. Differently from the IPM models there is not a marked difference at the rated load where, surprisingly, Prius PMREL model shows a slightly higher PF than the other two models. Prius PMREL loses its leading where the comparison is made at the maximum loading where also Lexus overcome Prius and i3 PMREL is the best one.

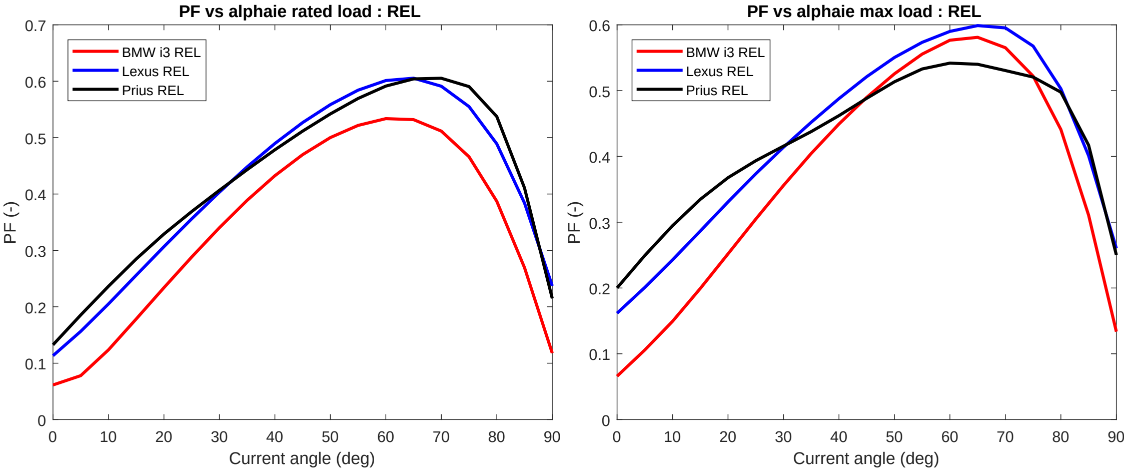

Figure 3.21: REL motors PF comparison. On the right at maximum load and on the left rated load.

Undoubtedly REL motors show the lowest power factor compared with the previous model. Their values are presented in figure 3.21. The Lexus based model is the most balanced one because the peak value of its PF does not change with the load and stays at about 0.6 which is a very low value compared with the IPM power factors. As mentioned before the Prius model has the worst PF of the group and BMW REL is characterized by an increment of PF with the load.

3.3 High speed behaviour

this section presents and comments the high speed behaviour of the analysed machines.

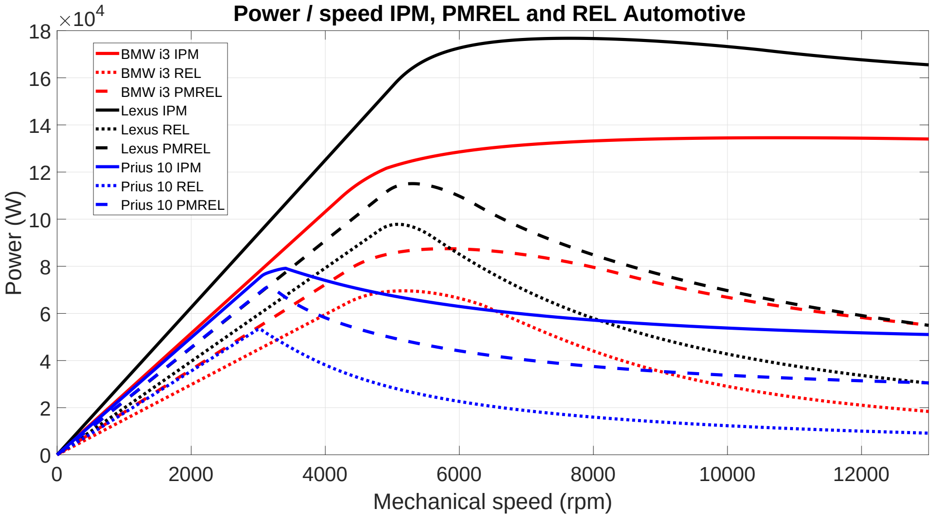

Figure 3.22: Power vs speed of the studied IPM, PMREL and REL models.

In the two figures 3.22 and 3.23 the power and torque behaviour vs the motor speed are reported. The IPM models (continuous line) are evidently the most performing motors. They are characterised by the highest torque and power values with-respect the other types. These motors have the highest slope of the power curve because their output torque is the maximum one between the models. After reaching the base speed IPM motors present

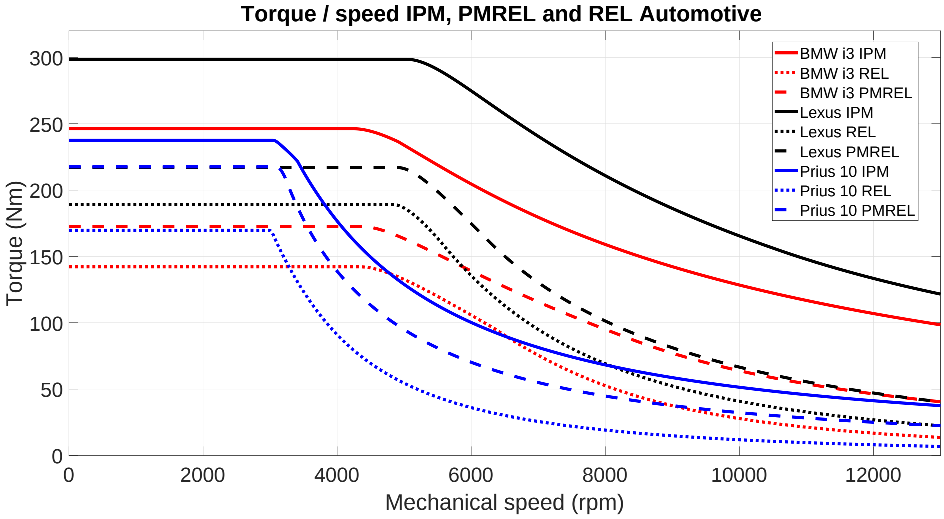

Figure 3.23: Torque vs speed of the studied IPM, PMREL and REL models.

a very large area where the power is stable. This behaviour is particularly present in the Lexus and BMW i3 models. The Prius IPM has a lower maximum power and after the peak value is reached the power presents a slow and steady decrease until the maximum speed value which is about 50 [kW]. As mentioned before these output powers are obtained from the maximum achievable electrical input, without considering a possible controlling algorithm.

When it comes to the PMREL models, they are characterised by a lower maximum output torque value and this produces a power curve with a lower initial slope. At the maximum electrical loading fluxes in the machines are too elevated and this causes an almost stable position of the base speed which is similar for the different motor typology built on the same model. After the base speed PMREL presents a maximum peak power which is near the base point in the case of Lexus and is almost equal in Prius. Only the i3 with PMREL rotor shows a flat power curve between the base speed and almost twice the base speed. This behaviour is mainly caused by the low saturation of the model which allows to maintain high currents even after the base point reaching. Hence in the BMW based model the flux weakening operative region is considerably longer than the other two models. An interesting fact is that at high speeds the i3 PMREL and Lexus PMREL converge toward the same power which is slightly above 50 [kW]. This convergence is caused by the rapid torque drop of the Lexus PMREL which, for speeds above 8000 [rpm] has almost the same shape and values of the i3. Prius PMREL has an output torque similar to the IPM one and this is the same for the base points, but the PMREL torque has a faster drop than the IPM one and at high speeds has almost half of the IPM's power. Hence in the two figures the PMREL version of the different models exhibits all its limits at high speeds. These limits can be exceeded by increasing at the maximum the amount of Ferrite PM inside the rotor in order to increase the short-circuit current helping the flux weakening region to persist for a longer speed range.

Reluctance motors are the less performing models. Powers are slightly higher than half of the IPM values and at high speeds the comparison is even worse. At 13000 [rpm] the maximum power of a reluctance motor is about 30 [kW] for the Lexus REL. The i3 is the REL which loses higher power with-respect the PM models. This is caused by the lower L_d/L_q ratio from the high number of poles. The powers at maximum speed of the

REL model with-respect the IPM are: 22% for Lexus, 15 % for BMW and 20% for Prius. Generally speaking for these Reluctance motors characterised by so elevated electrical loading after two times their base speed they lose too much performance. Hence they are competitive for this purpose only if the electrical loading is reduced and the base speed is moved toward the highest possible speed.

Model	V_{DC}	$\hat{I}_{c,max}$	n_B	T_B	P_B	$P_{out,max}$	T_{13krpm}	P_{13krpm}
Prius 10P								
IPM	650	250	3040	236.5	75.7	79.1 @ 3410	37.73	51.05
PMREL	650	250	3100	217.5	70.5	71.2 @ 3160	22.45	30.53
REL	650	250	2990	169.7	53.1	53.3 @ 3020	6.84	9.25
Lexus								
IPM	650	400	5040	298.6	157.6	176.8 @ 7725	122.2	165.5
PMREL	650	400	4910	216.9	111.5	115.1 @ 5260	40.4	55
REL	650	400	4820	189.3	95.5	97.8 @ 5085	22.46	30.5
BMW i3								
IPM	360	460	4240	246.2	109.3	134.6 @ 10700	98.5	134
PMREL	360	460	4370	172.5	78.9	87.5 @ 5800	40.6	55.1
REL	360	460	4330	142.1	64.5	69.6 @ 5250	13.2	18

Table 3.9: Output data comparison for the IPM, PMREL and REL version of the automotive motors.

Model	n_B	T_B	P_B	$P_{out,max}$	T_{13krpm}	P_{13krpm}
Prius 10P						
IPM	1	1	1	1.05 @ 1.12	0.16	0.674
PMREL	1.02	0.92	0.93	0.94 @ 1.04	0.095	0.40
REL	0.98	0.72	0.7	0.70 @ 0.99	0.029	0.12
Lexus						
IPM	1	1	1	1.12 @ 1.53	0.409	1.05
PMREL	0.97	0.73	0.71	0.73 @ 1.04	0.135	0.349
REL	0.96	0.63	0.61	0.62 @ 1.01	0.075	0.194
BMW i3						
IPM	1	1	1	1.23 @ 2.52	0.40	1.226
PMREL	1.03	0.70	0.72	0.80 @ 1.37	0.165	0.504
REL	1.02	0.58	0.59	0.64 @ 1.24	0.053	0.165

Table 3.10: Motor comparison in p.u. with-respect the IPM base values.

Chapter 4

Synchronous PMREL proposed for automotive applications

This chapter offers a description of the main requirements for the design of PMREL motor. As explained in chapter three the reluctance motor has an output performance in the base point equal about to 60% of an IPM motor characterized by the same dimensions [5]. This different performance is mainly caused by:

- absence of the rotor PM and its torque component
- higher saturation in the rotor that causes an higher "field" current
- difference in the L_d / L_q ratio

This performance gap can be reduced by the introduction of Ceramic-Ferrite PM in the rotor barrier [6], [5]. This PM produces its own flux that particularly helps the machine in the flux weakening region at high speed.

4.1 Preliminary discussion

As previously explained in chapter three, some limits need to be given in order for the machine to be well designed. The main limitations of this kind of motor are:

- Electrical loading
- Magnetic loading

These two parameters influence the whole behaviour of the machine. In particular a too elevated electrical loading will cause overheating in the conductors and saturation in the magnetic circuit. The overheating causes degradation in the conductor insulation and this leads to a reduced lifetime of the product. Saturation causes non linearities in the torque production and a drop in the power factor of the motor. Both electrical and magnetic loading lead to higher losses in the motor. The first one in the copper losses due to the higher current density and the second one in the iron losses due to the higher flux density reached in the narrow iron paths of the magnetic circuit. Another important consequence of the saturation is that the saliency ratio decreases and this brings to lower torque developed from the machine at higher loads. Hence the first two limits that are here imposed to the machines are:

- Limited current in order to reach $\hat{K}_s$ of 150 [kA/m] in overload and 100 [kA/m] for rated loading
- $\hat{B}_g$ in the order of 1-1.2 [T]

4.2 Considerations on the choice of the stator

This section presents several different combinations of poles and numbers of slots in order to understand which one is the best for automotive purposes. The main constrains here are:

- Maximum conductor peak current of 550 [A]
- Maximum DC-bus voltage of 345 [V]
- $D_{ext} = 256$ [mm]
- $L_{stk,max} = 180$ [mm]

These limits are imposed from the initial request for this type of motor. As said above the maximum electrical loading will be kept under 150 [kA/m] to avoid worse operational behaviour. In order to satisfy this limit the conductor current will be forced to decrease when the number of slot is high as it can be noticed in table 4.1.
In the following table the possible geometries for an automotive PMREL motor are reported. The number of slot per pole per phase varies from one to four. The number of conductor in the slot is fixed to an even number to allow wires transposition. In particular the conductors have to be *hairpin* type. These kind of conductors are rectangular-shaped and allow to better fill the slot. In order to contain these conductors the slot are rectangular-shaped and the K_{fill} is about 0.7 [12], [15]. In table 4.1 the highlighted rows contains slot geometries which allow the insertion of the rectangular wire.

Figure 4.1: Hairpin winding example

These geometries have been simulated with a maximum electric loading of 140 [kA/m] in order to satisfy the imposed limits and have a small safety factor. The rated loading is about 60 % of the maximum one, which is in the range of 80 [kA/m].

These geometries are characterised by an $L_{stk} = 100$ [mm] and by an air-gap diameter of about 180 [mm]. The main results of the geometries in table 4.1 are reported in the following table 4.2.

2p	q	Q_s	n_{cs}	$\hat{I}_{c,max}$	$\hat{K}_{s,max}$	ws	hs	wc	hc′	$\hat{J}_{s,max}$
4	3	36	4	550	134.5	8.2	16.5	7.4	3.1	23.6
4	4	48	4	425	138.5	6	19	5.4	3.9	20.3
6	2	36	4	550	134.5	8.2	16.5	7.4	3.1	23.6
6	2.5	45	4	450	137.5	5.9	21	5.3	4.1	20.7
6	3	54	4	375	137.5	5.4	17.3	4.8	3.4	22.9
6	4	72	4	275	134.5	4	20	3.4	4.1	19.7
8	1	24	6	550	133	12.4	19.1	11.5	2.5	19.9
8	2	48	4	425	137	6	20	5.4	3.9	20.1
8	2.5	60	4	350	141	4.7	20	4	4.1	21.3
8	3	72	4	275	133	4	20	3.4	4.1	19.7
10	1	30	6	450	133.8	9.8	19	9	2.5	20.7
10	1.5	45	4	450	133.8	6.2	18	5.5	3.5	23.4
10	2	60	4	350	138.7	5.9	20	4.3	4	20.4

Table 4.1: Table containing the explored PMREL geometries.

2p	q	Q_s	n_{cs}	$\hat{I}_{c,max}$	$\hat{K}_{s,max}$	$T_{out,nom}$	$T_{out,max}$	ω_B	$P_{out,max}$ @ ω	$T_{out,12krpm}$
4	3	36	4	550	134.5	150.3	227.4	4740	116.7 @ 5090	68.1
4	4	48	4	425	138.5	135.2	194.6	4220	88.7 @ 4530	50.5
6	2	36	4	550	134.5	183.1	297.3	3760	122.4 @ 4300	65.7
6	2.5	45	4	450	137.5	165.2	257.3	3430	95.4 @ 3700	50.3
6	3	54	4	375	137.5	182.2	292.8	2590	81.8 @ 2860	38.9
6	4	72	4	275	134.5	191.4	324.2	2070	73.7 @ 2510	34.1
8	1	24	6	550	133	162.1	273.3	3710	115.1 @ 4680	60.7
8	2	48	4	425	137	177.5	299.4	2990	100 @ 3530	51.5
8	2.5	60	4	350	141	178.7	300.6	2420	80.8 @ 2760	37.5
8	3	72	4	275	133	169.7	290.9	2040	66.3 @ 2400	30.9
10	1	30	6	450	133.8	164.6	284.5	2830	92.3 @ 3460	47.1
10	1.5	45	4	450	133.8	176.4	309.8	2880	99.6 @ 3390	51.2
10	2	60	4	350	138.7	185.4	306.5	2160	73.3 @ 2490	34.1

Table 4.2: Results of the explored geometries

Table 4.2 presents several highlighted results. Particular attention is paid to the output torque from zero to the base speed. This torque depends on the interaction between stator and rotor geometry, in particular between the number of slots and the number of rotor barriers which are filled with ceramic ferrite magnets. The barrier in the rotor have been imposed as equal to 4, and three of them filled with ferrite magnet. The fourth barrier, which is in front of the air-gap, is only an air barrier and is needed in order to partially protect the magnets from the demagnetisation and to increase the reluctance effect. As reported in the table the maximum torques are above 300 [Nm] which are comparable with the previously examined automotive motors.

The base speed varies a lot with the different motors. It is higher when the slots number is lower because there are less series conductor that need to share the available voltage. On the whole these speeds are in many cases above 3000 [rpm] which is a considerable base speed compared with the IPM equipped whit hard magnetic materials.

Maximum output power greatly depends on the flux weakening performances. This operative region is influenced by the voltage supplied to the motor, the quantity of magnetic material inside the rotor and the number of conductor in series per phase. Since the DC bus voltage is fixed, the higher powers are developed from motors with a lower number of conductors in series per phase. This occurs particularly when q, which represents the number of slot per pole per phase, is the lowest (assuming an equal number of conductor in the slot). From these observations powers above 100 [kW] are reached also when q is equal to 2 with six and eight poles machines.

The output torque developed at 12000 [rpm] is necessary in order to understand how stable the output power is at high speeds. In particular it depends on the flux weakening capacities and the MTPV operative region. If the machine is capable of taking the maximum power at higher speeds then the torque at 12000 [rpm] will be higher. This is seen with low slots and poles where the maximum power is above 4000 [rpm] and this increases a lot the MTPV performances. Particularly if the motor is characterised by low numbers of slots and conductors in the slots, and the magnetic material inside the rotor is maximized, then the flux weakening region is very wide and the MTPV is reduced. This method allows very smooth output powers above the base speed and higher output torques at the maximum speed.

These initial performances come from machines characterised by an $L_{stk} = 100$ [mm]. This suggests that the space used for these machines was not the whole. Hence with the same stator diameters but increasing the L_{stk} the output torque will be increased due to the higher active volume. As an example the 6 pole, 72 slots motor is furthermore studied with the introduction of a longer stack. The stack length is taken up to 180 [mm] which is the imposed limit. The result is reported in table 4.3 in the second row. In the third row of the same table there is an hypothetical result obtained by taking the DC bus voltage up to 600 [V] in order to increase the base speed and the flux weakening region performances.

L_{stk}	V_{DC}	T_B	n_B	P_{max} @ ω	T_{out} & P_{out} @ 12 krpm
100	345	324	2070	73 @ 2500	34.1 [Nm] & 42 [kW]
180	345	580	1150	73.7 @ 1390	30.4 [Nm] & 38.3 [kW]
65	345	210	3200	73.3 @ 3850	39.1 [Nm] & 49.2 [kW]
180	600	580	2000	128.2 @ 2400	98.8 [Nm] & 74 [kW]

Table 4.3: 6 poles, 72 slots motor: comparison with different stack length and DC bus voltage.

Table 4.3 shows an expected linear increment of torque with the longer stack. On the contrary, as a consequence of the longer stack, there is an higher flux and the maximum voltage is reached before than in the shorter motors. This produces a shift in the base speed toward lower speeds in such a way that the output power balance is correctly maintained. At the maximum speed the longer motor has a greater drop of power caused by the fact that the base speed is lower and the flux weakening region is worsened.

The hypothetical 600 [V] DC bus is needed in order to increase the base speed value and the high speed region performance [24], [19]. This value has been taken as reference because it resembles many supplied voltages of the automotive motors previously seen in chapter 2. It allows to take the base speed from 1150 to 2000 [rpm], which has been increased in a proportional way with the bus voltage. This argumentation can be done because the machines are similar, in other words the rotor and stator geometry are the same.

Many automotive motors like Prius, Camry and Accord are characterised by shorter stack lengths, below 100 [mm] and torque below 300 [Nm]. This construction allows to move the

base point toward higher speeds. Hence the PMREL motor has been furthermore studied with a configuration in which the stack is 65 [mm] long. This configuration allows to reach higher base speeds and better flux weakening performances but reduces the maximum torque in a linear way with the stack length.
On what has been previously discussed the following types of motors can be developed considering the same DC bus characteristics:

- High L_{stk}/D_{int} ratio: this motor is suitable for application where a lot of torque is needed at low speeds. For example light truck applications.
- Low L_{stk}/D_{int} ratio: this allows to move the base point toward high speeds and increase the flux weakening performances. This is suitable for a medium size electric vehicle where is preferred a flat output power in a wide range of speeds.

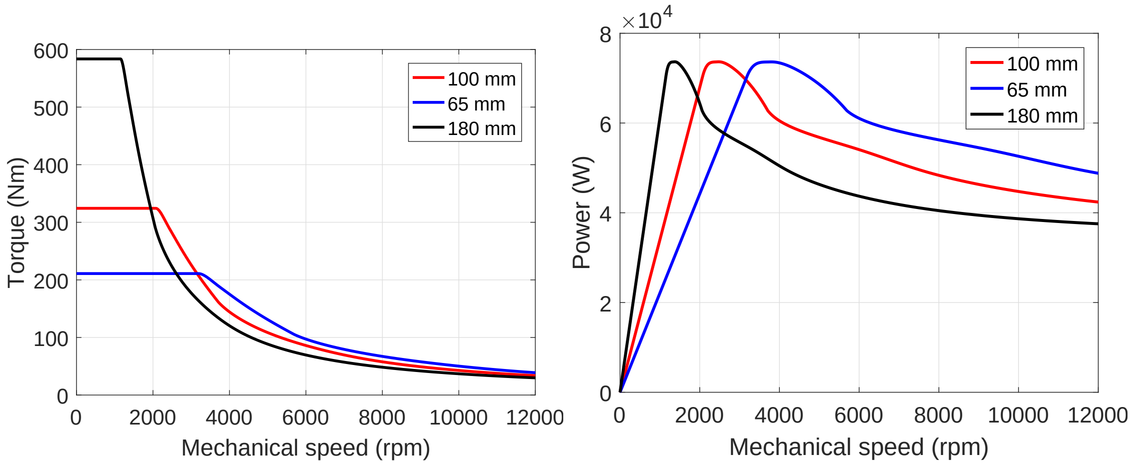

Figure 4.2: Comparison of the 72 slot, 6 poles with same electrical parameters and different stack lengths.

From these observation it is deduced that the stator must be chosen in order to satisfy the maximum torque required and the high speed behaviour.

4.2.1 Hairpin winding

This subsection focuses on the winding decided for this automotive motor.

Figure 4.3: Single hair-pin conductor.

In the table 4.1 the motors are presented with the number of series conductor in the slot n_{cs} and with possibles dimension of the conductor if the parallel path is chosen as equal to one.
The hairpin winding is constituted by a single solid conductor which has to be bended on one side and welded on the other [12].
In order to facilitate the bending process a conductor with small width or height is preferred [15]. Hence the slots characterised by a conductor larger than 6 millimetres have been chosen a number of parallel path equal to two. This allows to have a real conductor number in the slot equal for example to 8 and to decrease its height. However this will introduce more complexity in the winding shape. Following the rules in [3] the hairpin winding for the previously introduced motors have been designed.

2p	q	Q_s	n_{cs}	n_c	n_{pp}	ws	hs	wc_{new}	hc_{new}	$\hat{J}_{s,max,new}$
4	3	36	4	8	2	8.2	16.5	7.5	2	18.4
4	4	48	4	4	1	6	19	5.4	3.9	20.3
6	2	36	4	8	2	8.2	16.5	7.5	2	18.4
6	2.5	45	4	4	1	5.9	21	5.3	4.1	20.7
6	3	54	4	4	1	5.4	17.3	4.8	3.4	22.9
6	4	72	4	4	1	4	20	3.4	4.1	19.7
8	1	24	6	6	1	12.4	19.1	11.5	2.5	19.9
8	2	48	4	4	1	6	20	5.4	3.9	20.1
8	2.5	60	4	4	1	4.7	20	4	4.1	21.3
8	3	72	4	4	1	4	20	3.4	4.1	19.7
10	1	30	6	6	1	9.8	19	9	2.5	20.7
10	1.5	45	4	4	1	6.2	18	5.5	3.5	23.4
10	2	60	4	4	1	5.9	20	4.3	4	20.4

Table 4.4: Table containing the main parameters for the hair-pin winding construction.

In the table 4.4 different types of winding are presented. They change on the basis of the number of slot and conductor in slot. The new hypothesised winding with 2 parallel path are highlighted. These windings are characterised by a different building scheme as presented in figure 4.4.

From the winding point of view, stators that are characterised by low number of conductor in slot with small width and height of the elementary conductor have a building advantage with respect the others. If these observations are taken into account stators with more than 36 slot are the possible solutions (highlighted in table 4.1). This first choice excludes motors with the highest base speed, which are at the same time the ones with the highest maximum power. The only motor which is not included in this exclusion, is the 36 slots 6 poles because it has the highest output power. For this motor the winding will be reshaped following table 4.4 in order to reduce the conductor height.

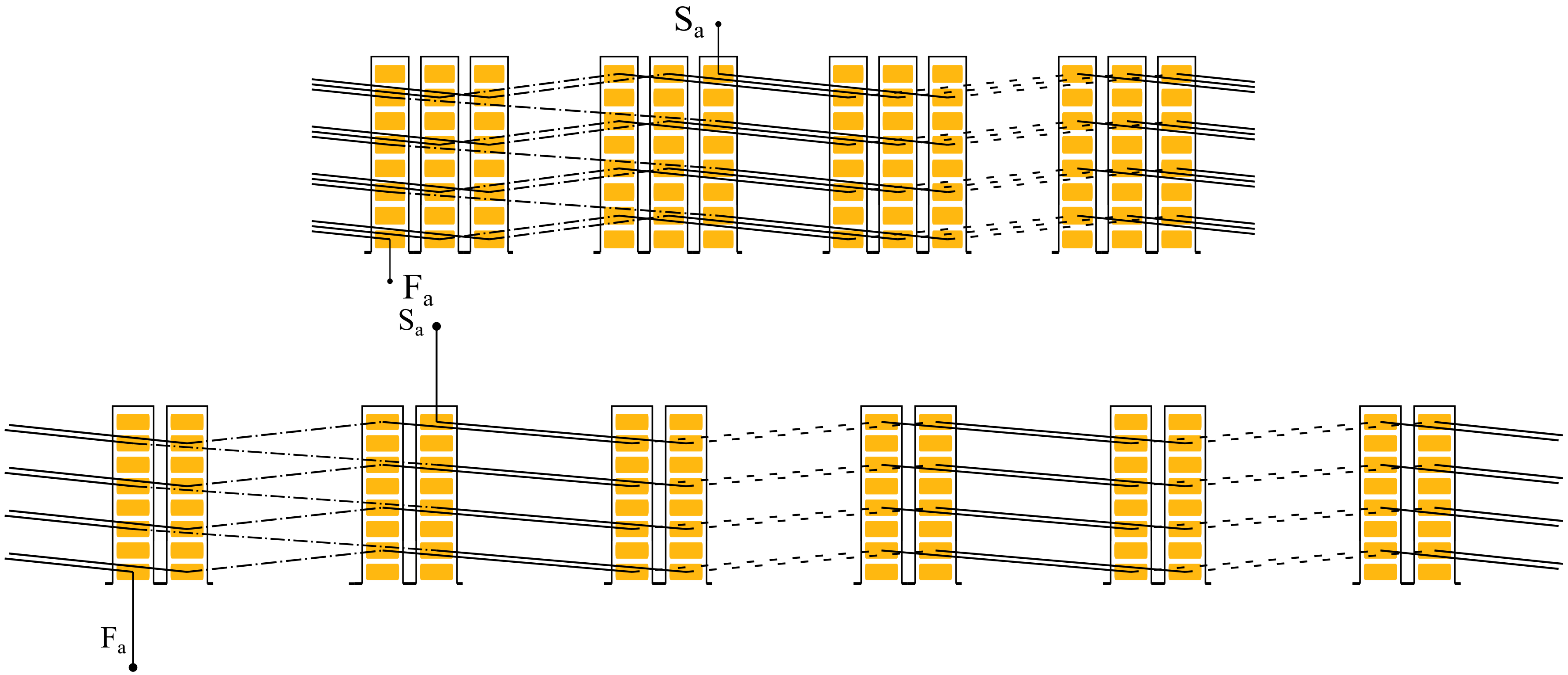

Figure 4.4: Examples of hairpin conductor scheme for a 4 pole, 3 slot per pole per phase motor (above), and for a 6 pole 2 slots per pole per phase (below). These are the winding highlighted in table 4.4 characterized by $n_c = 8$.

4.2.2 Magnet protection from demagnetisation

In PMREL motors there are Ceramic Ferrite magnets. These are characterised by low coercive magnetic field and low air-gap flux density. This implies that, when a high current is imposed in front of them, it can reduce the coercive magnetic field up to permanently demagnetise the magnet. This is a condition that has to be avoided in a PM motor. In order to verify magnetic fluxes inside the machine a test in which the current is imposed maximum on -q axis and zero on d axis is carried out for each motor. The residual magnetic flux inside the magnet has to be higher then the safety one [5]. The magnets equipped in the machines are all Ceramic 8 type, characterised by $H_c = 233$ [kA/m] and $\mu_r = 1.43$. The safety residual induction is fixed in 0.1 [T] for this typology of magnet. This value is respected by those machines where the number of poles combined with number of slot is higher. This occurs because more poles help reduce the flux and with more slots the total current inside the slot is lower. Motors which pass this test are in this particular case the ones with number of slots above 54. Motors with lower number of slots have to be modified with the insertion of larger magnets or will be studied in the pure reluctance configuration in the next chapter.

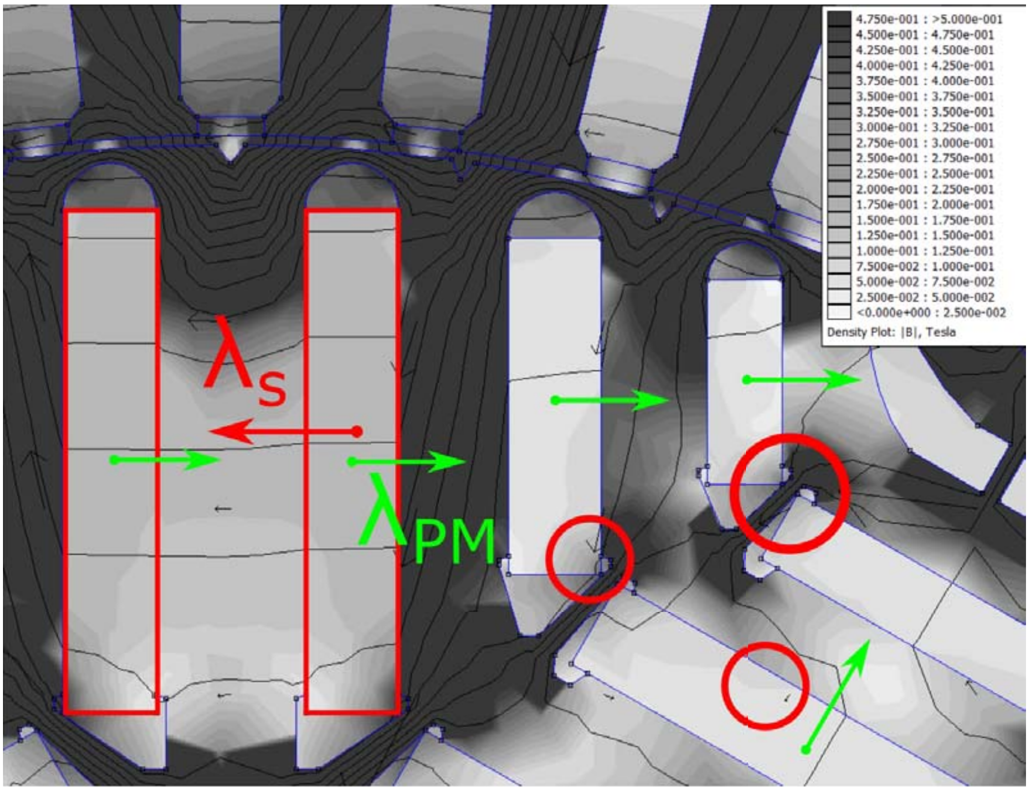

Figure 4.5: Example of de-magnetised magnet in the test with maximum current on the -q axis.

Figure 4.5 offers an example of demagnetisation. Usually the magnets that suffer from this problem are the ones positioned nearest the air-gap. However, this figure shows that, where the iron links are heavily saturated, there are flux lines which pass through the magnets and cause a reduction of magnetic field inside the magnet itself and a permanently demagnetisation.

4.2.3 PMREL motor choice

In tables 4.2 there are the main performances of the analysed PMREL motors. From the output torque's point of view the best ones are the 6 poles 72 slots, and the 10 poles with 45 and 60 slots. These motors are also the ones with lower base speed, a very important parameters and term of comparison between the automotive motors that are used nowadays. The ones with the higher base speed are the same which suffer from demagnetisation as stated in 4.2.2. Hence these machines will be developed as pure reluctance in the next chapter. Table 4.5 groups the motors that are not interested in the demagnetisation.

2p	q	Q_s	n_{cs}	$\hat{I}_{c,max}$	$\hat{K}_{s,max}$	$T_{out,nom}$	$T_{out,max}$	ω_B	$P_{out,max}$ @ ω
6	3	54	4	375	137.5	182.2	292.8	2590	81.8 @ 2860
6	4	72	4	275	134.5	191.4	324.2	2070	73.7 @ 2510
8	2.5	60	4	350	141	178.7	300.6	2420	80.8 @ 2760
8	3	72	4	275	133	169.7	290.9	2040	66.3 @ 2400
10	2	60	4	350	138.7	185.4	306.5	2160	73.3 @ 2490

Table 4.5: Motors which passed the demagnetisation test.

These motors are characterised by the lowest currents in the slots and the smallest conductors. This leads to less flux density that tents to demagnetise the Ferrite magnets. The lower current will also produce less Joule losses with temperature benefits. On the other hand these motors have a lower base point speed which is a drawback compared with modern IPM motors applied in automotive. In order to increase this base speed two strategies can be adopted:

- Increase the DC bus voltage
- Reduce the motor stack length

From the stack length reduction the available DC bus voltage is reached at higher speeds because the flux in the machine is lower. The downside of this choice is that the output torque is reduced in a linear way with the stack length. The preferable way is when the DC bus voltage is increased, for example with Boost converter. This leads to higher available voltages but the current taken from the conductors must be reduced if the power is left unchanged. The current does not represent to be a problem, because when the number of slot is increased, the current has to decrease in order to maintain the same electrical loading in the machine as it can be noted in tables 4.2 and 4.5. The main problem with a boost converter is that it increases the complexity in the supply circuit and then the costs will be higher. This choice has been made by the majority of the electric vehicle producers over these last years even because a power-train capable of energetic recovery is needed.

The simulation' results of the motors in table 4.5 are presented below. In order to be compared with IPM automotive motors the power and torque densities have to be evaluated. From table 4.6 it can be noticed that the PMREL external volume does not change because the diameter is imposed but the internal volume slightly increases because the air-gap diameter was adapted to the number of poles. Hence 8 and 10 poles machine have a roughly higher internal volume compared with the 6 poles motor. Finally PM Assisted Reluctance motors are compared in terms of dimensions and performances with automotive motors of chapters two and there.

2p	Q_s	L_{stk}	Vol_{int}	Vol_{ext}	$\hat{K}_{s,max}$	$T_{out,nom}$	$T_{out,max}$	ω_B	$P_{out,max}$ @ ω
6	54	104	2.65	5.35	137.5	182.2	292.8	2590	81.8 @ 2860
6	72	104	2.65	5.35	134.5	191.4	324.2	2070	73.7 @ 2500
6	72	180	4.58	9.26	134.5	169.7	580	1150	73.7 @ 1390
6	72	68	1.73	3.49	134.5	169.7	210	3200	73.7 @ 3850
8	60	104	2.70	5.35	141	178.7	300.6	2420	80.8 @ 2760
8	72	104	2.70	5.35	133	169.7	290.9	2040	66.3 @ 2400
10	60	104	2.79	5.35	138.7	185.4	306.5	2160	73.3 @ 2490
Prius 10	48	50.8	1.05	2.78	250.7	120	207	2800	60 @ 3600
Lexus	48	135.4	1.82	4.25	157.9	180	300	5000	165 @ >6000
BMW i3	72	132.2	3.36	6.08	87.6	150	250	4775	125 @ 4775

Table 4.6: Output performances of the chosen PMREL compared with three IPM automotive motors presented in chapter three.

Power and torque densities computation is carried out from the values in table 4.6, and is reported below in table 4.7:

Model poles & slots	T_{max}/Vol_{int} $[Nm/l]$	T_{max}/Vol_{ext} $[Nm/l]$	$P_{out,max}/Vol_{int}$ $[kW/l]$	$P_{out,max}/Vol_{ext}$ $[kW/l]$
6 & 54 (104 mm)	110.5	54.7	30.9	15.3
6 & 72 (104 mm)	122.4	60.6	27.8	13.8
6 & 72 (180 mm)	123.9	62.6	16.1	8
6 & 72 (68 mm)	115.4	60.2	42.6	21.1
8 & 60 (104 mm)	111.3	56.2	29.9	15.1
8 & 72 (104 mm)	107.7	54.4	24.6	12.4
10 & 60 (104 mm)	109.9	57.3	26.3	13.7
Prius 10	197.1	74.5	57.1	21.6
Lexus 600	164.8	70.6	94.5	41.6
LEAF	137.3	59.1	39.2	16.9
BMW i3	74.4	41.1	37.2	20.6

Table 4.7: Power and torque densities comparison: PMREL vs different type of automotive motors.

These two tables clearly show how the IPM motor is better than a PMREL equipped with Ferrite magnets. This, as explained in chapter three as well, is due to two several reasons [28]. The first thing that needs attention is that NdFeB magnets have an higher flux density which is the main advantage of these magnets. Firstly, this characteristic produces a higher output torque considering the same machine volume because magnet's flux appears directly in the torque equation. Secondly, the higher flux allows to reach higher electrical loadings in order to obtain the peak torque from the motor. This happens because magnets are not demagnetised when the current is imposed at its maximum with contrary direction on the magnet axis. This is the main cause that limits the Ferrite assisted motor regarding the electrical loading. Hence passing from NdFeB to ceramic-ferrite magnets causes two main limitations to the machine: torque density reduction and possible demagnetisation. In regards to the second problem the electrical loading must be limited and this causes a reduction in the peak torque and power values of the motor. In order to comply with those limits the Ferrite magnets machine must have a larger volume with a lower electrical loading.

Another important aspect is the number of poles in the machine. In a low pole motor, for example the 2 and 4 poles there is an higher flux in the machine and this means that the back-iron must be larger in order to receive that flux without increasing the back-iron saturation too much. This causes a lower air-gap diameter considering the output diameter unchanged, and a reduction of the available torque. This observation can be applied to every electrical machine and, as seen in chapter two, the studied automotive motors have all at least 8 poles. The drawback in the poles increment is that the supply frequency is higher and causes more iron losses and inverter electronic components are more expensive. Hence the number of poles has to be limited because when speeds are in the order of 10 [krpm], having for instance 12 poles causes the frequency enters in the [kHz] range. This causes complexity in the inverter and in its costs but also causes difficulties in the machine control if sensorless controllers are taken into account.

From table 4.7 the torque and power densities can be observed. It can be noticed that due to both the lower electrical loading both the lower Ferrite magnets performance, the torque density with respect the internal volume is very low compared with Prius and Lexus models. This comparison presents a torque density of PMREL in the range of the 60% of the Lexus and Prius motors. It is different for LEAF and BMW models, with the developed PMRELs that have almost the LEAF performance and overcome BMW by a 50%. This results in thinking of those two automotive motors as more balanced regarding the rated over peak performance ratio. In particular it is known that BMW motor can sustain 75 [kW] for half an hour and its maximum power for less than a minute [25], [27], [9]. Lexus model is capable of its maximum peak power just for 12 seconds due to its too high electric loading [8]. Hence PMREL motors thermal capability will be analysed and compared in the following section.

Power densities of PMREL motors vary in the range from 16 to 42 [kW/l]. Without considering the ones with different stack length, motors 100 [mm] long are in the range of 25 - 30 [kW/l]. This is a lot lower than Lexus and Prius model: in particular it is less than a third with respect Lexus model, and less than a half with respect Prius power density. This confirms the fact that those motors are characterised by very high peak values sustainable for a few seconds.

By focusing now on the 68 [mm] stack long motor it can be noticed that its torque density is higher than the BMW one and the power density is almost the same. This is produced from the different stack length which helps reduce the volume and takes the same peak power to higher speeds. Hence a higher power density is achieved with an almost equal torque density. These observations give the following results:

- The Ferrite assisted reluctance motor cannot reach the same electrical loading of a same dimension IPM.

- PMREL maximum torque is reduced by the lower electrical loading and magnet flux density.

- Torque in the order of the Lexus IPM torque are reached with a larger volume (46 % higher).
- Torque densities are in the order of the LEAF IPM motor.
- Power densities in most cases are much lower than the IPM ones.
- The power is limited in the flux weakening region due the Ferrite magnets lower performance with-respect NdFeB magnets.

On the whole, despite the general worsening in the performances with respect the same dimension IPM machine, these PMREL reach torques and powers suitable with an automotive application. In particular it is noticeable in table 4.6 that the volumes are similar to the BMW i3 motor. Furthermore torques are higher than the BMW one although at a lower speed. The PMRELs maximum powers are higher than the Prius one at similar speeds. Hence this type of motor is suitable for an hybrid vehicle where it can be used for optimizing the ICE and also to directly power the vehicle. If the stack length is reduced up to 40 [mm] then another type of motor can be introduced. This motor could be used as "start & stop" system like in the first types of electric vehicles [24], [23].

4.2.4 Cost reduction with respect an IPM

One advantage of Ferrite magnets is their lower cost with-respect rare earth magnets. Prices range and specific weights are reported below:

- NdFeB: Price $\cong$ 60-80 [$euro/kg$], weight = 7500 [kg/m^3]
- Ferrite: Price $\cong$ 7 [$euro/kg$], weight = 4900 [kg/m^3]
- Copper: Price $\cong$ 7 [$euro/kg$], weight = 8900 [kg/m^3]
- Iron: Price $\cong$ 1 [$euro/kg$], weight = 7800 [kg/m^3]

As shown the NdFeB magnets are ten times more expensive with respect Ferrite magnets. This section compares the weights and costs of IPM motors that were presented in chapter three as well as the previously developed PMREL.

Model -	Type -	PM Volume [m^3]	PM weight [kg]	PM price *euro*
BMW i3	IPM	$3.427 \cdot 10^{-4}$	2.57	160-205
Lexus	IPM	$1.854 \cdot 10^{-4}$	1.4	85-110
Prius 10	IPM	$1.04 \cdot 10^{-4}$	0.78	50-63
Accord M	IPM	$1.643 \cdot 10^{-4}$	1.24	75-100
LEAF	IPM	$2.511 \cdot 10^{-4}$	1.88	110-150
6 poles 72 slots	PMREL	$5.811 \cdot 10^{-4}$	2.85	20
8 poles 72 slots	PMREL	$6.504 \cdot 10^{-4}$	3.19	22.3
10 poles 60 slots	PMREL	$5.414 \cdot 10^{-4}$	2.65	18.6

Table 4.8: Magnets prices comparison for IPM and PMREL motors previously introduced.

From table 4.9 it is visible how the final machine price depends from the NdFeB magnets. In an IPM there is a percentage of PM price of about 60 - 70% on the total cost. Magnet

Model -	Iron mass $[kg]$	Copper mass $[kg]$	PM mass $[kg]$	Iron price *euro*	Copper price *euro*	PM price *euro*	Total price *euro*
BMW i3	26.3	4.6	2.57	29	33	160 - 205	222 - 266
Lexus	24.8	3.6	1.4	27	25	85 - 110	137 - 162
Prius 10	16.7	5.2	0.78	18	36	50 - 63	104 - 117
Accord M	21.4	6.3	1.24	24	44	75 - 100	143 - 168
LEAF	27.1	3.9	1.88	30	27	110 - 150	167 - 207
6p, 72 slot 100 mm	25.0	9.4	2.85	27	66	20	113
8p, 72 slot 100 mm	23.4	8.3	3.19	26	58	22	106
10p, 60 slot 100 mm	24.2	7.2	2.65	27	50	19	96

Table 4.9: Total price comparison between analysed IPM and proposed PMREL.

prices are then influenced by the market behaviour which can present high variations during short time periods. This is a plus point for the PMREL machine where the Ferrite magnets have less influence on the final cost. The highest costs in a PMREL machine are related to the copper quantity.
It is important to notice that PMREL motors end up being a lot cheaper alternatives to the IPM motor, but the price gap between PMREL and IPM has to be evaluated considering also the performance gap. For example the three presented PMREL are characterised by an output power similar to the Prius motor but the torque is about 300 [Nm] which is 50% higher then the Prius maximum torque. In order to equalize the Prius 2010 output torque the stack length must be reduced to 65 [mm] and this means to reduce the iron and copper prices in a linear way. This comparison will be later reported.

Model -	Price *euro*	$T_{out,max}$ $[Nm]$	ω_B $[rpm]$	$P_{out,max}$ @ ω $[kW]$ @ $[rpm]$	P_{out} @ 10000 rpm $[kW]$
Prius 10	104 - 117	207	2800	60 @ 3600	50
LEAF	167 - 207	280	2100	80 @ 5500	78
6p, 72 slot 100 mm	113	324	2070	73.7 @ 2500	46
6p, 72 slot 65 mm	88	210	3200	73.7 @ 3850	53
8p, 72 slot 100 mm	106	291	2040	66.3 @ 2400	40
8p, 72 slot 65 mm	74	190	3135	66.3 @ 3750	45
10p, 60 slot 100 mm	96	306	2160	73.3 @ 2490	44
10p, 60 slot 65 mm	71	200	3300	73.3 @ 3820	50

Table 4.10: IPM vs PMREL comparison: many parameters are in favour of the PMREL typology.

In table 4.10 the PMREL motor is proved to be a valid alternative to the IPM motors if the following assumption are taken into account:

- Cost saving due to lower price of the Ferrite magnets. This allows to build wider or longer machines in order to take the torque at same levels of the IPM motors.
- From table 4.9 it is noticeable that the iron mass of the three PMREL motors is almost 50 percent higher than the Prius iron mass and are in the range of others

IPM that develop more power. This means that in order to have the same output performances the PMREL machine will be wider an heavier, which are disadvantages in an automotive application.

- From table 4.10 the PMREL have the IPM characteristics until the base point is reached. After that speed the torque in flux weakening shows a rapid drop and the output power at 10 [krpm] is better for the IPM.

- LEAF motor has almost the same iron quantity of the PMREL analysed but allows a better flux weakening operation. This is caused by the NdFeB magnets which have higher flux density than the Ferrite ones. In order to fill the gap at high speeds the Ferrite quantity has to be increased or the base point has to be taken at higher speeds.

Thanks to this, it is possible to say that when it comes to the cost saving, the PMREL motor is suitable for an automotive application, although it should be larger and heavier than a IPM motor in order to have considerable performances. This means that the PMREL fits better in application where the required power density is not so high for example in a Prius like vehicle.
In regards to the torque point of view PMREL motor allows to reach high torque densities but at lower speeds with-respect an IPM, hence it must be wider and shorter in order to have the same IPM's base speed, or a DC bus higher voltage must be introduced. Hence this motor is suitable for truck applications as well.

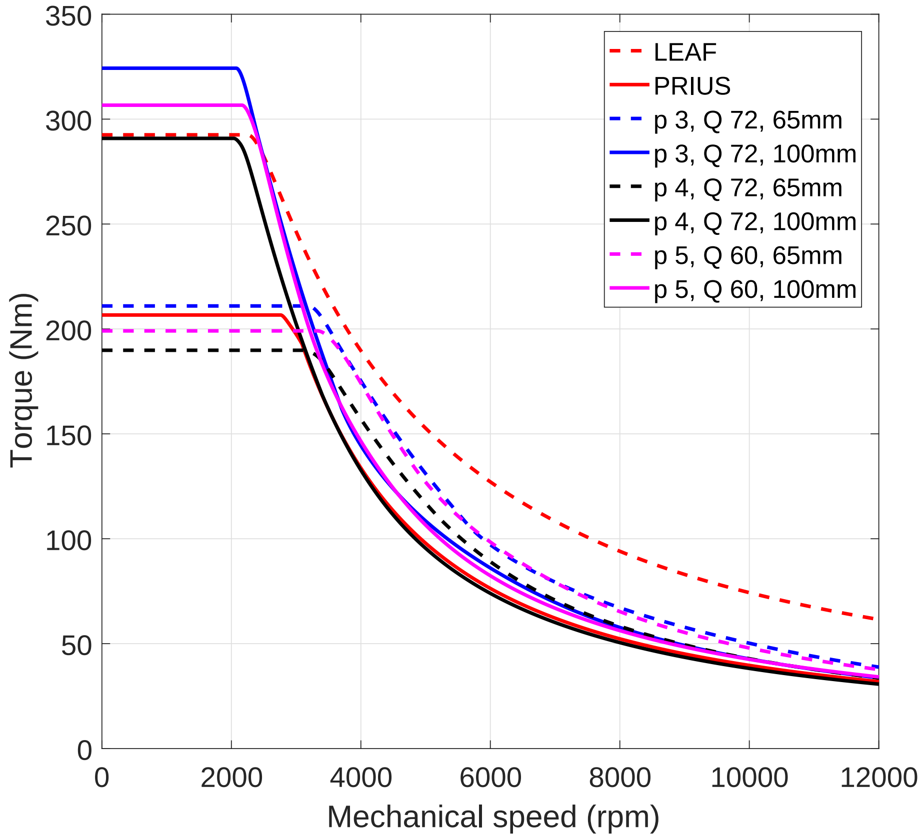

Figure 4.6: PMREL and IPM comparison: torque vs speed behaviour is comparable with Prius and Leaf IPM motors.

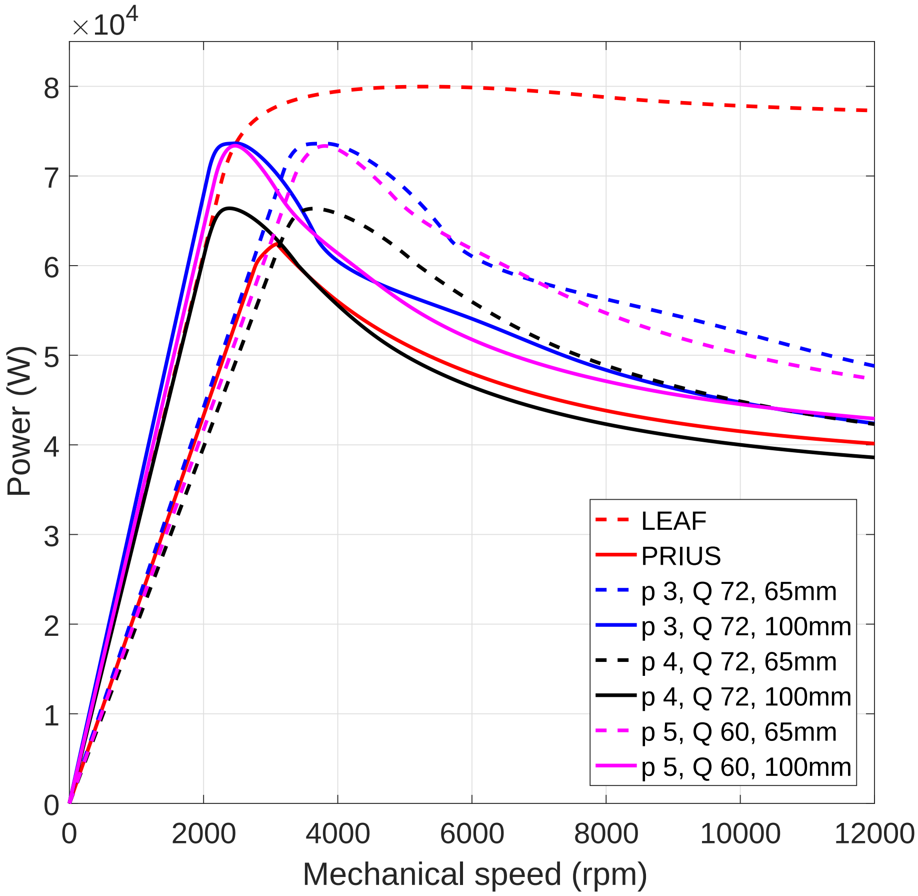

Figure 4.7: PMREL and IPM comparison: power vs speed behaviour is better than the Prius IPM model.

Figures 4.6 and 4.7 show the observations that have been mentioned in the previous chapter. It is noticeable that PMREL machines have the same maximum power and torque behaviour of the Prius motor reminding that the designed PMREL with 65 [mm] stack have 26% higher outer volume but almost the same iron weight (because of more "holes" in the PMREL used to create the barriers). The most important thigh is that, despite the higher volume, 65 [mm] long PMREL machines have lower costs in comparison to Prius motor (in the range of 61 to 84 % of the Prius cost).
The last parameter that was not considered above is the power factor. It can be stated here that due to the lower electrical loading and due to the presence of magnetic material in the PMREL machine, the saturation at the maximum required power is lower with-respect Prius, Lexus and other models, and this allows to reach PF in the MTPA condition above 0.8. In the rated load conditions PF is above 0.9 for the most of PMREL motors.

4.3 Thermal analysis of PMREL motor

In the previous subsection the final PMREL motors chosen are presented. The thermal analysis of those models is carried out in the following passages [1], [7]:

- Losses computation in the worst case
- Outer water cooling system definition

- Thermal simulation through Simulink and Mirage

4.3.1 PMREL thermal analysis

The cooling system is water/glycol type and it has been chosen following the example of others automotive motors. The system is constituted by an external case with spiral type channels in which the cooling fluid flows. This system is necessary in order to take out the amount of losses produced by the motors so that it allows to reach higher electrical loadings, i.e. higher currents in the motor's slots. In order to have a safety factor in the thermal analysis, the end winding losses have been introduced in the active volume. The cooling system is the same for each type of motor. Here is presented the one for motors with a stack length of 100 millimetres.

- outer case material: inox steel
- number of channels: 5
- channel width: 15 [mm]
- channel height: 10 [mm]

These values allow to reach Reynold coefficient in the cooling channel above 10000, hence turbulent type of motion in the fluid is reached in the fluid together with a thermal conductivity coefficient in the order of 12000 $[W/m^2 \cdot K]$. This value will be set equal for all the studied geometries. All the motors present maximum power losses slightly above the base speed, i.e. in the flux weakening region. This happens because the current is at its maximum and so are the Joule losses, and the speed is high enough to produce elevated iron losses due to the iron saturation and the frequency reached. After the flux weakening region the motor enters in MTPV operations in which the current is reduced and this allows to reduce the Joule losses and reduces the flux density in the iron. This means that from the losses point of view, the flux weakening region is the worst operative one, hence the losses chosen in order to carry out thermal simulation are these one reported in the table 4.11 and rated losses in table 4.12.

The hairpin windings need to be considered in the losses' evaluation, due to their large section, suffer from additional losses in the conductors. These losses are produced by skin effect and are negligible when the usual filament winding is equipped in the machine [3]. These additional losses are higher with lower number of conductors of elevated height, which is precisely the case of high number of slot stators. Hence the Joule losses have to be increased in order for these additional losses to be considered [3], [12].

2p	q	Q_s	n_{cs}	$\hat{I}_{c,max}$	$\hat{K}_{s,max}$	P_{Joule}	P_{Iron}
6	3	54	4	375	137.5	6050	780
6	4	72	4	275	134.5	5100	550
8	2.5	60	4	350	141	5000	1050
8	3	72	4	275	133	4300	700
10	2	60	4	350	138.7	4400	1100

Table 4.11: Losses in the worst point for the motors presented in the previous section.

2p	q	Q_s	n_{cs}	$\hat{I}_{c,nom}$	$\hat{K}_{s,nom}$	P_{Joule}	P_{Iron}
6	3	54	4	225	82.5	2200	450
6	4	72	4	165	80.7	1840	320
8	2.5	60	4	210	84.6	1800	600
8	3	72	4	165	79.8	1550	400
10	2	60	4	210	83.2	1590	630

Table 4.12: Losses at rated loads for the motors presented in the previous section.

Tables 4.11 and 4.12 shows the losses in the worst case (transient operations) and at the rated conditions. These values are needed in order to set the thermal simulation by means of Simulink. From the maximum losses in the machine can be defined the transient period of time for which the maximum power can be sustained. From the rated losses the temperature in the nominal conditions of the machine can be evaluated. This temperature must stay under the winding insulation class specified maximum temperature. Following the rules for a typical winding, the F class is chosen as insulation class and the related over-temperature allowed is equal to 155 [K] [7]. All the following thermal simulations have been done using the same outer case with the same amount of water/glycol cooling fluid.

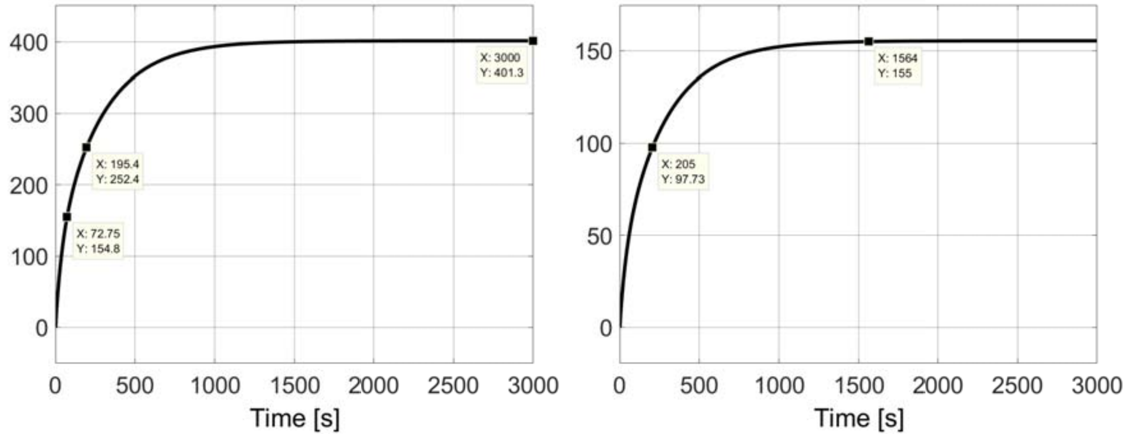

Figure 4.8: 6 poles 54 slots model thermal simulation: on the left at the maximum loading and on the right at rated load.

In figure 4.8 the temperature increments are presented. These first two figures regard the 6 poles 54 slots motor. Its temperature reaches the imposed limit when the rated load losses are injected in the model. This means that the output rated power can be sustained for long periods of time, theoretically for an infinite time. When the maximum losses are imposed as input in the thermal simulation, the winding temperature reaches a steady state temperature that is too high for the insulation performances. Hence in this case the maximum output power is guaranteed for a limited time which is equal to 72 seconds. As previously explained this time is higher than the studied automotive' where the maximum power was guaranteed for 15 - 30 seconds [9]. This fact happens because the developed PMREL motor have a lower electrical loading and this helps reduce the losses at the maximum power.

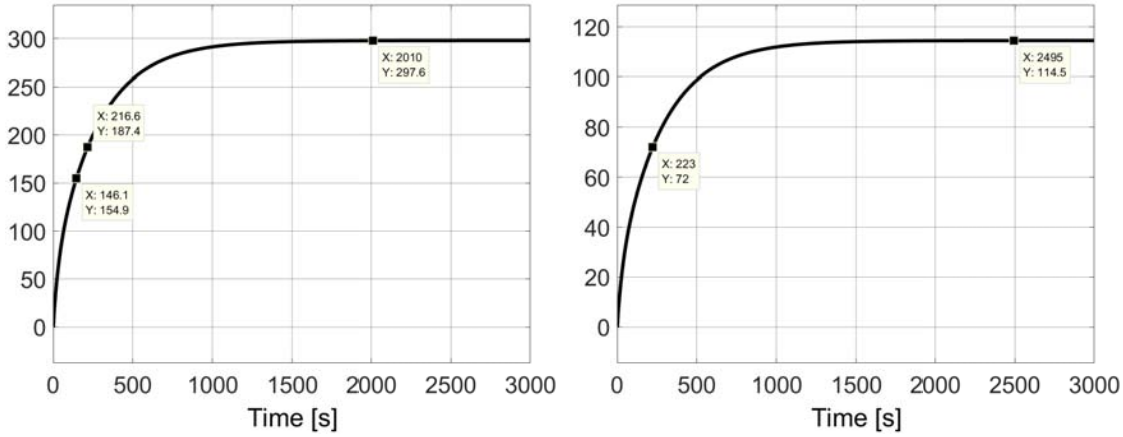

Figure 4.9: Thermal simulation of the 6 poles 72 slots model: on the left at the maximum loading and on the right at rated load.

In figure 4.9 temperature increments of the 6 poles 72 slots are reported. It can be noticed a great decrement of the steady state temperature with respect the previous model. This is due both because of the lower Joule losses that affect the motor and because of the cooling system which is the same. This helps also in the transient peak power that, as shown in the figure on the left, can be sustained for a longer time (for about 146 seconds). Hence this motor can be cooled by a lower amount of cooling fluid or can be electrically charged for a longer time.

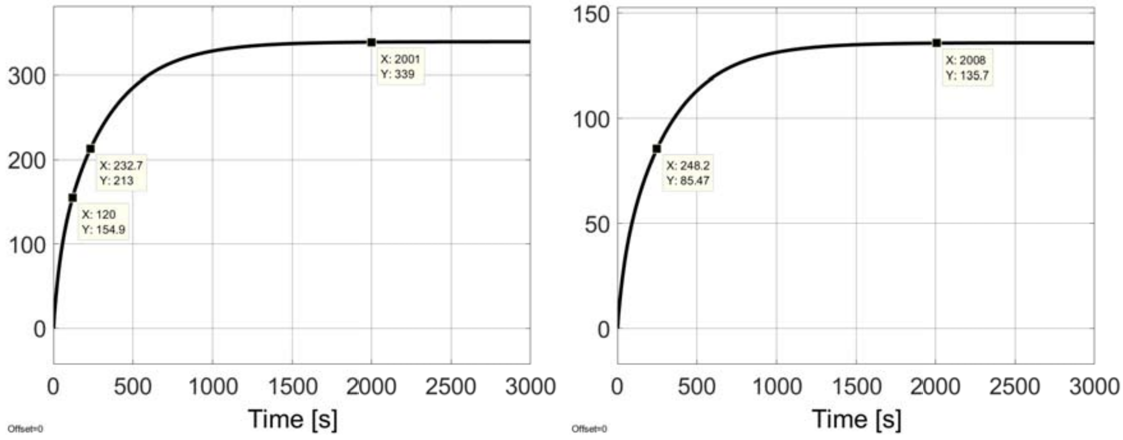

Figure 4.10: Thermal simulation of the 8 poles 60 slots model: on the left at the maximum loading and on the right at rated load.

In figure 4.10 the results regard the 8 poles 60 slots motor. At rated load (right) the losses take the steady state temperature again below the temperature limit and this happens also with the 8 poles 72 slots in figure 4.11 and the 10 poles 60 slot in figure 4.12. Hence for these models the cooling system can be reduced in size or a simpler one can be considered leading to costs advantages on the whole power-train system.
The transient peak losses produce a winding temperature in every case above 250 [K] but the 8 poles 72 slot is the better one because it is characterised by the lower losses and then the maximum peak power can be sustained for about 240 seconds.

The 8 poles 60 slots motor reach the maximum winding temperature in 120 seconds and the 10 poles 60 slots takes 150 seconds. These motors compared with the real automotive motors have a peak power duration which is 10 times higher. Hence this motor's peak power can be maintained for longer and this is an advantage for particular cases.

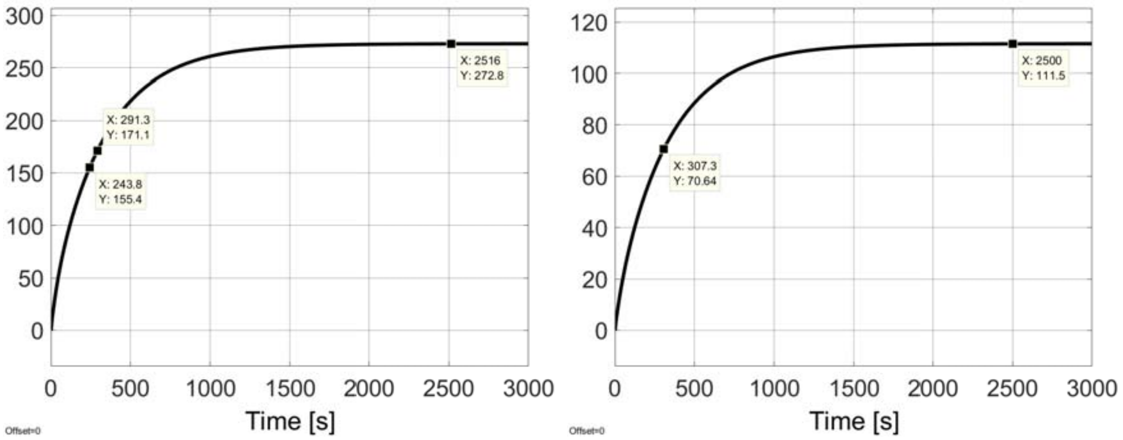

Figure 4.11: Thermal simulation of the 8 poles 72 slots model: on the left at the maximum loading and on the right at rated load.

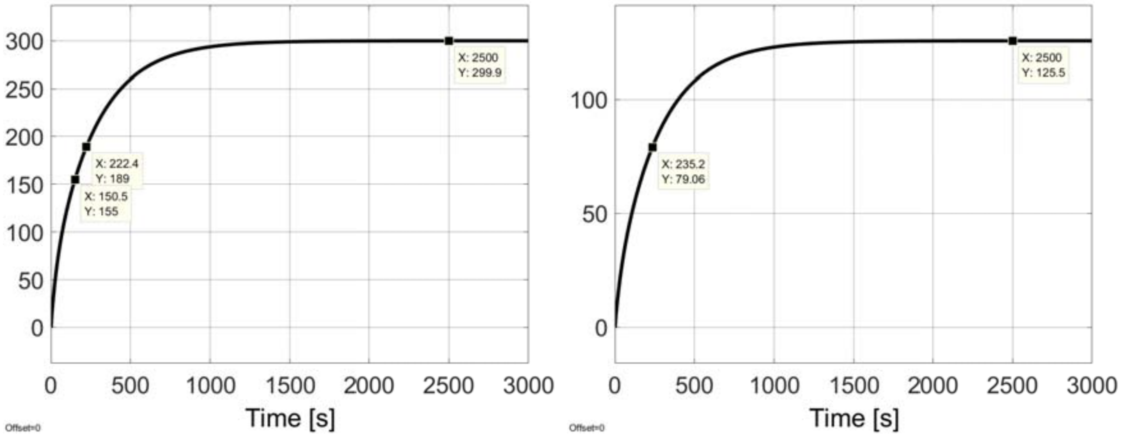

Figure 4.12: Thermal simulation of the 10 poles 60 slots model: on the left at the maximum loading and on the right at rated load.

The previous figures present both the points where the temperature reaches its maximum and where it reaches 63% of the maximum value. This is done in order to understand the motor thermal constant. This value is in the range of 220 - 300 seconds depending on the geometry differences.
In order to validate the Simulink thermal result the PMREL geometries have been also simulated in a thermal FEMM. This type of simulation is carried out by imposing all the Joule losses in the slots, assuming that the end-winding heat flows through the copper and is extracted by the cooling system. A safety coefficient has been introduced so that the hairpin additional losses can still be considered following [14] and [3]. The slot has been represented by the right number of conductors with the insulation layers of 0.1 millimetres similar to [16]. Iron losses have been split in tooth and back-iron losses and imposed to each iron region. The simulation results relative to the 6 poles 72 slots motors are presented below.

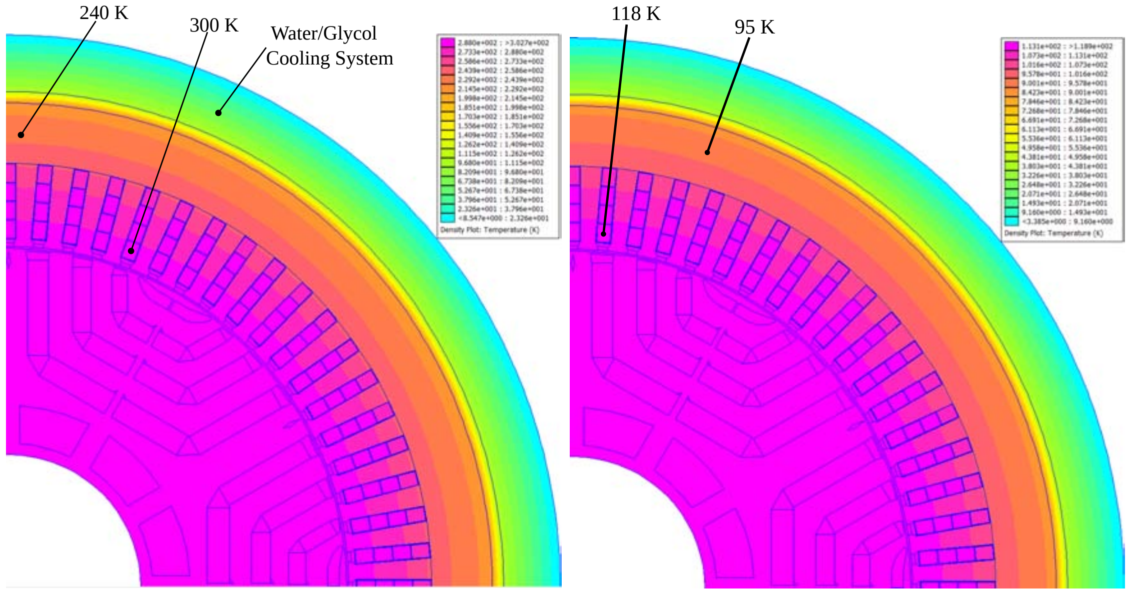

Figure 4.13: Overheating in [K] degrees in the 6 poles 72 slots motor. On the left there are temperatures relative to an hypothetical steady state at the maximum power, on the right there are temperatures at rated load. These temperatures have to be compared with the one in figure 4.9.

In the figure 4.13 the temperature distribution is presented. It is noticeable that the evinced temperatures in the slots are very similar to the steady state ones evaluated from Simulink and this is a validity index of the Simulink model.

4.3.2 Automotive thermal analysis considerations

In the previous subsection PMREL thermal analysis are presented and it can be noticed that, at their rated loadings, they do not reach the maximum insulation class temperature in many cases. This means that the cooling system can be reduced in size leading to further cost savings. This fact is allowed by their reduced electrical loading with respect the previously examined automotive motors. However there are IPM motors with a lower electrical loading, like the cases of BMW i3 and Nissan Leaf [25], [29]. As previously explained these two motors are characterised by a lower loading because of the main differences in the vehicle in which they are equipped. Indeed these two vehicles are the only ones in the analysed group that are pure electric vehicles. This is a substantial difference in the motor usage because, in a pure electric vehicle, the motor needs to guarantee the rated power for a longer time with respect the one in hybrid vehicle. Hence the thermal behaviour will be different in the two typologies of vehicle.
An example of these two behaviours is given in the declared performances of the BMW i3 and the Lexus motors. In the Lexus model the maximum power is guaranteed for 12 seconds, which is a sufficient time to help the ICE in the speed range from zero to 100 [km/h]. This means that the IPM motor is needed in order to provide peak powers during accelerations to preserve the optimal exploitation of the ICE. On the contrary in the BMW i3 vehicle the motor has to guarantee the rated power of 75 [kW] for 30 minutes. Hence in order to guarantee this thermal behaviour the electrical loading is a lot lower than the

Lexus one (BMW has 87 [kA/m] and Lexus has 157 [kA/m]).
BMW model guarantees 75 [kW] for 30 minutes because this value is influenced by the vehicle maximum range [25]. In order to explain this the following producer data are taken into account:

- i3 maximum speed limited at 150 [km/h]
- maximum range of 150 [km] (without range extender)

It is a reasonable assumption to have 150 [km/h] when the motor develops 125 [kW]. At the rated power of 75 [kW] an infinite number of speeds are possible but a medium one can be chosen in the range of 80 - 100 [km/h]. Assuming 90 [km/h] as rated speed then the maximum range allowed from the batteries is covered in about 1.6 hours. If the total distance is divided in half assuming the same route for the round-trip hence the rated performance of the motor has a duration of 0.8 hours (48 minutes). This range is in the motor possibilities taking into account that the utilisation of this vehicle is mainly as city car and its usage at high speeds (like extra-urban driveways) is limited by the batteries maximum range. This explains why the motor has that power guaranteed for half an hour which is totally different from the peak power performance declared in the Lexus model.

4.4 Conclusion

This chapter has compared automotive IPMs and the designed PMRELs so that come conclusion have been drawn.
The first one is on the PMREL machines volumes. It has been demonstrated that their volume has to be higher with-respect an IPM machine characterised by the same output torque. This is caused by the lower energetic content of Ferrite with-respect rare earth magnets. An higher volume causes many drawbacks in an electric vehicle application. The most important ones are the heavier motor embedded in the vehicle and the higher volume required by the whole system.
An hypothetical PMREL automotive motor is characterised by good performances until the base point is reached. This fact puts in evidence that in order to increase the competitiveness of this motor typology the base point of the machine has to be brought at the highest possible speed. This makes it possible to understand why the DC bus voltage on today's vehicles have been increased up to 700 [V] in the last years. Another important parameter that influences the base speed is the L/D ratio. In particular an automotive machine has to be designed with a low L/D ratio in order to have shorter single conductors in such a way to reduce the induced voltage and exploit the DC bus at its best. Another design aspect is relative to the number of slots. With many slots the slot width is lower allowing to equip smaller hairpin conductors. This helps reduce the space required to bend them and optimize the end-winding space.
After the base point the flux weakening region starts. In order to avoid a too short FW speed range the machine has to be characterised by a lower electrical loading. This offers many advantages which involve the power factor, the thermal behaviour, the iron saturation and the demagnetisation of the ferrite magnets. Indeed with a limited electrical loading the machine does not reach elevated saturation values as seen in chapter two for the different automotive motors. This fact helps reduce the MTPA maximum angle and allows a wider angular range for flux weakening region which can reach higher speeds and reduce the MTPV operations. This is necessary because when MTPV is reached there is a sudden drop in the developed output torque.

The power factor is maintained at higher values with lower saturations because the machine operates near the BH knee point. This enables to have lower flux values which modify the vector diagram at the maximum loading maintaining low angles between current and voltage vectors.
A lower electrical loading means less current in the slots and this helps in reducing the Joule losses leading to a better thermal behaviour in which it can be noticed that the water cooling system is oversized in many cases. In those motors the cooling system can be reduced in size allowing economic advantages and outer volume savings.
Lastly the ferrite magnets introduced in PMREL machines have an higher volume with respect the rare earth magnets in IPM but despite this they maintain a lower price which allows higher motor volumes in order to equalize the IPM performances.
All the cited observations together with good values of output torques and powers, similar to the ones of the pure electric vehicles lead to consider this motor as a good competitor with the IPM one when the performances required are not very strict as in models like Lexus or Accord motors. Hence this typology of motor can be a valid substitute of IPM for pure electric vehicles like BMW i3 and Nissan Leaf.

Chapter 5

Synchronous Reluctance motor analysis

This chapter analyses pure reluctance motor in order to understand their possible application in the automotive field. The geometries under investigation are characterised by the same dimension of the PMREL introduced in chapter four. From the observation in chapter three it can be said that this type of motor exhibits less performance than the IPM and PMREL ones, and this is caused by the absence of magnetic material in the rotor. The main advantages of a reluctance motor are its lower costs and the possibility of higher electrical loadings with-respect the PMREL.

5.1 Preliminary discussion

The electrical loading can be risen here toward higher levels in order to reach higher output torque. The problem in doing this is that the saturation in the machine will increase causing non linearities in the torque as function of the supplied current, lowering in the saliency ratio and worsening the power factor. In order to have good values of saliency ratio only the 4 pole and 6 poles motors have been evaluated. The first approach follows the same rules suggested in chapter 4, in particular a first analysis of different geometries at the same electrical loading is carried out. The limits taken into account in this analysis are reported below:

- Maximum conductor peak current of 550 [A]
- Maximum DC bus voltage of 345 [V]
- $D_{ext} = 256$ [mm]
- $L_{stk,max} = 180$ [mm]
- Electrical loading equal to 150 [kA/m]

The electrical loading has been brought to 150 [kA/m] because in this motor the magnets are not present and this allows to bypass the demagnetisation problem. However the electrical loading cannot be increased too much because it will introduce high saturation in the machine iron leading to a worsening of power factor. The first evaluated motors have the following main data:

- Q_s = 12 - 72 slots
- $D_i = 160$ [mm]
- $L_{stk} = 180$ [mm]
- 3 barriers rotor
- $\hat{K}_{s,max} = 150$ [kA/m]

With these imposed values it is expected to have the maximum torque performance because of the high volume but at the same time the flux weakening and MTPV performances will be the worst. In the following table the main output performances are presented in order to make a first comparison of this motor typology.

$2p$ -	q -	Q_s -	n_c -	$\hat{I}_{c,max}$ A	$\hat{K}_{s,max}$ kA/m	T_{max} Nm	Ω_B rpm	T_{nom} Nm	P_{max} @ ω kW @ rpm	P_{out} @ $12krpm$ kW
4	1	12	12	550	150	397	2300	241.9	98 @ 2400	11
4	2	24	6	550	150	396	2490	229.5	106 @ 2680	18
4	3	36	4	550	150	432	2460	258.8	114 @ 2600	15
4	4	48	4	410	150	410	1860	236.7	82 @ 2000	11
4	5	60	4	330	150	405	1500	236.6	65 @ 1600	8
4	6	72	4	275	150	411	1260	260.3	56 @ 1350	4
6	2	36	4	550	150	449	2000	276.6	100 @ 2200	14
6	3	56	4	375	150	445	1450	267.0	70 @ 1560	7
6	4	72	4	275	150	442	1110	260.6	52 @ 1180	4

Table 5.1: Comparison of the pure reluctance explored geometries with the maximum available volume.

As visible in table 5.1 reluctance motors exhibit a high value of peak torque which is related to the high machine volumes because all the available L_{stk} has been used. The main downside in doing this is that the base point is at very low speeds compared with the maximum speed required. After the base speed is reached the machine enters the flux weakening region which is very limited in duration. This happens because of the high fluxes in the iron due to the electrical loading values. All these facts are explained in the previous chapter because the machine limits are the same. This base point value make it easy to understand that this machine is competitive with the other types only up to the base speed as the MTPV region is the weakness of this machine.

5.2 Stack length reduction

In order to increase the base speed, one of the previous machines has been shortened at first up to a stack length of 100 [mm] and then to 60 [mm]. This different length will produce a lower output torque because of the less active volume but, due to the lower torque, power curve slope will be lower and this means that the maximum power will be reached at higher speeds. This is caused by the fact that with less volume the flux in the machine is lower in a proportional way implying that at the same speeds the shorter motor will have a lower terminals voltage with respects the longer ones. These facts are reported in the table and graphs below.

$2p$ -	q -	Q_s -	n_c -	$\hat{I}_{c,max}$ A	L_{stk} mm	T_{max} Nm	Ω_B rpm	P_{max} @ ω kW @ rpm	P_{out} @ $12krpm$ kW
4	3	36	4	550	180	432	2460	113.9 @ 2600	14.9
					100	240	4430	113.9 @ 4730	36.2
					60	144	7380	113.9 @ 7870	74.1

Table 5.2: 4 poles 36 slots REL motor with $D_i = 160$ [mm], 3 air barriers and different L_{stk}.

Table 5.2 underlines that with a pure reluctance motor a considerable amount of power can be developed at high speeds as shown in the shortest machine case. The drawback of a shorter motor is that the output torque is reduced due less active volume. The 60 [mm] motor has been chosen because its length is similar to other automotive motors like Prius 2010 [18]. The same reluctance motor is then modified in the internal diameter in order to have a possible comparison with the previous chapter PMRELs. Due to the higher internal volume for this machine a 4 barriers geometry has been chosen. In table 5.3 the main results of this motor are presented.

$2p$ -	q -	Q_s -	n_c -	$\hat{I}_{c,max}$ A	L_{stk} mm	T_{max} Nm	Ω_B rpm	P_{max} @ ω kW @ rpm	P_{out} @ $12krpm$ kW
4	3	36	4	550	180	381	2780	114.5 @ 3000	21.9
					100	211	5000	114.3 @ 5390	46.9
					60	127	8340	114.5 @ 9000	87.7

Table 5.3: 4 poles 36 slots REL motor with $D_i = 180$ [mm], 4 air barriers and different L_{stk}.

It is important to notice that the maximum developed torque has been reduced with-respect the one of 3 barriers motors but the base speed has been slightly improved. This fact has to be considered in order to do future optimisations of this motor typology. From these two tables it is noticeable that an output torque of 200 - 240 [Nm] is developed up to 4400 - 5000 rpm from a pure reluctance machine. 100 [mm] is the stack length that allows to reach those torques and it is higher than the length of an actual automotive motor. This means that a possible REL motor will be heavier because of its lower torque density.

Model	L_{stk}	D_i	Vol_{int}	Vol_{ext}	Ω_B	T_{max}	P_{max}
4 poles	180	160	3.62	9.27	2460	432	113.9
36 slots	100		2.01	5.15	4430	240	113.9
D_i 160	60		1.21	3.09	7380	144	113.9
4 poles	180	180	4.58	9.27	2780	381	114.5
36 slots	100		2.54	5.15	5000	211	114.5
D_i 180	60		1.53	3.09	8340	127	114.5
Prius 10	50.8	161.9	1.05	2.78	2800	207	60
LEAF	151	131	2.04	4.74	2100	280	80
i3	132.2	180	3.36	6.09	4000	250	125

Table 5.4: REL motors main dimension compared with other automotive adopted IPM motors.

The comparison of torque and power densities is carried out from the values in table 5.4 and presented in the following table 5.5. This table directly compares REL torque and power densities with the IPMs and PMRELs introduced in previous chapters. From these values it can be noticed that pure reluctance motors have a lower torque density with respect IPM automotive ones and in order to give a fast comparison reluctance motors reach the BMW i3 torque density but with an almost doubled electrical loading. This has been previously discussed in chapters three and is mainly due to the rare earth magnet presence in the IPM.

The pure reluctance motor with 100 [mm] stack can reach an automotive similar output torque up to 5000 [rpm]. This performance can be helped with by reducing the maximum speed requested to the motors, for example it can be limited at 10 [krpm] in order to have a lower output power loss at high speed. The 10 [krpm] is a valid limit because many different automotive motors are limited at this speed, for example the Lexus and the Leaf models.

Model	L_{stk}	Vol_{int}	Vol_{ext}	T_{max}/Vol_{int}	T_{max}/Vol_{ext}	P_{max}/Vol_{int}	P_{max}/Vol_{ext}
-	mm	l	l	Nm/l	Nm/l	kW/l	kW/l
4 poles	180	3.62	9.27	119.3	46.6	31.5	12.3
36 slots	100	2.01	5.15	119.4	46.6	56.6	22.1
D_i 160	60	1.21	3.09	119.0	46.6	94.1	36.9
4 poles	180	4.58	9.27	83.2	41.1	25	12.4
36 slots	100	2.54	5.15	83.1	41.0	45.1	22.2
D_i 180	60	1.53	3.09	83.0	41.1	74.8	37.1
Prius 10	50.8	1.05	2.78	197.1	74.5	57.1	21.6
LEAF	151	2.04	4.74	137.3	59.1	39.2	16.9
i3	132.2	3.36	6.09	74.4	41.1	37.2	20.6

Table 5.5: REL motors main dimension compared with other automotive adopted IPM motors.

If the previously cited speed limits are here introduced then the reluctance models can be directly compared with two exponents of the IPM motors. The IPM chosen here are the Prius and the Leaf models because they present a lower peak power than the others. This leads to understand that the possible usage of this motor is on low performances vehicles like city or small size cars.

The graphs which present the torque and power performances of these compared motors are shown in figures 5.1 and 5.2.

From these graphs is can be observed that the torque developed from the reluctance motors is comparable in many cases with the IPM ones. For example the 100 [mm] stack reluctance motor is capable of 211 - 240 [Nm] and this torque is stable up to a base speed which is double of the IPM one. This leads to a peak power higher than the Leaf power (80 [kW]) in a speed range between 3000 and 7000 [rpm]. The main disadvantage in the reluctance motor is that, as stated in the previous chapters, the torque has a fast drop in flux weakening and MTPV regions and this results in having the IPM power still higher than the REL up to 8000 [rpm].

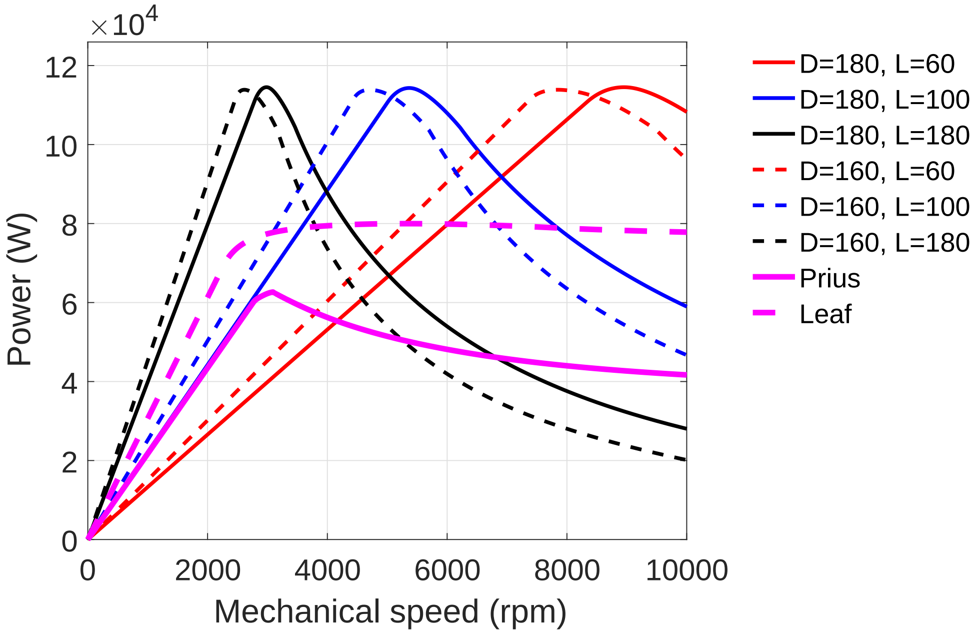

Figure 5.1: Power comparison between reluctance motors and Prius and Leaf IPM motors.

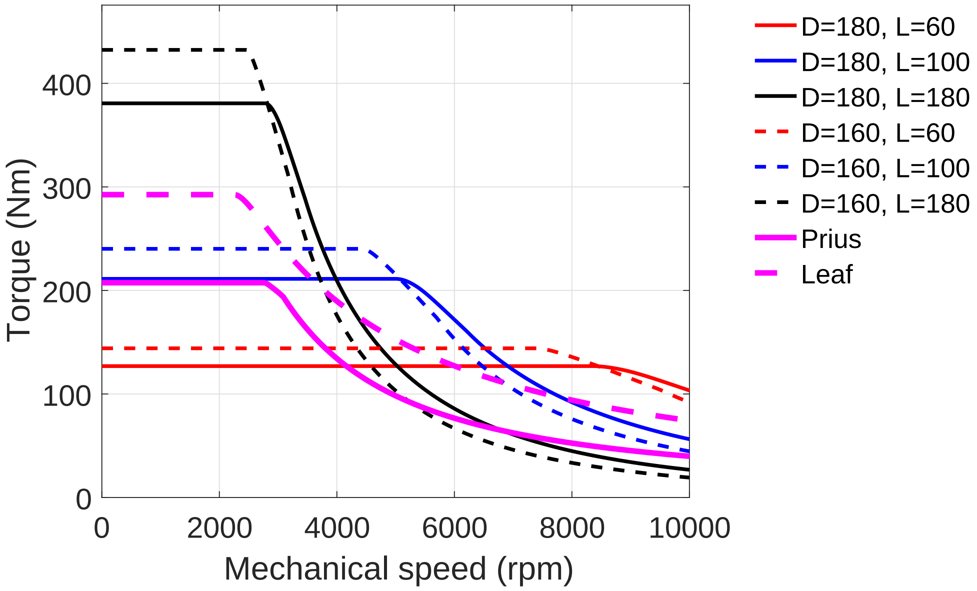

Figure 5.2: Torque comparison between reluctance motors and Prius and Leaf IPM motors.

In order to further increase the maximum speed powers the stack length can be reduced up to 60 [mm] leading to base speed moved toward 7000-8000 [rpm] but with a consequent reduction in the output torque which is decreased at 130 - 140 [Nm].

Hence, from these graphs it can be noticed that the reluctance typology of motor can be competitive with an IPM if the speed range is limited because the main disadvantage of this motor is the high speeds region.

In order to compare the REL with a PMREL of the previous chapter it is presented a graph with the same speed range for two similar machines. The PMREL chosen for this comparison is the 36 slots 4 poles which was discarded in the previous chapter.

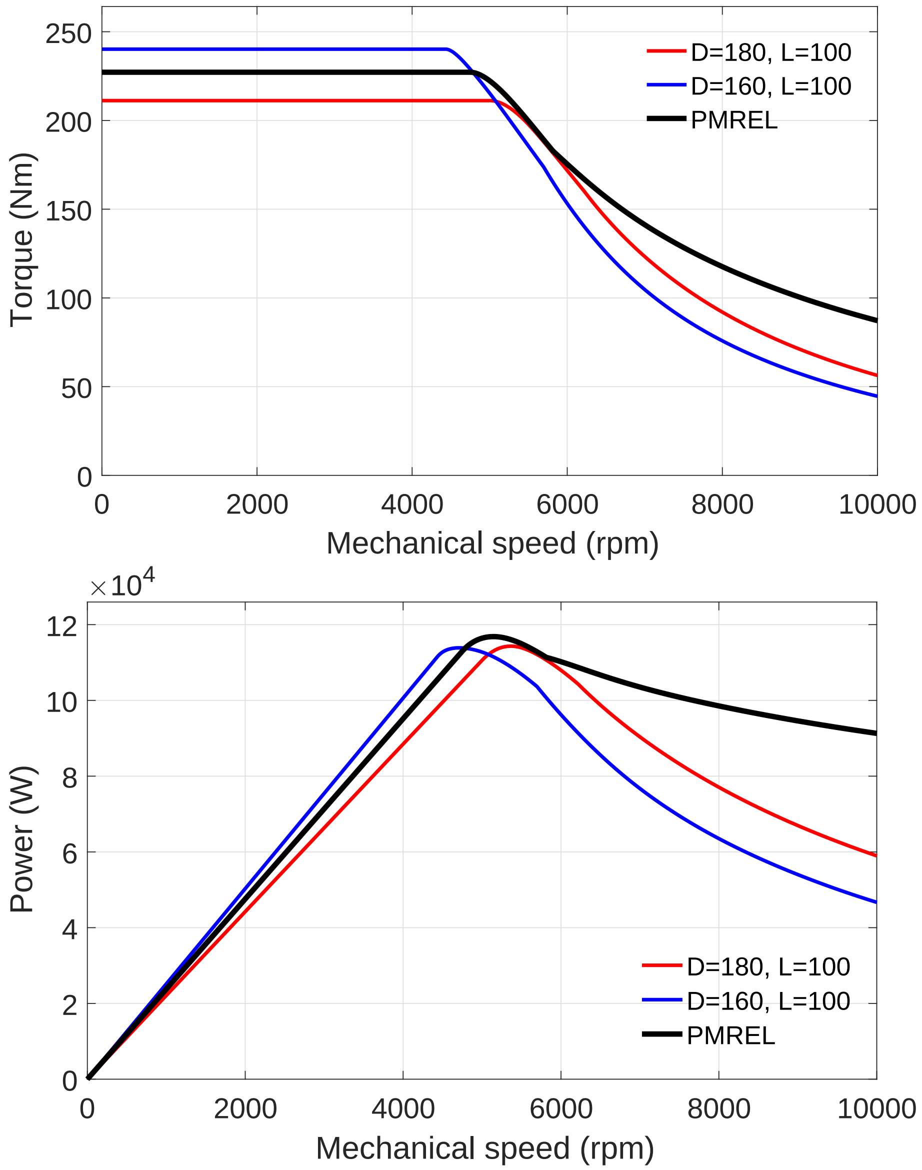

Figure 5.3: Torque and power comparison between REL and PMREL models characterised from the same main geometrical data.

The figure 5.3 shows that the torque developed from one of the REL motor is higher than the PMREL one. This is only due to the fact that the PMREL geometry has been supplied with an electrical loading lower than the REL model because the demagnetisation problem with the ferrite magnets. Even though the electrical loading is lower the torque is similar to the REL motor and the high speed behaviour of the PMREL is a lot better than the reluctance model.
Due the Ferrite PM the PMREL high speed power remains between 110 and 90 [kW] with-respect the REL one which drops toward about half of the PMREL power.

5.2.1 Cost and volume comparison

For the cost comparison the prices cited in 4.2.4 are taken into account and the following table 5.6 can be introduced. In this table there are IPM estimated prices and three PMREL of the previous chapter are taken as reference.

Model -	Iron mass $[kg]$	Copper mass $[kg]$	PM mass $[kg]$	Iron price *euro*	Copper price *euro*	PM price *euro*	Total price *euro*
IPM models							
BMW i3	26.3	4.6	2.57	29	33	160 - 205	222 - 266
Lexus	24.8	3.6	1.4	27	25	85 - 110	137 - 162
Prius 10	16.7	5.2	0.78	18	36	50 - 63	104 - 117
Accord M	21.4	6.3	1.24	24	44	75 - 100	143 - 168
LEAF	27.1	3.9	1.88	30	27	110 - 150	167 - 207
PMREL models D_i = 180 mm							
6p, 72 slot 100 mm	25.0	9.4	2.85	27	66	20	113
8p, 72 slot 100 mm	23.4	8.3	3.19	26	58	22	106
10p, 60 slot 100 mm	24.2	7.2	2.65	27	50	19	96
REL models D_i = 160 mm							
4p, 36 slot 60 mm	16.2	9.8	0	17.8	68.6	0	86.4
4p, 36 slot 100 mm	26.9	11.4	0	29.6	79.8	0	109.4
4p, 36 slot 180 mm	48.5	14.4	0	53.4	100.8	0	154.2
REL models D_i = 180 mm							
4p, 36 slot 60 mm	16.2	9.0	0	17.8	63	0	80.8
4p, 36 slot 100 mm	27.0	10.2	0	29.7	71.4	0	101.1
4p, 36 slot 180 mm	48.6	12.8	0	53.5	89.6	0	143.1

Table 5.6: Total price comparison between analysed IPM, PMREL from the previous chapter and 4 poles reluctance motors.

From table 5.6 it is evinced that the 4 poles reluctance motors are characterised by an high copper price because of the longer end windings. This means that the cost saving with-respect PMREL version are very low despite the great performance loss at high speeds.

5.3 Conclusion

The reluctance motor can develop suitable torques for an automotive application but its performances are satisfying until the base speed is reached. After that speed there is a rapid torque drop which leads to low high speed powers. In order to improve this behaviour the motors has been shortened and with a 100 [mm] long stack it presents valid power performances up to 6000 - 7000 [rpm].
The cost savings alone do not justify the introduction of this motor typology which presents the worst high speed performances combined with the lowest power factor of of the three types that have been analysed.

Conclusion

The major aim this thesis has achieved is the understanding that the PMREL typology of motor is suitable for an automotive application even though its torque density is lower with respect the IPM one. In particular it has been demonstrated that a PMREL with the main correct dimension is competitive for an application in which the pure performance is a secondary aspect. The chosen motors are characterised by the maximum outer and internal diameters available and a lower stack length with respect the maximum allowed. The amount of Ferrite PM in the rotor has been maximized in order to increase flux weakening performances. These dimensions have been selected in order to meet the right amount of torque compatible with an automotive application and to take the base speed as high as possible in order to have competitive powers at high speeds.

The developed motor has similar output performances to the Nissan Leaf IPM motor but at the same time it is characterised by an higher volume and a lower cost.

The reluctance motors that have been studied are characterised by a lower number of poles in order to maximize the saliency ratio. Two configurations have been taken into account, with different internal diameter and number of air barriers.

Reluctance motor presents good torque performances but limited to low base speed. After that speed, the performance experiences a considerable drop which is not compatible with an automotive application.

The final consideration is that, with a small price increment due to the Ferrite permanent magnet, the high speed performance is suitable for a possible automotive application.

Bibliography

[1] Alberto Amadio. “Analisi del Sistema di Raffreddamento di Motori Elettrici Per Trazione (Analisys of the cooling system of electric motors for traction)”. Master Thesis. UNIPD, 2012.

[2] Massimo Barcaro, Nicola Bianchi, and Freddy Magnussen. “PM Motors for Hybrid Electric Vehicles”. In: *The Open Fuels and Energy Science Journal* (2009).

[3] Grazia Berardi and Nicola Bianchi. “Design Guideline of an AC Hairpin Winding”. 2018.

[4] Nicola Bianchi. *Calcolo delle macchine elettriche col metodo degli elementi finiti*. 2001.

[5] Nicola Bianchi. *The Rediscovery of Synchronous Reluctance and Ferrite Permanent Magnet Motors*. 2016.

[6] Nicola Bianchi, Massimo Barcaro, and Silverio Bolognani. “Electromagnetic and Thermal Analysis of Permanent Magnet Synchronous Machines”. In: *Finite Element Analysis – From Biomedical Applications to Industrial Developments*. 2012.

[7] Nicola Bianchi and Silverio Bolognani. *Metodologie di progettazione delle macchine elettriche*. 2001.

[8] T. A. Burress et al. *EVALUATION OF THE 2008 LEXUS LS 600H HYBRID SYNERGY DRIVE SYSTEM*. Technical report. Oak Ridge National Laboratories, 2009.

[9] T. A. Burress et al. *Oak Ridge National Laboratory Annual Progress Report for the Electric Drive Technologies Program*. Technical report. Oak Ridge National Laboratories, 2016.

[10] David G. Dorrell et al. “Comparison of Different Motor Design Drives for Hybrid Electric Vehicles”. In: *IEEE TRANSACTIONS ON INDUSTRY APPLICATIONS* (2012).

[11] Marco Ferrari, Nicola Bianchi Senior Member IEEE, and Emanuele Fornasiero. “Analysis of Rotor Saturation in Synchronous Reluctance and PM Assisted Reluctance Motors”. In: *IEEE TRANSACTIONS ON INDUSTRY APPLICATIONS, VOL. 51, NO. 1* (2015).

[12] Tobias Glaessel, Johannes Seefried, and Joerg Franke. “Challenges in the Manufacturing of Hairpin Windings and Application Opportunities of Infrared Lasers for the Contacting Process”. In: *IEEE TRANSACTIONS* (2017).

[13] *Inside the HVH Hybrid Motor: Technical Insights on Remy s "Off-the-Shelf" Hybrid Motor Solutions*. 2009.

[14] J. Juergens et al. “Innovative Design of an Air Cooled Ferrite Permanent Magnet Assisted Synchronous Reluctance Machine for Automotive Traction Application”. In: *IEEE* (2016).

[15] Dae-Sung Jung et al. “Optimum Design of the Electric Vehicle Traction Motor using the Hairpin Winding”. In: *IEEE TRANSACTIONS* (2012).

[16] Paolo Mancinelli, Simone Stagnitta, and Andrea Cavallini. “Qualification of Hairpin Motors Insulation for Automotive Applications”. In: *IEEE TRANSACTIONS ON INDUSTRY APPLICATIONS* (2017).

[17] Mattia Morandin. “Electric Drives with Permanent Magnet Synchronous Machines Connected to Internal Combustion Engines”. PhD thesis. UNIPD, 2013.

[18] Mitch Olszewski. *EVALUATION OF THE 2010 TOYOTA PRIUS HYBRID SYNERGY DRIVE SYSTEM*. Technical report. Oak Ridge National Laboratories, 2011.

[19] Burak Ozpineci. *Oak Ridge National Laboratory Annual Progress Report for the Power Electronics and Electric Motors Program*. Report. Oak Ridge National Laboratories, 2014.

[20] Giorgio Pietrini. *Analisi di motori IPM per trazione automobilistica*. PhD course. Università di Parma, 2017.

[21] Se-Hyun Rhyu et al. “Design of the End-Coil Structure with Square Conductor for the Automobile ISG”. In: *KINTEX, Korea*. Ed. by Korea Intelligent Mechatronics Research Center Korea Electronics Technology Institute. 2015.

[22] Bulent Sarlioglu et al. “Benchmarking of electric and hybrid vehicle electric machines, power electronics and batteries”. In: *Wisconsin Electric Machines and Power Electronics Consortium (WEMPEC)*. Ed. by University of Wisconsin-Madison. 2015.

[23] R. H. Staunton, T. A. Burress, and L. D. Marlino. *EVALUATION OF 2005 HONDA ACCORD HYBRID ELECTRIC DRIVE SYSTEM*. Technical Report. Oak Ridge National Laboratories, 2006.

[24] Al Steier et al. *Advanced Strong Hybrid and Plug In Hybrid Engineering Evaluation and Cost Analysis*. Report. California Air Resources Board: CARB Agreement 15CAR018, 2017.

[25] *Technical Specifications BMW i3*. 2014.

[26] *THE HIGH VOLTAGE BATTERIES OF THE BMW i3 AND BMW i8*. 2014.

[27] *THE HYBRID SYNCHRONOUS MACHINE OF THE NEW BMW i3 and i8*. 2014.

[28] Yawei Wang and Nicola Bianchi. “Comparison of Synchronous Reluctance and IPM Motors for EV Applications Including design Approaches”. 2018.

[29] Rong Yang. “ELECTRIFIED VEHICLE TRACTION MACHINE DESIGN WITH MANUFACTURING CONSIDERATIONS”. PhD thesis. McMaster University, 2016.